Molten Salt-Carbon Nanotube Thermal Energy Storage for Concentrating Solar Power Systems
Final Report
March 31, 2012

Michael Schuller, Frank Little, Darren Malik, Matt Betts, Qian Shao, Jun Luo, Wan Zhong, Sandhya Shankar, Ashwin Padmanaban

The Space Engineering Research Center
Texas Engineering Experiment Station
Texas A&M University

Abstract

We demonstrated that adding nanoparticles to a molten salt would increase its utility as a thermal energy storage medium for a concentrating solar power system. Specifically, we demonstrated that we could increase the specific heat of nitrate and carbonate salts containing 1% or less of alumina nanoparticles. We fabricated the composite materials using both evaporative and air drying methods. We tested several thermophysical properties of the composite materials, including the specific heat, thermal conductivity, latent heat, and melting point. We also assessed the stability of the composite material with repeated thermal cycling and the effects of adding the nanoparticles on the corrosion of stainless steel by the composite salt. Our results indicate that stable, repeatable 25-50% improvements in specific heat are possible for these materials. We found that using these composite salts as the thermal energy storage material for a concentrating solar thermal power system can reduce the levelized cost of electricity by 10-20%. We conclude that these materials are worth further development and inclusion in future concentrating solar power systems.

1.0 Introduction:

On May 9, 1979, President Carter celebrated the installation of a solar-thermal water heater at the White House as a small part of the "greatest and most exciting adventure ever undertaken by the American people", aimed at providing cheap, efficient energy from the Sun [1]. Despite these lofty claims thirty years ago, solar power is currently responsible for less than 1% of total energy generation in the United States. However, higher fuel prices, an increased demand for energy independence, and a desire to mitigate the effects of greenhouse gases have led the United States to once again invest in solar power generation.

As technology has progressed, methods of generating electricity have been crucial to the improving standards of living everywhere. The vast majority of the electricity in the world today is generated using limited resources, such as fossil or nuclear fuels. Alternative energy sources, such as wind, solar, and hydroelectric are gaining acceptance due to costs associated with fossil fuels. One way to improve the economic competitiveness of solar power is the use of a storage system, which maintains power delivery in case of clouds and provides power even when the sun is below the horizon.

The chief impediment to large-scale implementation of solar power generation has been its cost. DOE has created their concentrating solar power program to attempt to reduce the cost of solar power generation. This project is part of that program, and addresses the DOE objective of reducing the leveled cost of electricity from a Concentrating Solar Power Plant. The primary goals DOE has for the thermal energy storage material are to extend the power plant's upper operating temperature to 500^{o} C and to reduce the cost of the thermal energy storage subsystem to $15/kW-hr(th).

In thermal energy storage systems, various storage materials are used to improve performance, including molten salts. In the past, interest has been directed at nitrate eutectics (a eutectic is a fixed-ratio mixture of two or more materials that has a lower melting temperature than any other ratio of the mixture components). In this work, nanoparticles have been combined with the standard nitrate eutectic and other eutectic salts in an effort to improve the thermal characteristics of the molten salt for use in thermal energy storage systems. Current thermal energy storage systems are based on grid power scales, and so store large quantities (MWhrs) of energy. Therefore, the systems are generally large and contain a large volume of storage material. Increasing the specific heat of the nitrate eutectic will decrease the quantity of material required to store a given amount of energy in a given system, reducing the storage system cost and size. Reducing the cost means thermal energy storage systems could be implemented in more locations, improving the viability of commercial concentrating solar power. In addition, raising the operating temperature through the use of other low-cost higher melting eutectic salts can increase the thermodynamic efficiency of the conversion cycle, and the combination of higher temperature and increased specific heat capacity can further increase the economic viability of solar thermal energy generation.

The types of commercial concentrating solar power technologies are presented in section 2. Most of these technologies can be coupled with thermal energy storage (TES) systems which allow them to offset their electricity generation to periods of peak demand, smooth out the effects of weather-induced transients such as periodic cloud cover, and produce power after the sun has set [2]. The available thermal energy storage technologies are reviewed in Section 2. The developing field of utilizing nanometer sized particles to create nanofluids which have enhanced thermal properties is reviewed in Section 2. The experimental apparatus, procedures, and analyses used to create and evaluate composite thermal energy storage materials based on a eutectic salt mixture and nanoparticles are presented in Section 3.

1.1 PROJECT OBJECTIVES

The first objective of this project was to create a composite thermal energy storage material using nanoparticles embedded in a molten salt base material, including determining the proper constituents and their proper proportions to best balance thermal energy storage, heat transfer, and system cost. A wide range of materials were examined, encompassing alkali halides, alkali carbonates, nitrates/nitrites, and eutectics of these materials for the base material and carbon nanotubes, cellulosic nanoparticles and metal oxide nanoparticles. The choice of the best material was made based on economic and technical factors, including cost, lifetime, safety, and system performance.

The second objective of this project was to characterize the thermophysical properties of the composite material by measuring the pertinent thermophysical properties (specific heat, thermal conductivity, latent heat) as a function of temperature over the temperature range of interest, demonstrating that the composite material is cost effective, compatible with common stainless steels, and poses no additional safety risk when operated as part of a concentrating solar power plant.

The third objective of this project was to assess the utility of the composite material in a concentrating solar power application by determining the economic benefit of using the molten salt-nanoparticle material in a concentrating solar power system. A system model for a concentrating solar power plant was created and used to calculate the effects of changes to the thermal energy storage material on the cost and performance of the plant. Results from the material development work were used as inputs to the system model.

1.2 PROJECT SCOPE

This project created nanoparticles and embedded them in a base material, with the goal of creating a new composite material with thermophysical properties that were superior to those of the base material with respect to application in a concentrating solar thermal power plant. To achieve this goal, we engineered the properties of the composite material to provide higher specific heat, lower melting temperature, and higher thermal conductivity and diffusivity than the base material. We investigated the compatibility of the composites with common stainless steels to determine the suitability of the composite for use at temperatures cycling between 0° C and 600° C.

This project addressed the DOE objective of reducing the leveled cost of electricity from a Concentrating Solar Power Plant. The primary goals DOE has for the thermal energy storage material are to extend the power plant's upper operating temperature to 500° C and to reduce the cost of the thermal energy storage subsystem to $15/kWh(th). DOE has shown that thermal energy storage systems can achieve very high round-trip efficiencies. A secondary goal of this program is to maintain this high efficiency while improving the economics of the storage system. The composite material addresses these goals by providing a low cost material that will not degrade at the desired temperatures, while providing increased heat storage and improved heat transfer into and out of the composite.

1.3 Project Results

Using additives to alter the properties of a mixture is nothing new. The many varieties of steel are a testament to that. The largest difference between the older mixtures and nanomaterials is the size of individual pieces of the additive. For currently unknown reasons, nanoparticles seem to have a much larger effect on thermal properties than the same material in standard form at certain low mixture mass percentages. Therefore, adding nanoparticles allows for the possibility of emulating or exceeding the properties of mixtures that use much more expensive materials. More importantly, the reduced quantity of nanoparticles relative to the bulk material required reduces the cost to get the improved performance.

The results of this investigation show how the addition of ceramic nanoparticles alters the specific heat of mixed salt eutectic, and to what degree. A second result is the quantification of the change of the heat of fusion of the mixed salt eutectic. The third result determined the nanoparticle eutectic composite's stability over time in the standard concentrating solar power storage temperature range. The final result determined the nanoparticle eutectic composite's compatibility with materials commonly used for concentrating solar power storage systems (*i.e.,* stainless steel).

1.3.1 Specific Heat

The thermal properties of the composite and plain material were measured using two techniques: American Society for Testing and Materials (ASTM) 1269E and Modulating Differential Scanning Calorimetry (MDSC). These two techniques measured the specific heat and the heat of fusion of the plain and composite materials.

The results of all the ASTM and MDSC measurements suggest that the addition of the nanoparticles using the given manufacturing technique increased the specific heat of the molten salt by approximately 20% (with both measurement techniques showing approximately the same level of increase). The silica and the alumina improved the specific heat by nearly the same amount over the base material.

The thermal-physical properties of an alumina nanoparticle-nitrate salt nanofluid at low nanoparticle mass fraction (less than 2% by mass) were studied using nanofluids created by evaporation using either a hot plate or an air dryer. For the nanofluids fabricated by the hot plate method, the results show that there exists a parabolic relation between specific heat and mass fraction of alumina nanoparticles (maximum 30.6% enhancement with 0.78% mass fraction of alumina nanoparticles). For the nanofluids fabricated by the air dryer, the results show that the specific heats of the nanofluids are higher than the literature value of 1.55 J/gK for the base salt, ranging up to 2.07 J/gK at 0.0625% mass fraction of alumina nanoparticles.

1.3.2 Heat of Fusion

The heat of fusion of the nanoparticle nitrate eutectic composite did not seem to be significantly altered compared to the observed heat of fusion value of the unmodified nitrate eutectic material.

1.3.3 Material Stability and Cycling Effects

1.3.3.1 Stability of Nanoparticle Nitrate Eutectic Mixtures

It was observed that the nitrate-and-silica composite material's specific heat decreased if the material was raised to a temperature above 400° C. The specific heat was also observed to decrease over time, even when the temperature was well below 400° C. It is unknown why this occurred. The nitrate-plus-alumina composite and the plain nitrate were stable to a temperature of 450° C for the test duration.

1.3.3.2 Cycling Effects on Nanoparticle Carbonate Eutectic Mixtures

A Nano composite material consisting of a eutectic of lithium carbonate and potassium carbonate, and 1% by mass alumina nanoparticles was subjected to thermal cycling in a stainless steel tube using a temperature-controlled furnace. After thermal cycling, the stainless steel tube was sectioned into three equal parts – top, middle and bottom. Composite material samples were taken from the central region and near the wall region of each section.

The specific heat of this material in the temperature range of 290° C-397° C was measured using the Modulated Differential Scanning Calorimeter (MDSC) method. The concentration of alumina nanoparticles in this material was measured using neutron activation analysis. The average specific heat of the uncycled material was found to be 1.37 J/g° C. The average specific heat of the thermally cycled material was between 1.7-2.1 J/g° C. It was found that the concentration of the nanoparticle varied along the height of the sample tube, the nanoparticles tended to settle towards the bottom of the tube with thermal cycling. There was also migration of nanoparticles towards the wall of the sample tube with thermal cycling. Despite these gross movements of nanoparticles, there was no significant change in the specific heat of the Nano composite due to thermal cycling.

1.3.4 Materials Compatibility

The effect of silica nanoparticles on corrosion of steel by molten carbonate eutectic (42.7% Li_2CO_3, K_2CO_3) was investigated. The experimental design was based on static coupon immersion methodology where a coupon (material under study, in this case a rectangular stainless steel specimen of SS304 with dimensions approximately 5x20x0.6mm and weight 0.5g) is exposed to a static corroding environment for predetermined periods of time. The testing times were 2, 4, and 6 weeks. The temperature during testing was maintained at a constant 520° C. The instantaneous corrosion rates were determined by normalizing the mass loss with respect to time and area. The mass loss was determined by descaling the corroded steel coupons using concentrated hydrochloric acid. The instantaneous corrosion rates obtained from all three times showed a reduction in corrosion of steel by molten carbonate eutectics when doped with silica 1% by weight in comparison to the molten base carbonate eutectics.

The results showed that doping the carbonate eutectic with silica nanoparticles (1% by weight) reduced the corrosion of steel by half in comparison to the corrosion without doping.

1.3.5 System Modeling

A solar-thermal power plant performance simulation model has been built based on Matlab/Simulink. It calculates the electricity generation amount according to information such as project's location, weather situation, direct normal irradiation, project configuration, and so on.

An economic model has been built based on Matlab. It calculates the cost of electricity or electricity sale price based on the annual electricity generation amount (from performance model), installation and operation costs, type of financing, tax rate, applicable tax credits and incentives, customer requirement and so on. These two models can work together and they

provide the capability of running a batch of simulations in which results are compared and analyzed at the same time.

A risk analysis model considers the faults that may happen in the solar thermal plant and calculates their probabilities. It helps identify potential and most probable problems the system may have, and the economic loss that may be caused by various problems. This calculation is heavily based on the detailed configuration of a system and results from the previous two models. Decision tables, a fault tree and an event tree will be generated and plotted during the analysis procedure.

2.0 Background: Thermal Energy Storage Systems

2.1 Thermal Energy Storage

The concept of thermal energy storage in a concentrating solar power system is rather simple. Take thermal energy (heat) from the solar field and divert it from the power block to heat up or change the phase of a secondary medium in order to store the thermal energy for later use. Thermal energy storage systems can be classified as direct or indirect systems, which are further categorized as sensible or latent heat storage systems, depending on how the thermal energy is stored. Each of these systems allow concentrating solar power plants to smooth out transients, offset electricity delivery to the grid to periods of peak demand, and generate electricity after the sun has gone down. A thorough review of the current state of thermal energy storage is available in a report from the National Renewable Energy Laboratory (NREL) Survey of Thermal Energy Storage for Parabolic Trough Power Plants released in 2000 [6]. A brief summary of this report and supporting literature is presented in the following sections.

2.1.1 Classification of Thermal Energy Storage Systems

Traditionally, thermal energy storage systems (TES) have been characterized by their method of storing thermal energy. The broad categories of TES systems are sensible heat TES systems, latent heat TES systems, and chemical energy TES systems. Sensible heat TES systems store energy by heating up the TES material. Energy is then recovered as the TES material is allowed to cool. These types of systems are called sensible heat TES systems because they rely on the measureable or sensible change in the TES material's temperature to store thermal energy.

Latent heat thermal energy storage systems use the relatively high energy of fusion required to melt the TES material to store thermal energy. These types of TES systems usually operate over a much narrower temperature range than sensible heat storage systems do.

Chemical energy storage uses the solar field to drive reversible chemical reactions which store energy in chemical bonds. When a chemical TES system is discharged, the chemical bonds are broken, and the thermal energy can be extracted as needed. These thermal energy storage systems are discussed in greater detail in the Survey of Thermal Storage for Parabolic Trough Power Plants [3].The materials created during the course of this research project were used to investigate the potential impact of high temperature nanofluids on sensible heat thermal energy

storage systems. In general, sensible heat thermal energy storage systems rely on large scale temperature swings in the TES material to store thermal energy as governed by Eq. 1.

$$E(T) = M_s \int_{T_L}^{T_H} c_p(T) dT \qquad 1$$

In Eq. 1, E is the amount of thermal energy stored in the system as a function of temperature, M_S is the mass of the thermal energy storage material, C_p is the temperature dependent specific heat of the thermal energy storage material, and T_H and T_L are the highest and lowest operating temperatures of the TES system, respectively.

Sensible heat TES systems can use solids or liquids as thermal energy storage materials. Table 1 was adapted from the *Survey of Thermal Energy Storage for Parabolic Trough Power Plants* [3] and lists the operating range and approximate costs (in 1991 dollars) of sensible heat thermal energy materials on a $/kWh_t basis. Despite ongoing research into developing latent heat and solid media sensible heat TES systems, concentrating solar power plants traditionally rely on liquid sensible heat TES systems such as the two tank system employed in Spain at Andasol 1. The table clearly shows why nitrate salt eutectics such as Hitec-Solar Salt were the material of choice for both Solar II and Andasol 1: the low cost and widespread use of this material were the driving factors in selecting Hitec-Solar Salt as the base material for the foundation of this research project.

Table 1. Reported sensible heat storage materials and their associated costs [3].

TES Material	Operating Temp. (° C) T_L	T_H	Media Cost ($/kg)	Media Cost ($/kWh)
Solid Media				
Reinforced Concrete	200	400	0.05	1.0
Cast Iron	200	400	5.00	60.0
NaCl (solid)	200	500	0.15	1.5
Silica Fire Bricks	200	700	1.00	7.0
Sand Rock Mineral Oil	200	300	0.13	4.2
Liquid Media				
Synthetic Oil	250	350	3.00	43.0
Nitrite Salts (NO_2)	250	450	1.00	12.0
Nitrate Salts (NO_3)	265	565	0.70	5.2
Carbonate Salts	450	850	2.4	11.0
Phase change Media				
	Melting Temp. (° C)			
$NaNO_3$	308		0.2	3.6
KNO_3	333		0.3	4.1
Na_2CO_3	854		0.2	2.6
K_2CO_3	897		0.6	9.1

Sensible heat thermal energy storage systems can be classified as direct or indirect thermal energy storage systems by their interface with the solar field. Direct thermal energy storage systems use the solar field's heat transfer fluid (HTF) as the thermal energy storage medium and therefore do not require heat exchangers. Indirect TES systems do not use the solar field's HTF

to store energy but rather store heat indirectly by using a heat exchanger to heat up the TES material. The most common types of sensible heat thermal energy storage systems are the two tank TES system and thermocline TES system. Both of these thermal energy storage systems can be implemented as direct or indirect systems and are discussed in greater detail in the following section.

2.1.2 Description of Sensible Heat TES Designs

2.1.2.1 Two Tank Storage

Two tank storage systems can be implemented in both direct and indirect configurations. The two tank TES system used at Solar II was implemented as a direct TES system as shown in Fig. 1.

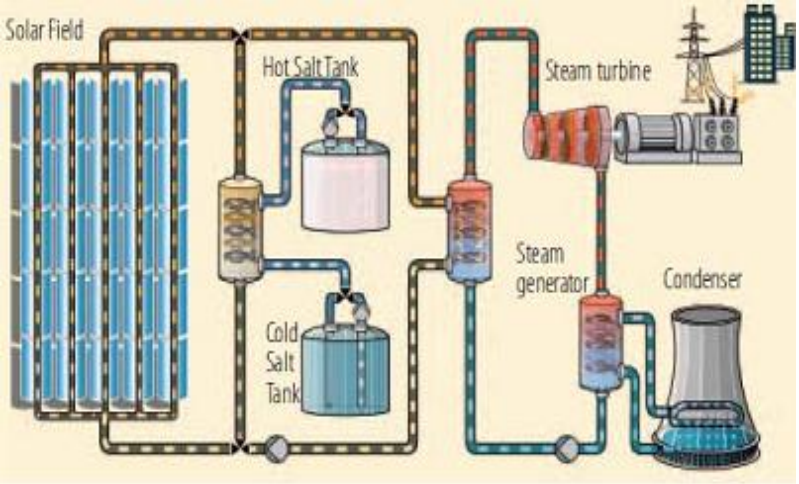

Figure 1 Schematic of a direct two tank TES system.

As the name implies, two tank TES systems use two large isothermal storage tanks. As the system is charged, salt stored in the cold tank is pumped through the solar field or into a heat exchanger where it is heated to its upper operating temperature. The hot salt is then stored in a second salt storage tank until it is needed. When the system is discharged, salt from the hot tank is pumped from the hot tank to the steam generator where it releases its stored energy. The cold salt is then pumped from the steam generator to the cold storage tank until the system can be recharged and the cycle started again.

2.1.2.2 Thermocline

Thermocline systems rely on thermal stratification of the TES material to store energy in a single tank, as shown by the gradient in Fig. 2.

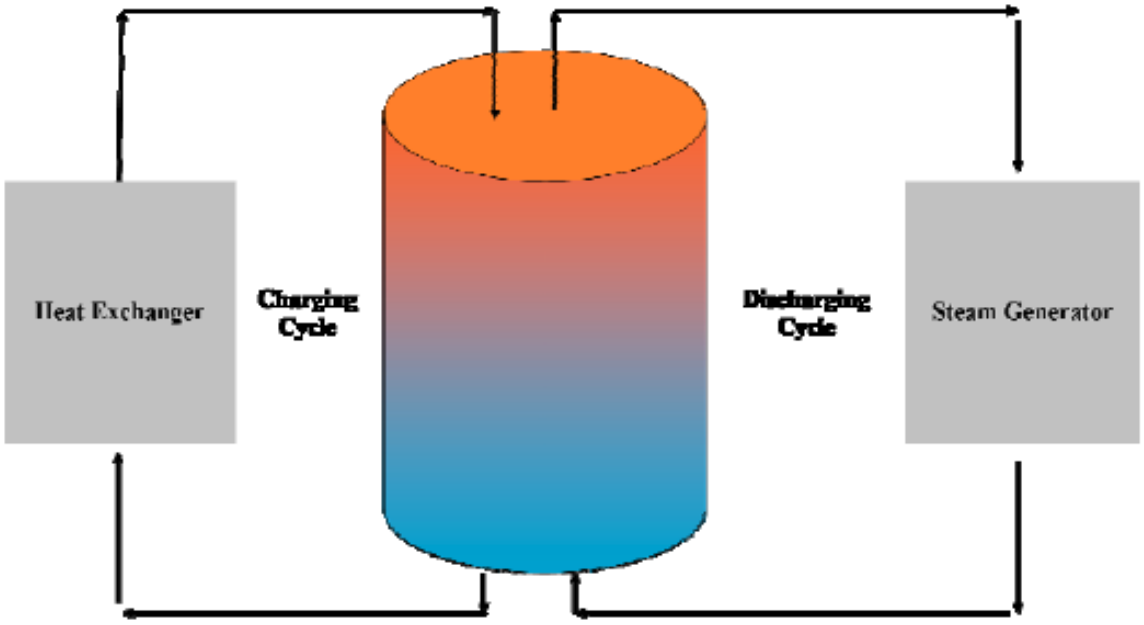

Figure 2 Schematic of an indirect thermocline TES system.

As the TES is charged, cold liquid is drawn from the bottom of the tank and heated either directly by the solar field or indirectly in a heat exchanger (as shown); the hot fluid is then reintroduced into the top of the thermocline tank. When the system is discharged, the flow is reversed: the hot fluid is drawn from the top of the tank, sent to a steam generator where it gives up its thermal energy, and returned as cold fluid that is pumped into the bottom of the tank. Some thermoclines can be considered hybrid solid/liquid sensible heat storage systems because they use a cheap filler material such as limestone, quartz, or sand to replace the more expensive oil or salt heat transfer or TES fluid [4].

This research focused on two tank sensible heat thermal energy storage systems similar to the one employed in the Solar II pilot concentrating solar power plant and the one currently in use at Andasol I in Spain. The two tank system is the simplest of the available sensible heat TES technologies. Additionally, the purpose of this research is to investigate the ability of alumina nanoparticles to impact the specific heat of Hitec-Solar Salt. Measurement of thermal conductivity is of secondary importance and would need to be investigated thoroughly before the composite was used in a thermocline, to ensure that the nanoparticles would not enhance the heat transfer capabilities of the composite to the point that thermal stratification would not occur, thus destroying the operating principle of the thermocline TES system. Finally, the effects of thermal gradients on the stability of the composite materials were not investigated. While further study into these effects is needed, the current state of research is best applied to the isothermal cold and hot tanks of the two tank TES system.

2.1.3 Why Thermal Energy Storage

There are several different types of energy storage devices and technologies which can be coupled with concentrating solar power production to extend the power plant’s delivery of

electricity into the hours following sunset. An advantage of thermal energy storage is that it stores the energy collected in the solar field directly, without the thermal-mechanical-potential energy conversion losses of other systems. These potential energy storage systems rely on water displacement or compressed air to store energy until it is needed later. An alternative to potential energy storage systems is electrical energy storage systems, batteries, which store the solar energy after it has been converted to electricity. These energy storage systems are able to avoid storage penalties due to conversion inefficiencies because they store the energy in its final useable state; however, most of these systems are only able to return 75% of the stored electricity to the grid [5]. The approximate $\$/kWh_e$ capital costs for these systems are presented in Table 2. These cost estimates where adapted from Divya's *Battery energy storage technology for power systems-An overview* [5]. A euro to dollar conversion factor of 1.484 was used to adapt the values given by Divya for direct comparison to reference thermal energy storage cost estimates.

Table 2 Approximate capital costs for available electricity storage systems [5].

Battery Type	Largest Capacity	Approximate Cost ($\$/kWhr_e$)	
Lead Acid (Flooded Type)	10 MW/ 40 MWh	74.20	222.60
Lead Acid (Valve Regulated)	300 kW/ 580 kWh	74.20	222.60
Nickel Cadmium	27 MW/ 6.75 MWh	296.80	890.40
Lithium Ion		1038.80	1484.00
Vanadium Redox	1.5 MW/1.5 MWh	534.24	1484.00
Zinc Bromine	1 MW/ 4 MWh	534.24	1484.00
Metal Air		74.20	296.80

The Andasol I TES storage system cost is approximated to be between 32.33-30.88 $\$/kWh_t$ [9] or 81.80-85.64 $\$/kWh_e$, assuming the 37.75% conversion cycle efficiency in DOE's Excelergy model. The low cost of thermal energy storage makes it competitive with current battery energy storage systems. In addition to offering a cost effective means of storing thermal energy for later electricity production, TES systems offer a buffer against transient weather conditions that can cause the turbine in solar power plants to operate at reduced capacity or shut down without thermal energy storage. The potential for nanofluids to lower the thermal energy storage cost below that of lead acid batteries is discussed in the following sections.

2.2 Nanofluids

Nanofluids are generally defined as suspensions or colloids created by dispersing particles less than 100 nm in size into a base fluid. Nanofluids are the latest attempt to improve the thermal conductivity and heat transfer of liquid media by introducing high conductivity particles into water and other heat transfer fluids. In general, heat transfer fluids offer relatively low thermal conductivities when compared to those of solid metals or metal oxides. The concept of adding solid particles to a liquid base material is not a new one; suspensions of millimeter-and-micrometer-sized particles have been used to try to improve the thermal conductivity and heat transfer properties of various heat transfer fluids. However, these suspensions are generally unstable and have failed to provide the necessary thermal properties and performance required to meet the demands of current heat transfer applications. Unlike previous suspensions, which used larger scale particles, nanofluids have been shown to offer higher thermal conductivity and improved critical heat flux while offering improved suspension stability [6].

2.2.1 Enhancement of Thermal Properties

The process by which nanoparticles improve the thermal properties of base fluids is still not well understood. Many early experiments reported results that were not compatible with available heat transfer theories at the time. However, there is a growing base of knowledge that supports the ability of nanofluids to improve the thermo-physical properties of base heat transfer fluids. In general, nanofluids are believed to offer improved thermal properties because the nanoparticles act as bridges or provide structure between adjacent fluid molecules. What is particularly exciting about nanofluids is the ability of nanoparticles at relatively low concentrations (<1% volume fraction) to change the thermal properties of the base fluid, such as thermal conductivity, by approximately 10% - 40% [10]. The size and concentration of the nanoparticles in the nanofluid have been shown to affect the fluid thermal conductivity. Much of the research into nanofluids has focused on efforts to improve the thermal conductivity of the base fluid, while nanofluid specific heat, viscosity, and other thermal and fluid properties have received less attention.

2.2.1.1 Specific Heat Capacity

In 2008, a paper by Zhou and Ni entitled *Measurement of the specific heat capacity of water-based Al2O3 nanofluid* [7] claimed that the specific heat of water-based nanofluids could be predicted using the model given in Eq. 2. The model predicts the specific heat of a nanofluid, C_p (nf) based on the density (ρ) specific heat (C_p) of the nanoparticles (np) and base fluid (bf) along with the volume fraction of the nanoparticles (Φ).

Proposed model for predicting the specific heat of nanofluids

$$C_{pnf} = \frac{\psi(\rho c_p)_{np} + (1-\psi)\left(\rho C_p\right)_f}{\psi\rho_{np} + \left(1-\psi\right)\rho_f} \quad (2)$$

The scope of the investigation was rather limited, as the average specific heat of the nanofluid was only calculated for a temperature range of 25 – 40° C. Despite the limited experimental temperature range, the model was shown to agree quite well with experimental results over a wide range of nanoparticle volume fractions, 0 - 21.7%. Differential scanning calorimetry (DSC) measurements performed by Zhou showed that the introduction of alumina nanoparticles into water produced nanofluids that exhibited smaller specific heats of the nanofluid than that of the base fluid [7].

Previous work at the Air Force Research Lab in the field of nanofluids contradicts the experimental results published by Zhou. Experiments performed by I.C. Nelson showed approximately a 30% improvement in the specific heat of a water-based nanofluid which used exfoliated graphite nanoparticles [8].

The nanofluids created for the present research into developing new TES materials are an entirely new class of nanofluids that use Hitec-Solar Salt as the base fluid. Due to the exploratory nature of this work, alumina nanoparticles were selected as the nanoparticle of choice due to their wide availability and the potential impact of high temperature nanofluids on TES systems.

Andasol 1 in Spain is a CSPP that uses parabolic troughs and a two-tank storage system that has the capacity to store enough thermal energy to operate the turbine for 7.5 hours after the solar field has shut down for the day. Due to the geographic location of the plant, Andasol 1 is able to provide electricity almost 24 hours a day during the summer months [2]. In general, larger capacity TES systems require a larger capital investment but deliver energy at a lower cost because the larger capacity allows for increased power production and spreads the cost of the system over a larger operating window [9]. Despite the widespread literature supporting the economics and benefits of coupling thermal energy storage systems with concentrating solar power plants, only four thermal energy storage systems have been constructed in the United States, none of which are in operation today. California's Solar I and Solar II pilot plants were each shut down following the completion of their test periods of operation. The solar energy generation station SEGS I in California had a two-tank TES system that caught fire and was never repaired or replaced. Presumably, the lack of TES systems in the American solar power industry is due to the large capital costs associated with these systems.

The DOE uses a $/kWh$_t$ figure of merit for evaluating potential thermal energy storage systems when evaluating TES systems. The $/kWh$_t$ costs of thermal energy storage materials, which operate over a particular temperature range (ΔT), are calculated using Eq. 3. As the equation shows, any increase in the specific heat or the operating range of the thermal energy system results in an improved $/kWh$_t$ media cost. For the purposes of this research it is assumed that the introduction of nanoparticles will change the operating range (ΔT) of the TES as this will be established by the capabilities of the solar field to heat the HTF to the highest temperature (T_H) while the demands of the power block will establish the lowest temperature (T_L) at which energy can be extracted from the TES. As discussed in the preceding section, the introduction of nanoparticles into Hitec-Solar Salt was meant to produce composite nanofluids that had improved specific heat capacities.

Figure of merit for DOE thermal energy storage media on a [$/kWht] Basis

$$\text{MediaCosts}[\frac{\$}{kWh_t}] = \frac{\text{MaterialCosts}[\frac{\$}{kg}]}{\text{Average}C_p[\frac{kJ}{KgK}]\times\Delta\text{T}[K]\times 2.778E(-4)[\frac{kWh_t}{KJ}]} \quad (3)$$

The purpose of this research was to determine if the introduction of alumina nanoparticles into Hitec-Solar Salt offers a cost-effective improvement in the specific heat of thermal energy storage material. Fig. 3 shows the results of a parametric study into the potential cost benefit of introducing nanoparticles into Hitec-Solar Salt. Four different curves representing 0%, 10%, 25% and 50% increases in material costs due to the introduction of nanoparticles are plotted as a function of theoretical improvement in the TES materials specific heat. The normalized media costs are plotted as the dependent variable for this parametric study. From the plot, it is possible

to determine that a composite material produced at a 10% higher manufacturing cost with a specific heat 1.5 times higher than that of the base Hitec-Solar Salt yields more than a 25% savings with respect to the current Solar Salt TES material. Similarly, a new TES material which demonstrated a 30% increase in specific heat similar to that observed by Nelson would offer a 15% savings if it could be produced at only a 10% higher material cost. If the cost of producing the material were to increase by 30% or more, there would be no advantage to the new material. The predicted cost increase for each of the measured mass concentrations is given in Table 3.

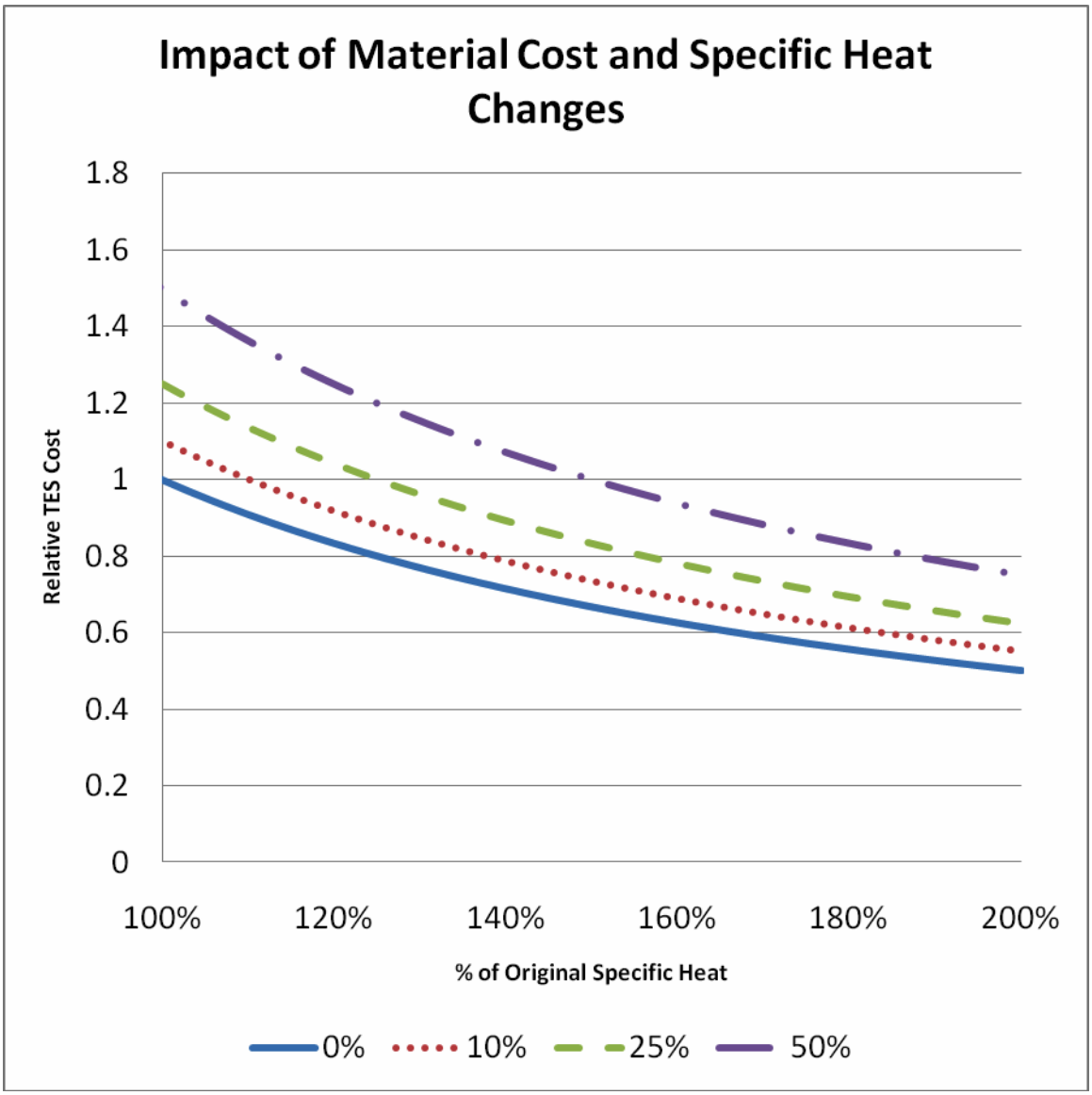

Figure 3. Relative TES material costs due to the percent improvement in specific heat for a given percent increase in manufacturing costs % Increase in Material Cost Relative to Base Material.

Table 3. Predicted cost increase (%) for the created Hitec- Solar Salt and Al_2O_3 high temperature nanofluids.

Mass fraction Al_2O_3	**Increase in Material $/kg Cost**	**C_p Increase for 20% $/Whr$_t$ Reduction**
0.1%	0.9%	126%
1.0%	8.8%	136%
10%	87.6%	235%

In addition to lowering the TES material costs on a $/kWht basis, improving the specific heat of the material results in secondary systems savings due to the need for smaller tanks, foundations, less insulation, etc.

2.2.1.2 Thermal Conductivity

Since Choi [10] first defined nanofluids, many experiments have shown anomalous enhancement of thermal conductivity of nanofluids compared with the corresponding base fluids. Eastman et al. [11] measured the thermal conductivity of nanofluids containing Cu and CuO nanoparticles with two different base fluids: water and HE-200 oil. A 60% improvement in thermal conductivity was achieved with only 5% volume fraction of nanoparticles compared to the corresponding base fluids. Lee et al. [12] reported a 20% enhancement of thermal conductivity of suspended CuO nanoparticles in ethylene glycol at 4% volume fraction of nanoparticles. Kuznetsov [13] presented a study on the thermal conductivity of nanofluids consisting of Al_2O_3, SiO_2, and TiO_2 nanoparticles and water. The measured data showed that the three suspended nanoparticles increased the thermal conductivity of the base fluid by 15%, 20% and 40%, respectively. Wang et al. [14] presented investigations of the increase of thermal conductivity with the introduction of CuO and Al_2O_3 nanoparticle in water, ethylene glycol, vacuum pump oil and engine oil. Experimental data showed that the thermal conductivity of the nanofluids increased as the volume fraction of the nanoparticles increased.

2.2.2 Material Stability

An important factor in choosing a suitable TES medium is that of stability of the nanoparticle enhanced eutectic salt mixture. Both chemical reactivity (decomposition) and the physical stability of the mixture are considered. Chemical decomposition can be determined through thermal testing. The nanoparticle enhanced eutectic salts are presumed to be an uniform distribution of particles within the salt. Long-term particle settling and particle agglomeration will affect the properties of the mixture.

For settling particles that are considered individually, i.e. dilute particle solutions, there are two main forces enacting upon any particle: gravity, and a drag force that is due to the motion of the particle through the fluid. Gravity is usually not affected by the particle's velocity, whereas the drag force is a function of the particle’s velocity. [15]

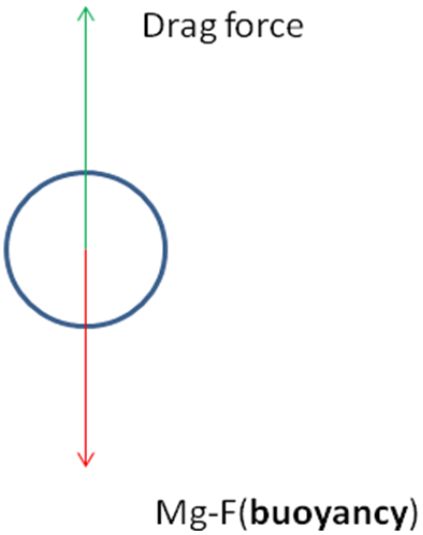

Figure 4: Force analysis of nanoparticles' settling down process

A particle at rest will experience no drag force, which causes the particle to accelerate due to gravity. When the particle accelerates, the drag force acts in the direction opposite to the particle's motion, retarding further acceleration; in the absence of other forces, the drag force directly opposes the body force. As the particle increases in velocity eventually the drag force and the applied force will approximately equate, causing no further change in the particle's velocity. This velocity is known as the terminal velocity, settling velocity or fall velocity of the particle. This is readily measurable by examining the rate of fall of individual particles. [16]

The terminal velocity of the particle is affected by anything that will alter the particle's drag. Terminal velocity is most notably dependent upon grain size, the shape (roundness and sphericity) and density of the grains, and the viscosity and density of the fluid in which the grains are suspended. [16]

For dilute suspensions, Stokes' law predicts the settling velocity of small spheres in a fluid. This is due to the strength of viscous forces at the surface of the particle, which provide the majority of the retarding force on the particle. Stokes' law finds many applications in the natural sciences, and is given by:

$$w = \frac{2(\rho_p - \rho_f)gr^2}{9\mu} \qquad 4$$

here ω is the settling velocity, ρ is density (the subscripts p and f indicate particle and fluid respectively), g is the acceleration due to gravity, r is the radius of the particle and μ is the dynamic viscosity of the fluid. [16]

To calculate the settling rate for alumina nanoparticles in a typical molten TES, assume the following literature values: for the density of alumina, $\rho_p = 4 g/cm^3$; for the molten salt, $\rho_f = 1.83 g/cm^3$ and $\mu = 0.235 \times 10^{-2}$ (PaS). Then, $\omega = 2.01 \times 10^6 r^2$.

The time for a 20-micron cluster of nanoparticles to settle in a test cylinder 3 inches high was calculated to be 16 hours. This shows that while well-dispersed nanoparticles are stable, clusters tend to settle quickly with time. Consider that the size of the nanoparticles/Nano clusters in the test sample ranges between 30 nm and 10 microns in size. Any cluster of size greater than 10 microns would settle faster than the 10-micron particles. The time taken for all the 10 micron clusters to settle through a distance of 3 inches in the test cylinder due to gravity is 20 hours. If the radius of alumina nanoparticles is 15nm, r = 15nm and the length of the test cylinder is 3in = 76.2mm, the expected settling time for 15 nm alumina particles in a molten TES salt is 46803 hours or1950 days, which is more than 5 years. If the size of the particle is smaller, the time will be even longer. Well-dispersed alumina nanoparticles will stay evenly in the fluid rather than settling quickly to the bottom.

2.3 Nanoparticle Enhanced Material Compatibility

The driving force of corrosion is the lowering of free energy associated with the oxidation of a metal. Thermodynamics examines and quantifies this driving force. It predicts if reactions can or cannot occur (i.e., if the metal will corrode or be stable). It does not predict at what rate these changes can or will occur: this is the area of kinetics. However, knowing from thermodynamics what reactions are possible is a necessary step in the attempt to understand, predict, and control corrosion. Though this TES project will not be investigating the kinetics of such reactions, P.H. Suegama et al [17] have shown that silica nanoparticles induce reactions that reduce corrosion. One way to improve the thermophysical properties of a molten salt is by adding silica nanoparticles and a useful byproduct of this addition is an expected reduction in corrosion. Molten fused salts have been shown to be more corrosive than aqueous salt solutions [18]. One way to decrease the corrosion rate of molten salts is by reducing the oxidizing power of the salt with additives. In this TES project, these additives are nanoparticles whose primary purpose is to improve the thermophysical properties of the salt. We hypothesize that these additives (nanoparticles) will also reduce the oxidizing power of the salt.

The metal subject to corrosion in this test is SS304, a material commonly used for containment in CSP plants. The typical composition of SS304 is Mn 2, Ni 9.25, Cr 19, Si 1, C 0.08, P 0.045, S 0.03, and Fe balance [19].

The proposed corrosive materials are the carbonate eutectic with and without silica nanoparticles (1% by weight).

2.3.1 Corrosion and Its Mechanisms

Corrosion involves the interaction between a metal or alloy and its environment. Corrosion is affected by the properties of both the metal or alloy and the environment. The most important environmental variables include: pH (acidity); Oxidizing power (potential); Temperature (heat transfer); Velocity (fluid flow); and Concentration (solution constituents). While corrosion obeys well-known laws of electrochemistry and thermodynamics, many variables that influence the behavior of a metal in its environment can result in accelerated corrosion in a given case and complete protection from corrosion in a largely similar case.

2.3.1.1 Mechanisms of Molten Salt Corrosion

Adler et al, [18]**,** have described two general mechanisms of corrosion that exist in molten salts. One is metal dissolution caused by the solubility of the metal in the salt. This dissolution is similar to that in molten metals, but is not common. The second, more common mechanism is the oxidation of the metal, which is similar to aqueous corrosion. For this reason, molten salt corrosion has been identified as an intermediate form of corrosion between molten metal and aqueous corrosion.

General, or uniform, metal oxidation and dissolution is a common form of molten salt corrosion, but is not the only form of corrosion seen. Selective leaching is very common at higher temperatures, as are pitting and crevice corrosion at lower temperatures. All the forms of corrosion observed in aqueous systems, including stress-assisted corrosion, galvanic corrosion, erosion-corrosion, and fretting corrosion, have been seen in fused salts. Electrochemically, the molten salt/metal surface interface is very similar to the aqueous solution/metal surface interface. Many of the principles that apply to aqueous corrosion, such as anodic reactions leading to metal dissolution and cathodic reduction of an oxidant, also apply to molten salt corrosion. Based on this concept, recent studies have been successful in using electrochemical test methods commonly used in aqueous solutions (e.g., electrochemical noise, linear polarization, and harmonic distortion analysis) to make measurements of corrosion and localization in laboratory studies. This work has even been carried on to use in commercial plant operations to help relate changes in process variables to periodic conditions of accelerated corrosion [18].

The acid - base behavior of the melt is very similar to that of its aqueous counterpart. The corrosion process is mainly electrochemical in nature because of the excellent ionic conductivity of most molten salts. Some investigators think that dissolved water enhances the electrochemically corrosive nature of such molten salts.

Even though the corrosion mechanism is similar, there are major differences between molten salt and aqueous corrosion. The differences arise mainly from the fact that molten salts are partially electronic conductors as well as ionic conductors. This fact allows for reduction reactions to take place in the melt as well as at the metal/melt interface. This behavior also allows an increase in frequency of cathodic reactions and can therefore lead to a substantial increase in corrosion rate over a similar electrochemically controlled aqueous system, especially if the corrosion media contain very few oxidants. Because of property differences between water and molten salt, the rate-controlling step in most molten metal systems is ion diffusion into the bulk solution, not the charge transfer reaction that is typical of aqueous systems. Molten salt systems operate at higher temperatures than aqueous systems, which lead to different forms of corrosion attack.

Electrochemical measurements have highlighted these differences between aqueous and molten salt environments, particularly in terms of characterizing their polarization through the classical Stern-Geary relationship. Values obtained in a molten salt system tend to be much different than those observed in an aqueous system, brought about by the simultaneous presence of many ionic species and the combined ionic and electronic conduction mechanisms in molten salts. However, use of these techniques has resulted in meaningful measurement of corrosion rates that correlate with actual mass losses in system components in combustion environments [18].

The paourbaix diagram (Figure 5) shows possible corrosion reactions for iron corroding in a molten carbonate salt. This diagram is key to understand the corrosion dynamics.

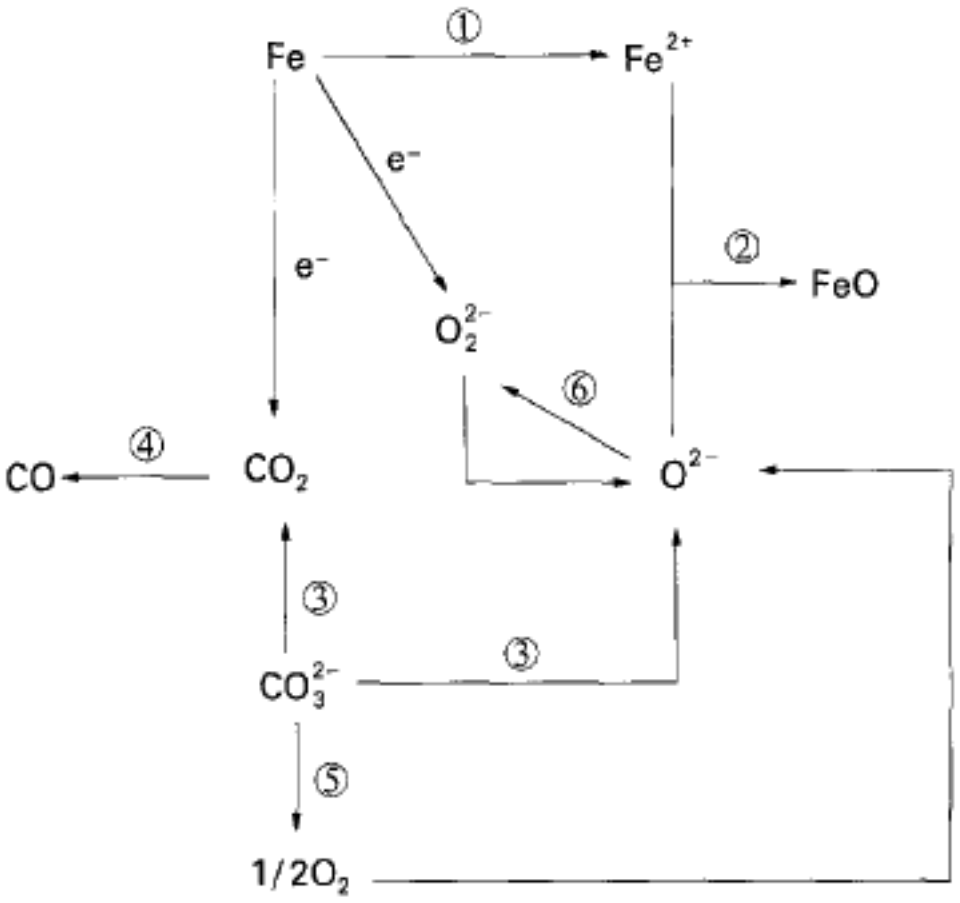

Figure 5. Paourbaix diagram of iron in molten carbonate salts (taken from [20]

The regions of immunity, corrosion and passivation of a metal in aqueous solutions can be assessed from the so-called Paourbaix diagram (potential-pH diagram). Bearing in mind that the oxygen anion is most likely to be reduced during the partial cathodic reaction, potential – pO^{-2} diagrams were devised in analogy to this treatment for a range of metals in molten salt electrolytes to define the zones of corrosion and passivation. It is known that the dissociation of oxygen-containing anions gives rise to a well-defined acid-base behavior.

$SO_4^{-2} = SO_3 + O^{-2}$ ---------- (R1)

$NO_3^{-} = NO_2^{-} + O^{-2}$ ---------- (R2)

$CO_3^{-2} = CO_2 + O^{-2}$ ---------- -- (R3)

$2OH^- = O^{-2} + H_2O$ ---------- (R4)

In accordance with the Lux-Flood theory [20], oxygen containing anions acts as a base in the supply of oxide anions, and the corresponding gas oxides are their conjugate acids. From the above equilibrium it follows that the acidity of the melt may be expressed by pO^{-2}. Accordingly, the *E*/pO^{-2} diagram provides a suitable framework for determining passivation zones and the electrochemical behavior of different metals. This passivation zone is considered a direct measure of the amount of corrosion, which in turn determines the corrosion rate. Thus removing the passivation layer and normalizing with time will lead to corrosion rate. This method of determining corrosion rate by removing the passivation layer is termed a "gravimetric or mass loss" method of determining corrosion rate.

In the diagram, the carbonate anion breaks as in reaction R3. This provides O^{-2} for oxidation/corrosion of iron. It is expected that nanoparticles will reduce the oxidizing power of the melt and hence form adducts. An adduct is a chemical compound that forms from the addition of two or more substances. The adduct forms a passivating layer and inhibits corrosion [17]. It is expected that silica nanoparticles will form a passivating layer by forming an adduct which is stable and also that this adduct is formed by transforming less parent material compared to the adduct formed without silica nanoparticles. On descaling, the mass loss normalized with time and area will be a direct indicator of the corrosion rate.

2.3.1.2 Thermodynamics and Kinetics of Chemical Oxidation of Metals

Market Research Report [21], has reported that the thermodynamic feasibility of a corrosion reaction is determined by the change in free energy of the system during the corrosion process.

$Me + 1/2O_2 \rightarrow MeO$

However, such determinations can also be made by comparing the dissociation pressure of the oxidation product and the partial pressure of oxygen. If the partial pressure of oxygen is less than the dissociation pressure of the oxidation product the backward reaction progresses and vice versa. Corrosion takes place if the forward reaction is favored, forming an oxide film. Conditions for film continuity are determined as follows. Let V_{Ox} be the volume of oxide formed and V_{Me} be the volume of the metal. If $V_{Ox}/ V_{Me} > 1$, generally films form with good protective properties.

Film growth generally follows 3 laws: a linear law, a parabolic law, and a logarithmic law.

The linear law is $V_{Ox}/ V_{Me} < 1$, and $dy/dt = K$, where y is the film thickness. This implies "y" is proportional to the oxidation time.

Linear Law:

$Y = Kt + A$

All alkali metals undergo this type of corrosion.

The parabolic law is $V_{Ox}/ V_{Me} > 1$. The corrosion process will be retarded by diffusion of corrosion products through the film. This results in thickening of film that continuously decreases the corrosion rate with time.

Parabolic Law:

$y^2 = Kt + A$

Iron oxides typically observe a parabolic law of film growth. Cu, Fe, and Ni also follow this growth pattern.

For iron the expected rate of corrosion is parabolic [22]**.** The expected parabolic behavior is seen in Figure 6.

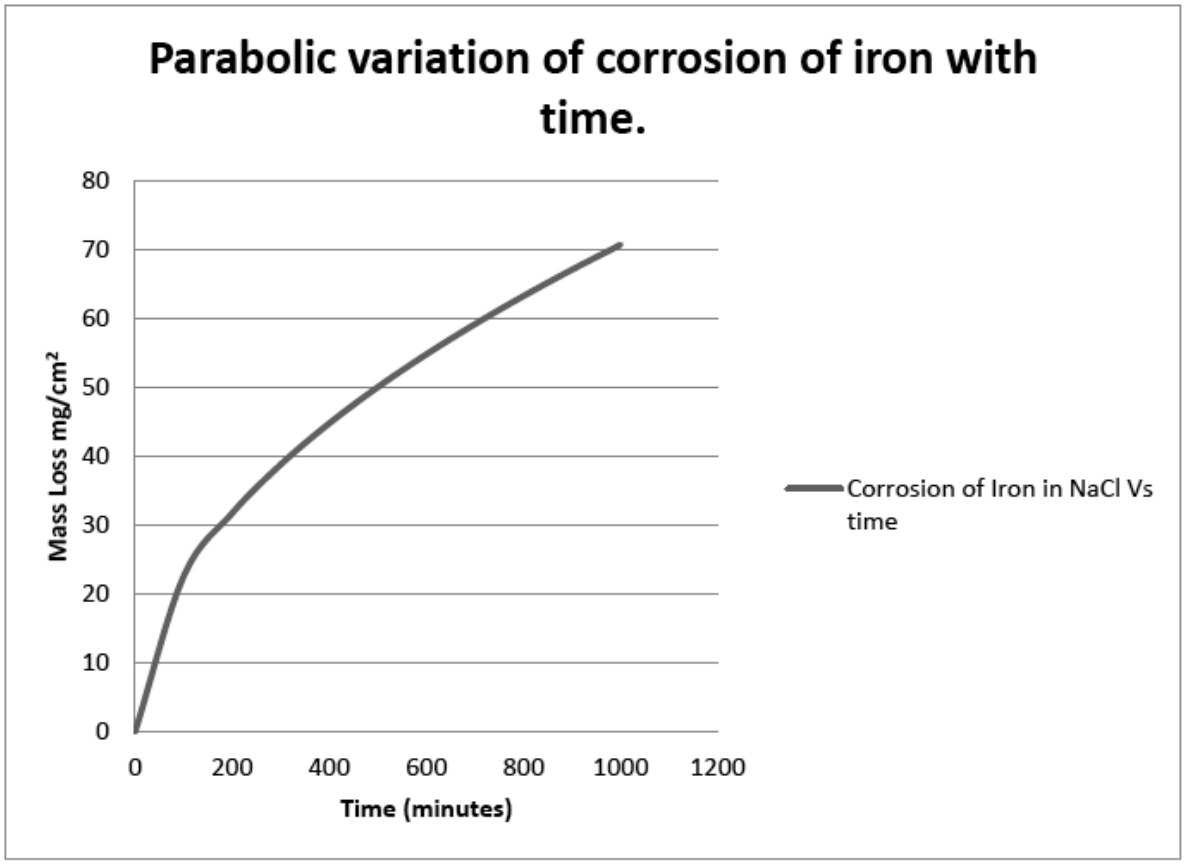

Figure 6: Corrosion Characteristics of Iron with Time [22].

The logarithmic law is much slower than predicted by parabolic law. The parabolic growth rate is $dy/dt = Ke^y$. The logarithmic growth rate is $y = \ln (Kt)$

Al, Cr and Zn follow the logarithmic law during corrosion. Iron in particular follows a logarithmic law up to 400° C but a parabolic law from 500° C to 1100° C. Mass loss and corrosion are determined as follows: as discussed, the film growth on the surface of the metal

due to corrosion is a result of the transformation of the base metal into oxides. The "term mass" loss indicates the mass of metal transformed into oxides. Thus, mass loss is one way to quantify corrosion rate. In particular, normalized mass loss per unit area per unit time is a very good indicator of the rate of corrosion. Molten salt corrosion rates are predominantly determined gravimetrically [18]. Other quantifying techniques include electrochemical noise, linear polarization, and harmonic distortion analysis, but only mass loss was used in this research.

Corrosion is an electrochemical process whose rate can be quantified several ways. Ideally, rate of corrosion is measured using an electrochemical cell, where the metal whose corrosion rate is to be determined is set up as the anode, the corroding environment/agent is the electrolyte, and the corrosion product is formed at the cathode. The corrosion current is directly proportional to the rate of corrosion. The concept of polarization potential is also used in determining the rate of corrosion. The corrosion rate typically follows a Gaussian distribution [23].

In addition to the above methodologies, the concept of anodic mass loss directly measures the rate of corrosion. As the experimental setup demonstrates, the anode and cathode are essentially the same steel coupon, and the surrounding molten salt acts as a corroding environment and completes the electrochemical circuit. After the experiment, when the steel coupon is descaled with hydrochloric acid, the acid removes all the oxides formed and leaves the steel coupon alone. This method has been detailed in [19]**.** Bradshaw et al have shown that the time of exposure to the environment must be large enough to capture oxide-metal interface. The average time of exposure is about 300 - 1000 hours.

The rate of corrosion can be used to identify and classify the operability of steel into various categories. This classification per Cabeza et. al [24] will be used as a basis to give recommendations to DOE. This table of classification is as below (Table 4).

Table 4: Corrosion Rate and their Operability in Industries. [24]

Corrosion Rate in $mg/cm^2/yr$	Corrosion Rate in mm/yr	Recommendation
> 1000	> 2	Completely destroyed within days
100 to 999	0.2 – 1.99	Not recommended for service greater than a month
50 to 99	0.1 – 0.19	Not recommended for service greater than one year
10 to 49	0.02 – 0.09	Caution recommended, based on specific application
0.3 to 9.9	NA	Recommended for long term service
< 0.2 NA	NA	Recommended for long term service; no corrosion, other than as a result of surface cleaning, was evidenced

2.4 System Modeling

A Concentrated Solar Power Plant usually consists of four subsystems: a solar collection field, a thermal storage system, a heat engine and electricity generator, and related pipes and heat exchangers as shown in Figure 1.

A solar thermal power plant performance simulation model has been built based on Matlab/Simulink. It calculates the electricity generation amount according to information such as the project's location, weather situation, direct normal irradiation, project configuration, and so on.

An economic model has been built based on Matlab. It calculates the cost of electricity or electricity sale price based on the annual electricity generation amount (from performance model), installation and operation costs, type of financing, tax rate, applicable tax credits and incentives, customer requirement and so on. These two models can work together and they provide the capability of running a batch of simulations to compare and analyze results at the same time.

A risk analysis model considers the faults that may happen in the solar thermal plant and calculates their probabilities. It helps identify potential and most probable problems the system may have, and the economic loss that may be caused by various problems. This calculation is heavily based on the detailed configuration of system and the result of previous two models. Decision tables, fault tree and event tree will be generated and plotted during the analysis procedure.

3 Materials and Methods

3.1 Eutectic Salt Mixtures

An extensive literature survey was conducted of the thermodynamic properties of mixed salt eutectic mixtures. Based on the goal of developing improved higher temperature materials, a 42.7 % lithium carbonate / 57.3 % potassium carbonate eutectic mixture was selected for investigation. The material has a melting point of 489° C

After DOE expressed the desire to concentrate on reducing the cost of the TES without increasing the operating temperature above 400° C, sodium nitrate/potassium nitrate eutectics were chosen for investigation. Hitec Solar Salt 55 mole% sodium nitrate/45 mole% potassium nitrate has a melting point of about 220 °C.

3.1.1 Existing Materials

The current standard thermal energy storage material is a nitrate eutectic, comprised of sodium nitrate and potassium nitrate. This material works well, as it has a low melting temperature, a moderate specific heat, and moderate thermal conductivity. The nitrate eutectic is used only in its liquid phase, and has been applied in thermoclines and two-tank systems for more than 40 years. Several variants of the basic form exist under trade names, such as Hitec solar salt and Hitec XL. The important physical properties of these composites are listed in Table 5.

Table 5: Reference Thermophysical Values for the Hitec Solar Salt by Coastal [25]. (As a point of comparison, water has a specific heat of 4.18 J/gK.)

	Hitec Solar Salt	Units
Specific Heat	1.55	J/gK at 350C
Heat of Fusion	132.58	J/g
Melting Point	222	°C

3.1.2 Standard Nitrate Eutectic

The standard nitrate eutectic compound chosen for this investigation has the industry name "Hitec Solar Salt", and is manufactured by Coastal Chemical. This particular eutectic is a blend of sodium nitrate ($NaNO_3$) and potassium nitrate (KNO_3), with a 55% $NaNO_3$ molar ratio blend. The eutectic diagram is shown in Figure 7. The Hitec eutectic provides close to the minimum melting temperature of any mixture of the two eutectic components. This is desired as the nitrate eutectic is not designed to function as a thermal energy storage material in both the solid and liquid phases, but rather functions exclusively in the liquid phase. Hitec is used in several existing facilities and is available in significant quantities for a low cost. The heat of fusion for various eutectic fractions is shown in Figure 8. The reference specific heat of the chosen nitrate eutectic is shown in Figure 9.

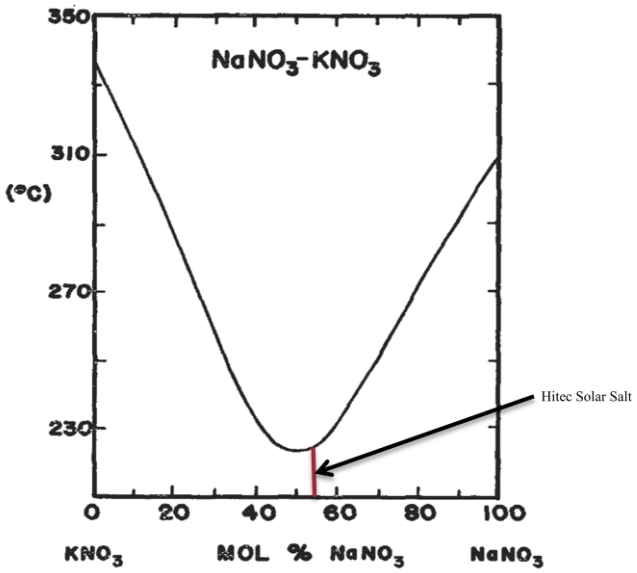

Figure 7: Nitrate eutectic diagram by Janz *et al*. [26].
The red line shows the mixture point of Hitec solar salt. The mixture point of Hitec is near the minimum melt temperature of any mixture.

Composition (mol % KNO_3)	ΔH_f° (kcal mol^{-1})	T_m (°C)
0	3.600	310
25	3.382	275
40	3.290	243
50	3.195	227
60	3.100	230
75	2.802	260
87	2.685	300
100	2.300	337

Figure 8: Heat of fusion for various nitrate eutectic mixes by Janz *et al*. [27].
The Hitec solar salt mixture is at 55% sodium nitrate, so the heat of fusion is between the 50% and 60% mixture heat of fusion value.

T (K)	C_p (cal $K^{-1}mol^{-1}$)	T (K)	C_p (cal $K^{-1}mol^{-1}$)
510	39.99	650	36.29
520	39.72	660	36.03
530	39.46	670	35.77
540	39.19	680	35.50
550	38.93	690	35.24
560	38.67	700	34.97
570	38.40	710	34.71
580	38.14	720	34.45
590	37.88	730	34.18
600	37.61	740	33.92
610	37.35	750	33.66
620	37.08	760	33.39
630	36.82	770	33.13
640	36.56		

Figure 9: Reference specific heat values for a 50% sodium nitrate eutectic by Janz *et al*. [27].
The Hitec solar salt is a 55% sodium nitrate eutectic, so the values will be slightly different.

The strengths of the nitrate eutectic are based around its use as a sensible-only thermal energy storage medium. The material is thermally stable for long periods in the liquid phase. The material has a low melting temperature of about 220° C. The material has a specific heat in the liquid phase of about 1.55 J/gK. The material is relatively cheap and available in large quantities, making potential manufacturing of a nanoparticle composite material an easier task. The eutectic components are generally non-toxic and non-flammable, so a spill or rupture would be less dangerous for the environment around a CSP facility than thermal oils. The material is solid under ambient conditions, but highly soluble in water, making cleanup from a spill much easier, unless it is raining. The weaknesses of the nitrate eutectic are more due to long-term operational

concerns than thermal property issues. The eutectic has a relatively low decomposition temperature, observed to be around 500° C, as shown by Peng *et al*[28]. The nitrate is highly corrosive, requiring additional maintenance and replacement. The material is hydrophilic, and will absorb water from the atmosphere if left in an open container.

3.1.3 Carbonate

Materials used for thermal storage should have a high energy storage density. This reduces the size of the storage vessel and the related material cost, thus making the TES system economically sound. Among the various TES materials, alkali carbonates are a good candidate for thermal energy storage in high temperature applications. They have a high energy storage capacity, good thermal conductivity, low corrosiveness, moderate cost, and safe and simple handling procedures [29]. The carbonate eutectic that was investigated is a eutectic of lithium carbonate and potassium carbonate. The phase diagram for the eutectic is shown in Figure 10. The eutectic is composed of 62 mole % lithium carbonate and 38 mole % potassium carbonate. The eutectic of this composition has a melting point of 488° C. The melting points of the pure components, lithium carbonate and potassium carbonate, are 723° C and 898° C respectively [30]. Such a high melting point allows high temperature thermal energy storage and results in a high Rankine cycle efficiency of the power plants. One property of phase change materials that considerably impacts thermal storage devices is the change in the volume of the material at phase transition. The volume of carbonate eutectic increases by 8.5% when it melts, which is not very high, and is well within the allowable range.

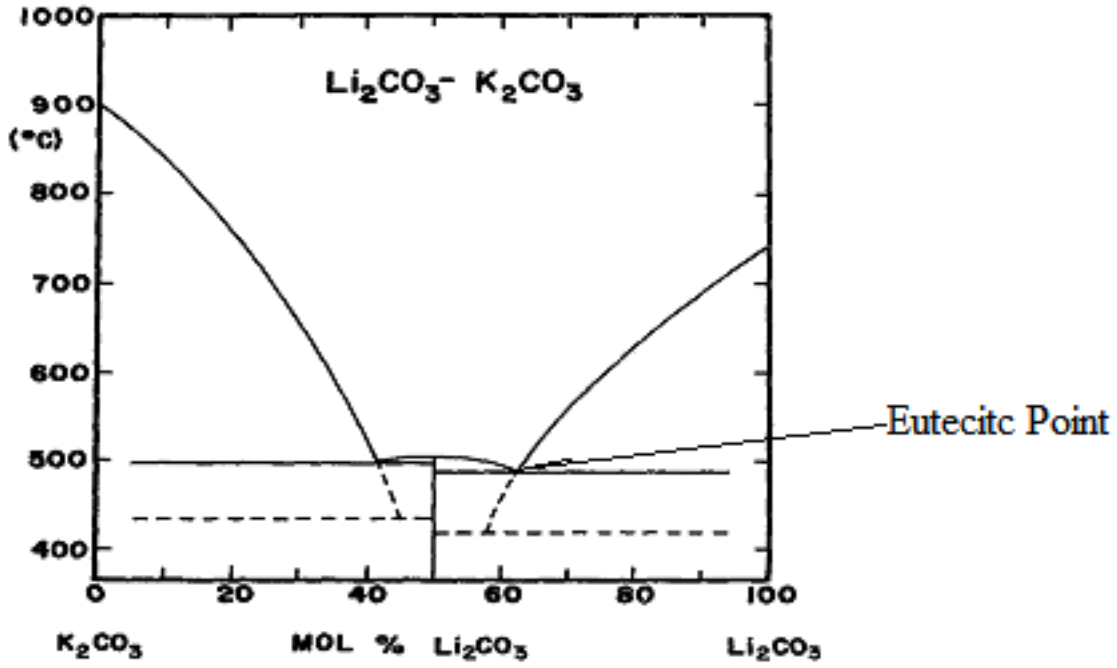

Figure 10: Phase diagram of lithium carbonate and potassium carbonate [30]

3.2 Nanoparticle Augmentation

Many papers have been published in discuss the effects of adding nanoparticles to substances to change their properties. Some discuss how best to change the physical properties of substances, such as strength or conductivity, others show how best to modify a fluid to suit a given purpose. In particular, there have been many studies on changing the thermal properties of water. The studies used to design this investigation have looked at changing the specific heat and the thermal conductivity of aqueous solutions by doping them with various concentrations of nanoparticles. These papers described a wide variety of tests to determine thermophysical properties, but the overall view is that the addition of small concentrations of nanoparticles will significantly change the thermal properties of water.

3.2.1 Nanoparticle Selection

Research by others, such as Easterman *et al*. [31, 32], Wang [33, 34], Zhou [7, 35], and Sundar [36] has shown that small additions of certain nanoparticle types seem to influence the thermophysical properties of water to a varying degree, based on the nanoparticle material and the concentration of nanoparticles, using a variety of manufacturing methods. Using these publications, it was concluded that the best options for improving the thermophysical properties of the nitrate eutectic were alumina (Al2O3) and silica (SiO2). The observed water thermal properties showed the addition of nanoparticles reduced the specific heat but increased the thermal conductivity of the eutectic. The drop in specific heat is expected given the large disparity in the specific heat of water and the specific heat of the bulk material form of the nanoparticles. Additionally, others such as Likhachev [37] and Wang [33, 34] have observed that the specific heat of nanoparticles of a given material can be significantly higher than the bulk form of the same material. Unfortunately, no specific papers were found that describe the specific heat of the nanoparticles, only of the bulk material.

Material compatibility issues also affected the selection of nanoparticle salt mixtures after it was observed that nitrate salts reacted vigorously with carbon nanotubes when heated. Carbon nanotube carbonate mixtures were stable.

3.2.2 Mass Percentage Selection

A variety of published works [7, 31, 32, 33, 34, 35] have shown that there is an anomalously large effect at low nanoparticle mass concentrations when altering the thermal properties of a base material. For water, these values typically range between 0.1% and 5% by volume. To simplify the testing process, a single mass percentage was chosen and set to 1% for most of our study. We did perform several experiments in which the mass percentage of nano particles was varied from 0 to 1.5%, to observe the effect this variation had on specific heat. We found that the peak specific heat occurred at or near 1% mass of nano particles.

3.3 Material Preparation

3.3.1 Solar Salt Nanomaterial Fabrication

3.3.1.1 Solid Solution Mixing

Ball milling of the eutectic salt plus nanoparticle material to form a homogenous solid solution

was tried using a standard laboratory ball mill with steel balls and a stainless steel body. Material was loaded into the ball mill and agitated for up to two hours. The resulting mixtures were, in fact, not homogenous as shown by thermodynamic properties measurement and electron microscopy. Solid solution mixing of the eutectic salt and nanoparticles was abandoned quickly in favor of aqueous methods.

3.3.1.2 Aqueous Methods

To create the nanoparticle composite material requires several steps. The first step is combination, the second is mixing, and the third is water removal. The nitrate eutectic components are highly hydrophilic, so the material was prepared in a dry, argon-filled glove box. Later steps require the material to be in an aqueous solution, so the components were massed, then combined in distilled water to form the base aqueous eutectic. The base eutectic was purchased in the form of pre-mixed pellets, so these were crushed into a fine powder using a mortar and pestle before being added to distilled water. The solubility of the nitrate eutectic mandated a ratio of 10 mg of the eutectic per ml of solution. The chosen nanoparticles were alumina (Al_2O_3) and silica (SiO_2), and were added to the aqueous solution of the base eutectic. The nanoparticles were added such that they comprised 1% of the mass of the eutectic in the aqueous solution.

In order to ensure complete distribution of the nanoparticles into the eutectic, the aqueous solution had to be sonically mixed for a set duration of 2 hours, as that was the observed minimum time to fully dissolve the nitrate in the solution and qualitative observations suggest additional sonication would re-agglomerate the nanoparticles. Based on the limitations of the sonic mixers used, the standard batch size was about 2 g of composite material, as the largest standard container held 200 ml of water. This batch size was used to minimize the number of batches required to make sufficient test material for all the experiments. A larger batch size was found to be impractical, as the larger container required reduced the effectiveness of the sonic mixing and extended the drying time, which will be discussed next.

3.3.1.2.1 Evaporation

Once the nanoparticles were mixed into the aqueous solution, the material was transferred back to the glove box. Once in the glove box, the sample mixture was heated in a steel pan on a hot plate set to 90° C (Figure 11), so that the water would quickly evaporate out of the pan without actively boiling, leaving the nanoparticle composite material as a precipitate in the steel pan. To ensure the water would not simply be taken in again by the eutectic, several trays filled with desiccants were placed in another portion of the glove box. This setup was maintained until all the water was driven from the steel pan, and a fine-grain white powder was left coating the bottom of the steel pan. Since the material was precipitated out of the aqueous solution, it adhered to the steel pan, so it had to be removed physically. To accomplish this, a steel paint scraper was used to scrape the material from the pan, leaving a loose, white powder with the consistency of flour. The white powder was the final testing form of the nanoparticle composite eutectic. The material was then transferred from the pan to a container for later use, and stored in an oven at 140° C to ensure the processed material would not absorb water while in storage.

Figure 11: Process of water evaporation on a hot plate at 90°C

The use of nanoparticles created several significant challenges in the area of sample preparation. The largest challenge stemming from the small size of the nanoparticles was cross contamination of nanoparticles. In order to prevent cross-contamination, all samples were prepared in a cleaned glove box, and each nanoparticle type had its own tool set, meaning there was a steel pan and scraper used only for silica nanoparticles and another set used exclusively for alumina nanoparticles. This procedure was followed to ensure minimal cross-contamination, as even with extensive cleaning nanoparticles tend to remain on surfaces and tools with which they come in contact. A secondary concern was water absorption by the prepared samples. The thermal testing method requires little to no water in the sample material to ensure accurate results and to prevent machine damage. To prevent water absorption, the samples were kept in the dry glove box, and the samples were heated in a vacuum furnace up to 140° C for at least a day before being used in the thermal analysis machine.

3.3.1.2.2 Spray Drying

The batch drying method of preparation of the solar salt/nanoparticle mixtures for use as enhanced thermal storage materials in Concentrating Solar power Plants was deemed inappropriate for scale-up to the production of the large quantities of material needed for a pilot plant demonstration. Alternate methods for the production of large quantities were considered. Attempts to physically mix uniform solid solutions of solar salt and nanoparticles by ball milling had not yielded reproducible results. Flash evaporation of nanoparticles suspended in an aqueous solution of solar salt was considered a possible answer. Instead of introducing a stream onto a hot surface that could cause degradation of the material, it was decided to try a technique used in the food and drug industries to remove solvent from suspensions called spray drying. In spray drying, the slurry is suspended in a low boiling point solvent and introduced as an atomized mist into a heated air stream flowing coaxially with the mist. The solvent evaporates in the heated air stream, leaving solid particles of the suspension that are then collected from a cyclone separator. When the air flow and temperature are properly adjusted for the solvent suspension, the material will not become much hotter than the boiling point of the solvent. In this case, since water is

used as the solvent, the solar salt/nanoparticle mixture would not be subjected to temperatures in excess of a few degrees above 100° C.

A Büchi mini spray dryer Model B-290 (Figure 12) was used to synthesize the nanofluid mixtures that were used for the physical properties measurements reported below

Figure 12. Büchi Model B290 Spray Dryer

With a Büchi spray dryer, the air drying process can be modified by altering the temperature and volume of the air stream and the rate of liquid and gas flow through the aspirating nozzle. Initial tests of sample preparation using the air dryer were run with pure solar salt (60 mole percent $NaNO_3$ — 40 mole percent KNO_3). The volume of solution used for these trials was kept at 200 ml and the concentration of the salt in the aqueous solution was varied by ten-fold. This was done to gain experience with the system and to adjust the parameters.

The method used to prepare the materials for the air dryer was the same as previously used for the hot plate evaporation preparation method, namely dissolution of solar salt and alumina nanoparticles in water followed by sonication to disperse the nanoparticles. The working parameters for the spray dryer were maintained through all production runs: the solution/slurry feed rate was 5 ml/min through the dryer's integral peristaltic pump; the spraying air flow was set with the unit's rotameter to 473 l/h with a pressure drop of 0.41 bar (flow at STP 667 l/h); And the inlet temperature of the drying air was set to 220° C with a flow of about 37 m^3/h (both maximum settings for the dryer).

The air dryer method was used to synthesize nanofluids with nominal Al_2O_3 nanoparticle mass fractions of 0% (pure solar salt), 0.0625%, 0.125%, 0.25% and 0.5%. For this set of samples, the specific heat, melting point and heat of fusion were determined by using the DSC.

3.3.2 Carbonate Eutectic Preparation

3.3.2.1 Aqueous Methods

3.3.2.1.1 Evaporation

Similar methods to those described in section 3.3.1.2 were used to create an aqueous slurry of nanoparticles and dissolved carbonate salts.

First, the salt (base salt +nanoparticles) was dissolved in water. To speed up the process 4-oz vials were used to dissolve the salt in water. Second, the salt and the nanoparticles were mixed in the glove box with nanoparticles at 1% concentration by weight. One gram of mixture (salt + nanoparticles) was added to 100 ml of distilled water. Third, the resulting solution (salt and distilled water) was sonicated for 2 hours. Fourth, after sonication, the solution was transferred to an evaporating dish and evaporated in the glove box as described in section 3.3.1.2.1. On average, this evaporation process took 45 minutes. Fifth, after evaporation, the salt was scrapped off the evaporating dish, transferred to a clean, dry vial, labeled, and stored.

3.3.2.1.2 Low Temperature Vacuum Evaporation

A low-temperature preparation of a nanoparticle enhanced carbonate salt eutectic was prepared through vacuum distillation/sublimation. A sample consisting of 0.93 g of Li_2CO_3 and 1.07 g of K_2CO_3 was dissolved via sonication in a glass container in approximately 200 ml of water; 20 mg of silica nanoparticles were added to the carbonate solution and the mixture sonicated for 2 hours.

The solution was poured from the glass preparation vessel into an 8 x 8 in stainless steel pan, which was placed in a vacuum bell jar. The jar was sealed and the air pumped out to reduce the internal pressure. We used a liquid nitrogen cold trap to reduce the amount of water we put through the vacuum pump. Time and pressure were recorded with visual observation of the solution made through a viewing port in the bell jar.

When the bell jar was opened, spots of material were observed on the bottom and sides of the bell jar from splashing caused by the violent boiling. Sample yield was about 1.5 g.

Table 6: Observations of low pressure evaporation production method.

Time (min)	Pressure (torr)	Observation
0	830	Start run
5	295	Pan sample is liquid
10	185	Bubble formation in pan (degassing?)
15	100	Bubble formation (still degassing?)
20	48.5	Less bubble formation
25	19.0	Incipient boiling
30	7.0	Periodic large violent bubbles (boiling)
35	4.3	Observe sheet freezing rapidly covering pan
36	4.4	Triple point: liquid boiling with ice sheet on surface
41	4.1	Triple point
58	2.5	Solid ice in pan
117	1.9	Solid ice in pan
154	4.4	Solid ice in pan; Trap plugged; Bell jar isolated, trap removed and drained (about 2 inches of solid ice in trap inlet)
184	4.6	Vacuum line to bell jar reopened without liquid nitrogen in trap
1104	0.84	Ice gone; bell jar isolated, vented to atmosphere, opened and sample retrieved

3.4 Material Characterization

3.4.1 Differential Scanning Calorimetry (DSC)

Differential Scanning Calorimetry (DSC) refers to a thermal property determination technique. The technique uses a device called a differential scanning calorimeter. The general operating principle of the device is to compare the thermal energy input into two samples simultaneously. One sample is called the reference, the other is the actual sample to be measured. The standard setup is to make the reference an empty sample containment pan, and the measurement specimen is the unknown material in a sample containment pan. The recorded data output, usually called the heat flow, is the difference between the reference thermal energy input and the sample thermal energy input, which represents the difference in energy required to raise the temperature of the sample and reference items by the same quantity. The thermal energy difference between the sample and reference specimen is the energy required to raise the temperature of the unknown specimen by the same amount, as the energy required to raise the sample pan temperature is accounted for by the reference heat flow signal. There are two primary data outputs for standard DSC, heat flow and temperature. There are two methods to calculate a sample's specific heat from this information, ASTM 1269E and modulated differential scanning calorimetry (MDSC).

3.4.1.1 ASTM 1269E Testing

ASTM 1269E is the most widely accepted means of determining the specific heat of an unknown sample using a DSC. A sample measurement is comprised of three separate measurements: a baseline, a sapphire, and the sample. The baseline measurement is required to compensate for any calibration errors and any sample/reference pan mass differences. The sapphire run is used to determine the power required to heat a very well characterized material, as the specific heat of sapphire is known over a wide temperature range with high accuracy. The sample run is then compared to the sapphire run after factoring in mass differences between the two pans, the sapphire, and the sample. The temperature profile used with the ASTM 1269E method is shown in Figure 13. The described method results in 3 liquid phase measurements; heat of fusion measurements can be added after the specific heat measurements using the standard testing procedure outlined in ASTM 1269E, which is discussed in more detail later. These repeat measurements in the profile were done to ensure the reported values for a given sample were repeatable. Each of the repeat measurements was called a cycle, as the profile makes the DSC cycle through the same temperature range several times. Cycle 1 was the first such measurement, cycle 2 was the second, and cycle 3 was the third.

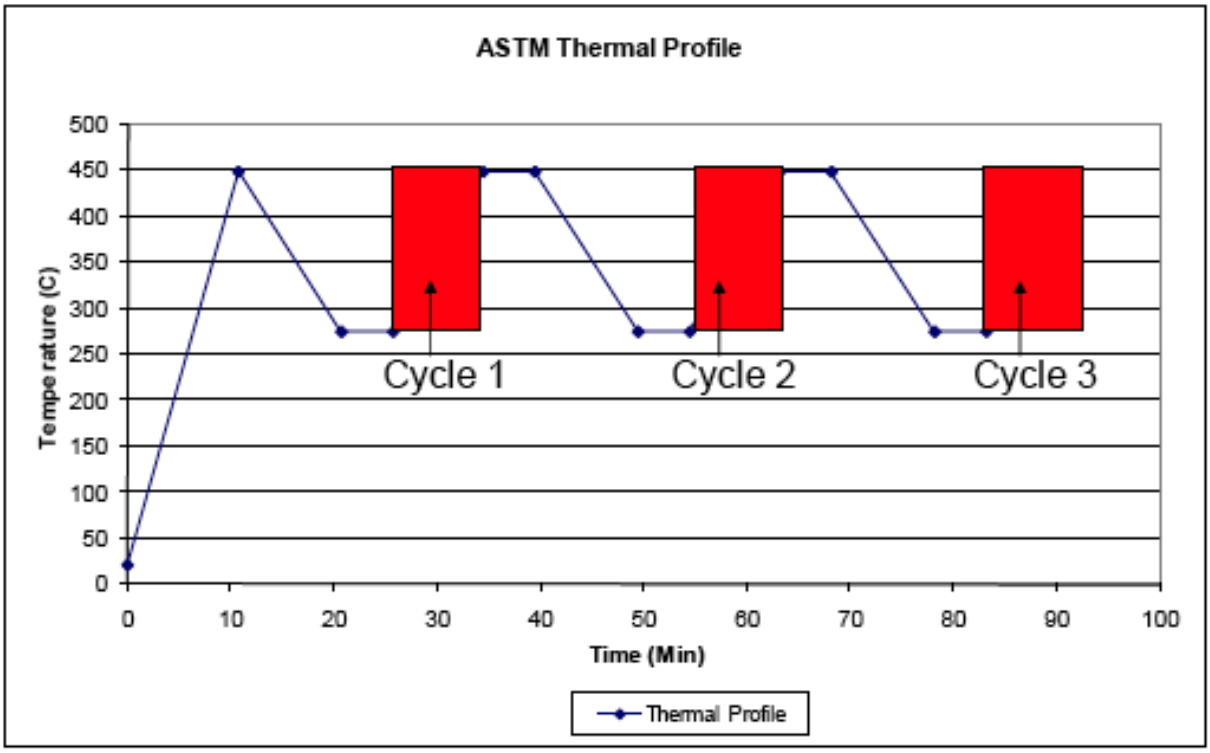

Figure 13: ASTM 1269E Test Temperature Profile.
The first temperature increase segment is called the "spike", as it is designed to melt the sample rather than measure data. The other three temperature increase segments provide data used to determine specific heat.

ASTM 1269E uses a series of equations, described below, to convert the heat flow signal from the DSC into the specific heat of the unknown sample. The equations use the results of all three runs previously mentioned (the baseline, sapphire, and sample runs) to determine the specific heat flow of the sample at a given temperature.

$$D_s(T) = S(T) - B(T) \quad (5)$$

$$D_R(T) = R(T) - B(T) \quad (6)$$

$$C_{ps} = C_{pr}(T)\cdot(D_s(T)\cdot M_R)/(D_R(T)\cdot M_S) \quad (7)$$

In Equation 5, D_s is the corrected heat flow of the sample at a temperature, S is the heat flow of the sample (of mass M_S) at a given temperature and B is the baseline heat flow at a given temperature. In Equation 6, D_R is the corrected heat flow of the reference at a given temperature, R is the heat flow of the reference (of mass M_R) at a given temperature. In Equation 7, C_{ps} is the specific heat of the sample at a given temperature, and C_{pr} is the specific heat of the reference at a given temperature. This equation set is sometimes referred to as the ratio method. There is a provision in ASTM 1269E to include the effects of pan mass on the computed specific heat, but due to the requirements of the MDSC method, the pans were mass matched for the ASTM tests as well. This negated the need to apply the more complicated ASTM 1269E method, and allowed the use of Equations 5, 6, and 7 in its place.

3.4.1.2 MDSC Testing

An alternative method to find the specific heat of a sample was Modulating Differential Scanning Calorimetry (MDSC). This method was created by Thermal Analysis (TA) a DSC designer and manufacturer; their Q200 and Q2000 DSCs support this option. This method superimposes a sinusoidal temperature variation over a fixed temperature increase rate. Using the sinusoidal temperature response of the sample and reference pans, the specific heat of the sample can be found. The applicable ASTM standard is ASTM E2716, which was followed where allowable. While the ASTM 1269E method can be run on any DSC, including a MDSC, the MDSC method can only be run on a suitable TA DSC with the MDSC option, as the MDSC method requires a different set of sensing hardware to detect very small changes in temperature and heat flow. The additional hardware and internal calculations give the MDSC method additional outputs over the standard ASTM 1269E method. The MDSC method has a direct data output of heat flow, temperature, and specific heat.

To verify the accuracy and precision of the MDSC method at the required temperature range, a series of tests were performed using the standard DSC calibration sample material, namely sapphire. A single sapphire sample was placed in the sealed hermetic aluminum pans used for the nitrate tests. The temperature profile for the sapphire runs was determined by a thorough review of TA's documentation and internal testing of the method. A standard MDSC test temperature profile can be seen in Figure 14. The sapphire sample was run four times to determine the precision and accuracy of the MDSC method. The results of these tests can be seen in the MDSC High Temperature Validation Results section, which clearly shows that the method is both highly accurate and highly precise. A more thorough analysis is presented later, in the Results section.

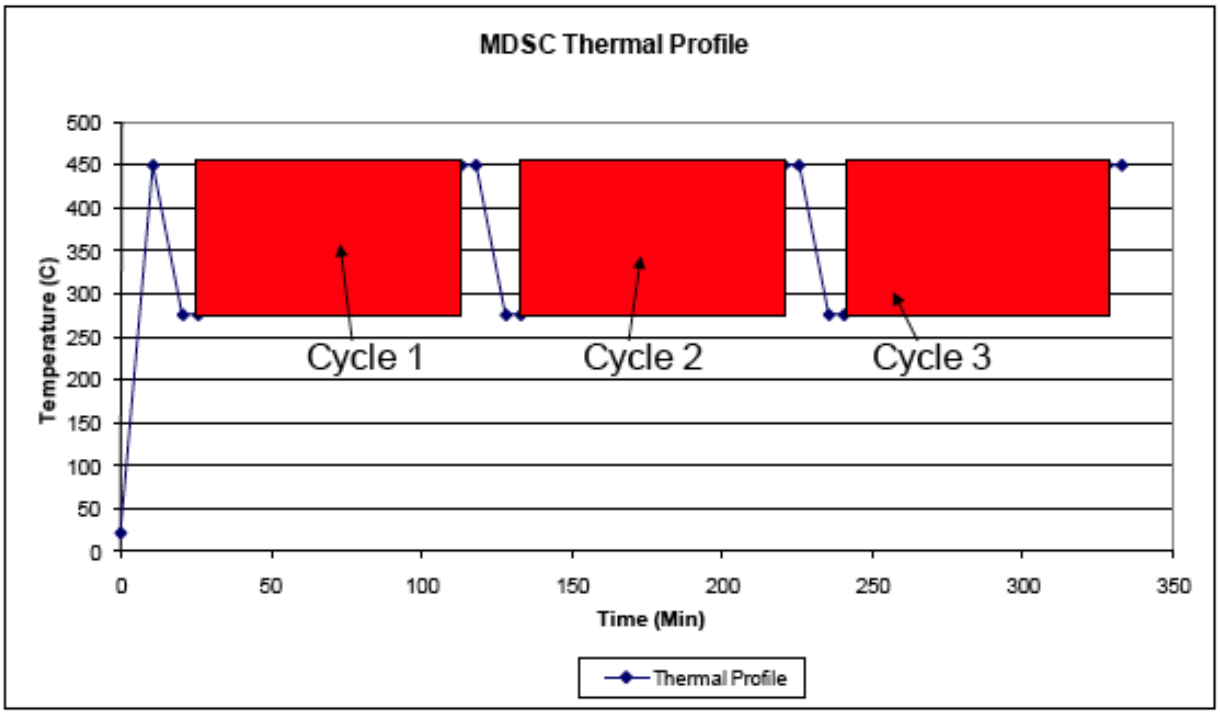

Figure 14: MDSC Temperature Profile.
Like the ATSM temperature profile, there are four temperature increase segments, three of which are used to gather specific heat data.

Due to the superbly accurate and precise measurements obtained using the MDSC method with the sapphire samples, testing was extended to the nitrate eutectic, but with modifications. In particular, the measured temperature range was reduced, as the CSP system operational temperature range is only from approximately 300° C to 600° C. The modulation was set up with a 1° C amplitude and a 120 second period. This method was created to minimize the phase change effects in the run data while still allowing for data collection during a phase change in order to find the heat of fusion after specific heat measurements had been taken. Multiple repeats in the liquid phase allow for confidence in the data for a particular sample. Preliminary qualitative testing showed minimal changes in the sample distribution within the sample pan after multiple freeze/melt cycles, but multiple heat of fusion measurements were still taken after the specific heat measurements.

3.4.1.3 ASTM 1269E Comparison with MDSC for Specific Heat

The ASTM 1269E and MDSC methods determine the same thermophysical property, specific heat. Both methods compare a sample to an established standard to determine the sample's specific heat. However, one of the key differences between the two methods is duration of the test. In the ASTM 1269E test, the sample is only at any given temperature for a relatively short span of time, due to the high ramp rate required by the method. In comparison, the MDSC method uses a very slow ramp rate. Therefore any thermophysical changes that occur over time at elevated temperatures are far more likely to appear with the MDSC method. A significant question concerning the composite nanomaterial is whether the nanoparticles would precipitate

out of solution or agglomerate during testing, as both occurrences would negate any positive benefit the nanoparticles gave to the material. This event is unlikely to occur fast enough to be captured by the ASTM 1269E method, but it may impact the results of the MDSC method. Therefore, both methods were used to determine the specific heat.

3.4.1.4 Heat of Fusion Measurement

The heat of fusion, according to ASTM 1269E, is the definite integral of the heat flow with the limits of integration being the onset and offset temperature of the melting sample while the temperature ramp rate is extremely low (2° C per minute). The extremely low ramp rate is required to minimize the impact of the specific heat term of the total instantaneous energy absorption equation, shown as Equation 8.

$$Q = m(C_p\Delta T + H_f) \qquad (8)$$

In Equation 8, Q is the heat flow into the sample, C_p is the specific heat of the sample, ΔT is the change in temperature of the sample, m is the mass of the sample, and H_f is the heat of fusion of the sample. As can be seen from Equation 8, the smaller the ΔT, the smaller the effect on Q that C_p has. A low ramp rate reduces ΔT. Therefore, the best way to find the heat of fusion is to ramp through the melting temperature range as slowly as possible so that the energy absorbed (Q) will be almost entirely due to the heat of fusion.

Table 7: Total minimum required experiment list.
The time required to perform each test varies with the temperature range required and the testing method, as the ASTM and MDSC tests require different amounts of time for the same temperature range.

Material	**Number of Tests**	**Hours Per Test**
Plain Nitrate	6	6 to 9
Nitrate + Silica	6	6 to 9
Nitrate + Alumina	6	6 to 9

The total required test list is shown in Table 7. Three sample runs of each type were used, requiring months of testing. Three repeats were chosen to reduce time required for testing and to reduce cost, while still allowing for sufficient data integrity. All materials of the same type were from the same material creation batch, in order to ensure consistency between the samples. A minimum of 6 runs were required for each material to allow for three repeat measurements of each tested method and property - that is, three ASTM measurements and three MDSC measurements for each material.

3.4.1.5 Thermal Conductivity

The basic theory to test the thermal diffusivity and the thermal conductivity is as follows.

$$\alpha = \frac{1.38L^2}{\pi^2 t_{1/2}} \qquad (9)$$

where α is the thermal diffusivity, $t_{1/2}$ is the time required for the rear face of the sample to reach half of the maximum temperature rise, as shown in Fig. 15 [38].

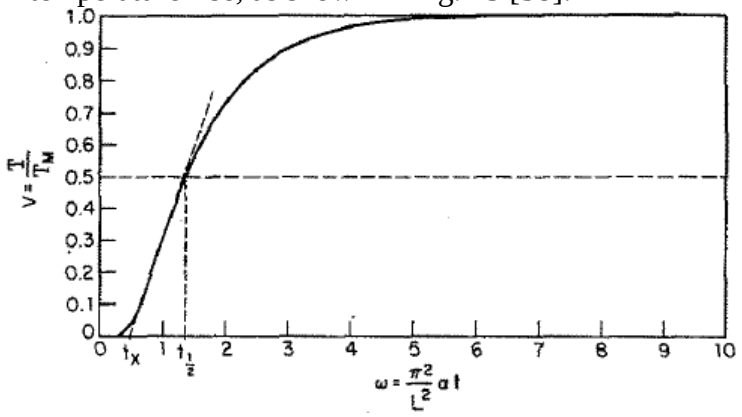

Figure 15: Dimensionless plot of rear face temperature

Then the thermal conductivity is found from the Eq. (10):

$$k = \alpha \cdot C_p \cdot \rho \qquad (10)$$

where C_p is the specific heat, ρ is the density of the sample.

In this study, thermal diffusivity and thermal conductivity measurements were performed using laser flash analysis (LFA) (LFA 447 NanoFlash, NETZSCH Co., Germany), shown in Fig. 16. The front side of the sample was heated by a short light pulse produced by the flash lamp. The resulting temperature rise on the rear surface is measured using an infrared detector (IR Detector). By analysis of the resulting temperature versus-time curve, the thermal diffusivity of the sample can be determined. Then its thermal conductivity (k) can be determined if its specific heat (C_p) and density (ρ) are known.

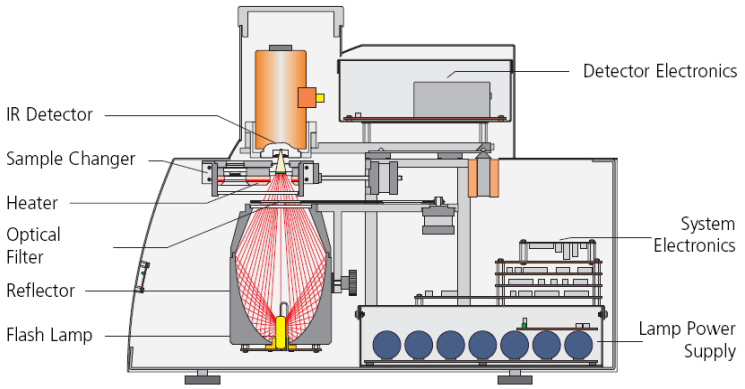

Figure 16: Schematic of the Laser Flash Analysis Experiment System

3.4.2 Stability Determination

As stated in the Introduction, one of the objectives of this project was to determine if the nanoparticle composite material and its thermophysical properties are thermally stable. While there is an ASTM test to determine the thermal stability of a sample using DSC (ASTM E537-07), the type of thermal stability being determined by that testing method is different from the

type of thermal stability desired in these tests. ASTM E537-07 looks at chemical reactions due to temperature and environment, and uses the heat flow to determine if a reaction takes place. For the purposes of this investigation, thermal stability refers to the consistency of the specific heat over the test duration, rather than the thermally triggered reactivity of the sample. There is no established testing method for this sort of observation. Therefore, the quantifiable metrics will be established here.

As described in the ASTM and MDSC method sections (3.4.1.1 and 3.4.1.2), the temperature profiles used in determining the specific heat consist of multiple repeats of the same ramp rate and temperature range. The temperature profile takes a considerable amount of time to completely execute due to the fixed temperature ramp rates and the time needed to cool the instrument between measurement cycles. While this length of time is a far less than that of a dedicated thermal stability test designed to emulate the operational thermal profile of a thermal energy storage system, it is still useful as a possible means to determine if the nanoparticles are falling out of solution. If they are, the specific heat of the sample should decrease over time as the nanoparticles coat the lower surface of the sample pan, reducing the concentration of nanoparticles suspended in the sample.

Quantifying the decrease in the specific heat over time is accomplished by comparing the measured specific heat from multiple cycles at a fixed temperature. The progressive change over time will be shown as a percentage change of the specific heat from cycle to cycle for a fixed temperature. Therefore, for the temperature profiles previously discussed, there will be two measurements of thermal stability for each sample: a percentage change in the specific heat between the first and second measurement cycle, and a percentage change in the specific heat between the second and third measurement cycle. A consistent decrease will manifest as two negative percentage changes greater than the measurement uncertainty of the DSC. Other possible outcomes represent unclear results, as many other factors could cause an apparent increase in specific heat between cycles, such as a material or sample pan geometry change.

3.4.3 Thermal cycling test

Separate thermal cycling tests were conducted for nitrate eutectic salts with nanoparticles and carbonate eutectic salts with nanoparticles. In both cases, the nanomaterial was subjected to thermal cycling in a stainless steel sample container. The nanomaterial was held in 316 SS grade stainless steel cylinders of 3/8” diameter and 3” height. The cylinder's dimensions should enable us to emulate actual plant operation in a laboratory setup. (In this case, the dimensions of the cylinder are also restricted because the nanomaterial is expensive and requires lengthy preparation. Therefore an optimum test sample size was determined arbitrarily for this test. A diagram of the sample holder is shown in Figure 17, and a picture of the sample holder in its oven support rack is shown in Figure 18.

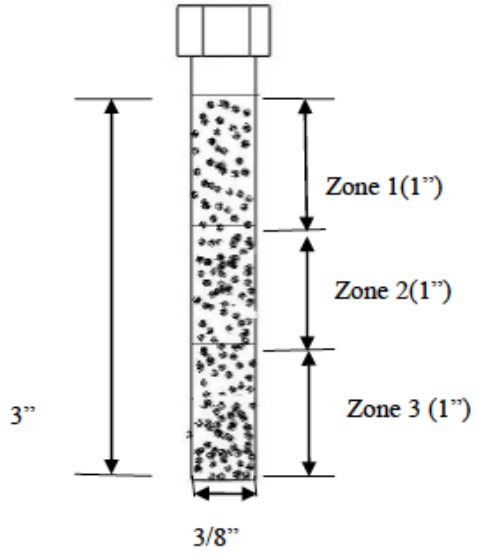

Figure 17: Schematic representation of a sample holder showing the nanomaterial and the different zones for study

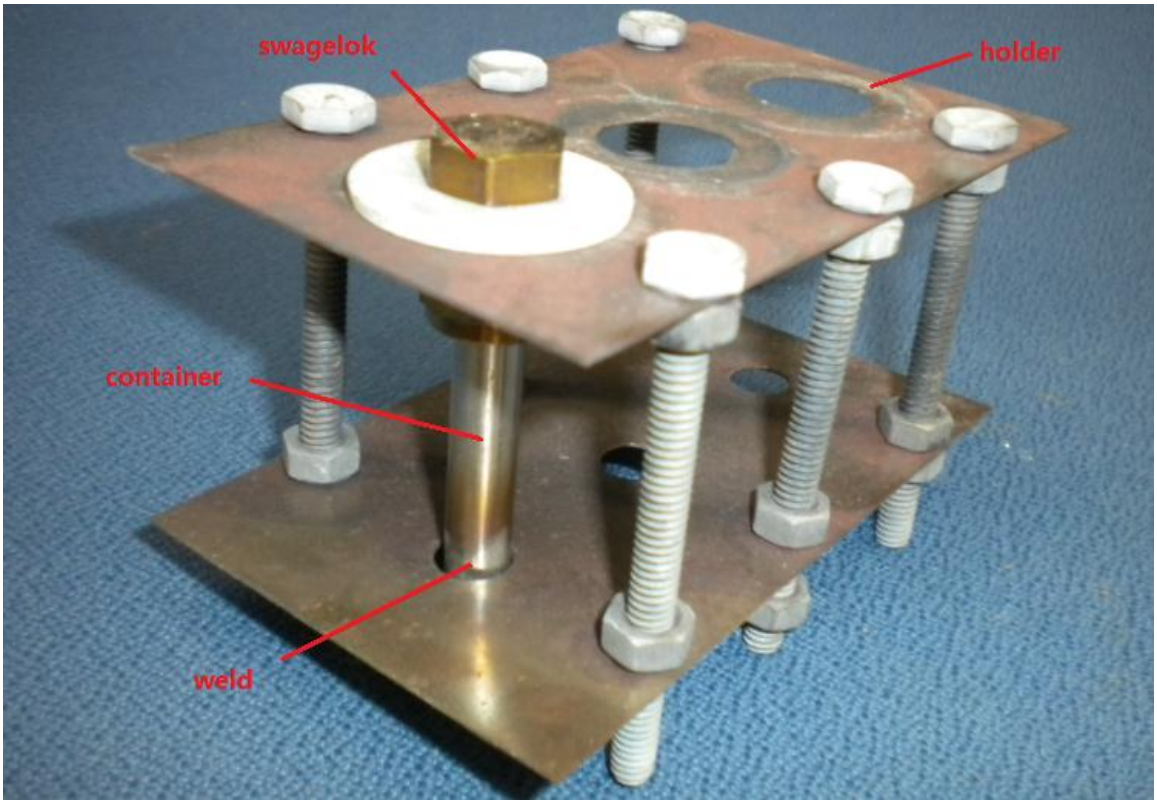

Figure 18: Picture of a sample holder with its oven test support rack

Each cylinder was sealed with Swagelok compression fittings on one end and welded on the other end. There were 5 batches of nitrate salt and 4 batches of carbonate salt that were subjected to thermal cycling. Each batch contained 3 sample cylinders, underwent a different number of

thermal cycles. and was therefore kept in the furnace for a different length of time. The thermal cycling was carried out in a Linderburg Blue 3 zone tube furnace with a UP 150 programmable temperature controller. The controller was programmed with the cycle following the temperature profiles described in Figure 19 for the nitrate salt and Figure 20 for the carbonate salt.

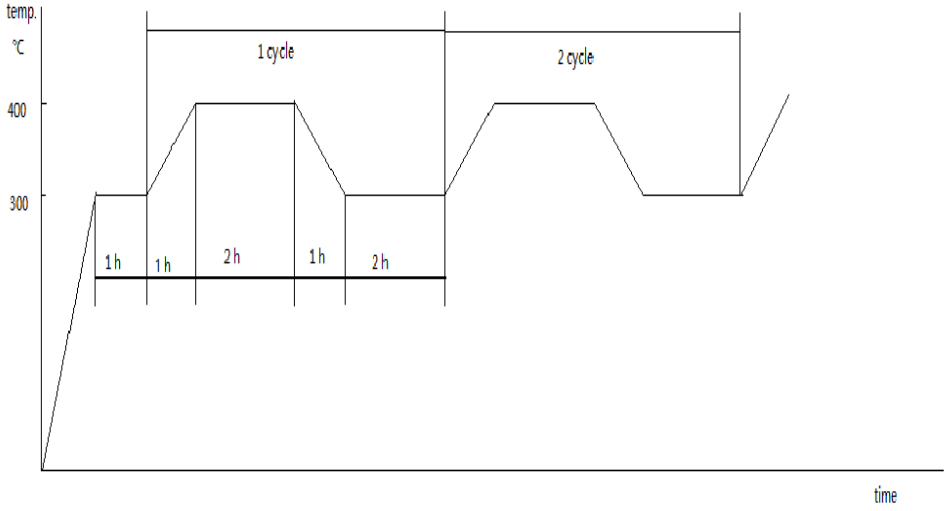

Figure 19: Diagram of thermal cycle used for stability testing of alumina + nitrate eutectic

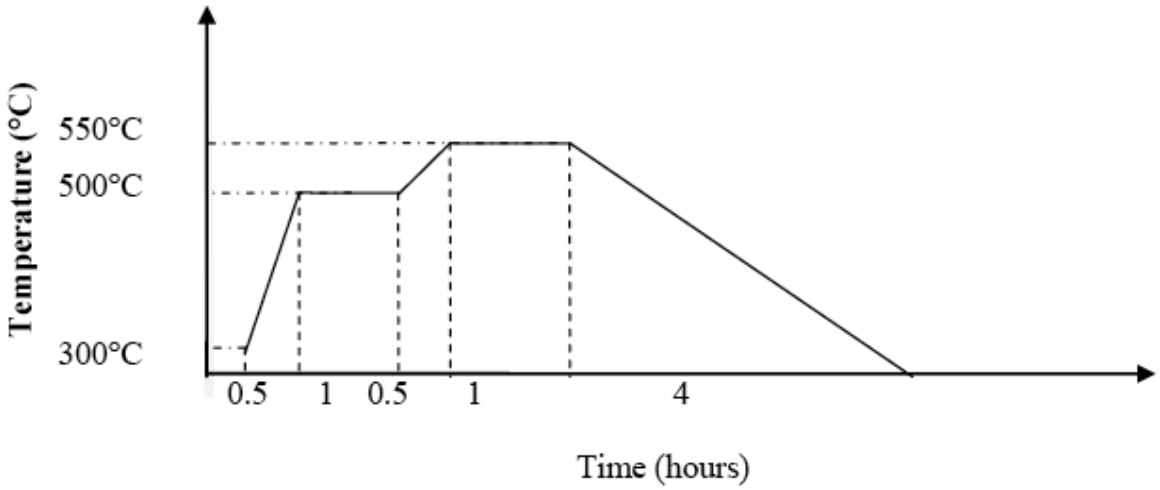

Figure 20: Diagram of thermal cycle used for stability testing of alumina + carbonate eutectic

3.4.3.1 Extraction of materials for analysis

The sample cylinders were taken out of the furnace after completion of thermal cycling. Study of the gradient in the concentration of nanoparticles along the height of the sample container requires analyzing material from multiple sections of the specimen. In accordance with the

preliminary nature of this study, thermophysical properties were characterized by taking material from 3 zones – top (zone 1), middle (zone 2), and bottom (zone 3). The sample cylinder is sectioned with a tube cutter to avoid any contamination of the material. The nitrate material was mechanically extracted from its sample holder section by crushing the tube sidewall. For the carbonate material, the section is allowed to soak in a dish of water. This makes the material soft so that it can be removed with minimal effort. The material removed from the sections is stored in glass vials. The material that was tested in the DSC is stored in a glove box with desiccants to keep the material moisture-free.

3.4.3.2 Measurement of Specific Heat with a Modulated Differential Scanning Calorimeter

The Modulated Differential Scanning Calorimeter (MDSC) as described above (Section 3.4.1.2) is used to measure the specific heat of the material. The properties of the material are measured before and after the material is subjected to thermal cycling.

3.4.3.3 Measurement of Particle Concentration - Neutron Activation Analysis (NAA)

The gross settling of nanoparticles in the base material due to gravitational effects is measured by the concentration gradient along the height of the test cylinder. The concentration of the nanoparticles is measured using neutron activation analysis (NAA). The method is suitable for the qualitative and quantitative analysis of minor and trace elements. The sample to be analyzed is bombarded with neutrons to create radioactive isotopes, which decay and emit a measureable radiation--in this case gamma rays. The gamma ray emitted is characteristic of a specific element. The signal can be analyzed to determine the concentration of a particular element--in this case, aluminum. The percentage mass concentration of the nanoparticles can be derived from the elemental percentage concentration.

$Al^{27} + n^{1} \longrightarrow Al^{28*}$
$Al^{28*} \quad Al^{28} + \gamma$ (radiation)
Al^{28*} - Radioactive isotope of aluminum

The sample from each zone of the test cylinder is analyzed using NAA, and the concentration of the nanoparticles in the top, middle and bottom zones is measured.

The neutron activation method was employed for quantitative analysis of aluminum in the sample, from which the percentage of alumina has been calculated. To check for neutron flux alteration due to the presence of lithium, standards were made on lithium carbonate substrate. 500 micro liters of 1000 µg/ml solution of aluminum oxide standards were deposited onto lithium. Three such standards were tested and gave results of 1056, 1045, and 1049 ppm (µg/g) as against the expected results of 1000 ppm. There was a 5% positive bias, and it was surmised that the data did not indicate that any effect due to lithium was detected. The samples for the tests were made completely moisture-free and then deposited into 1 ml vials. The results of the tests give us the percentage of aluminum in the sample expressed as µg/g of aluminum. From this the percentage by mass of alumina is calculated using the formula:

$$\text{Mass percentage of alumina} = \frac{Mass\ of\ aluminum * 101.96)}{53.96} * 10^{-4} \quad [9]$$

All the tests were carried out by the Center for Chemical Characterization and Analysis, Texas A&M University.

3.4.4 Corrosion Testing

The experiment was designed to mimic the wall conditions of the steel containers used as storage tanks in a CSPP exposed to molten carbonate eutectics. This was achieved using a coupon made of SS304, the material used for constructing a storage tank of a CSPP. This coupon approximately 5x20x.6mm and .5gm in weight represented the wall of such a storage tank as shown in Figure 21.

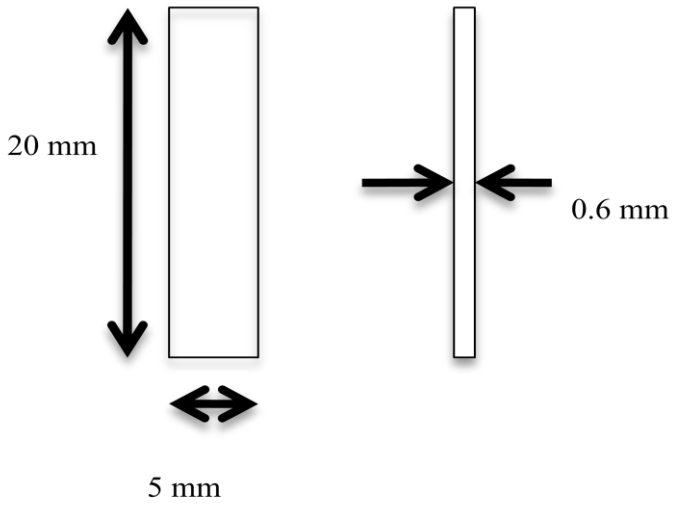

Figure 21: A Schematic Diagram of a Steel Coupon.

This experiment was a static immersion test, implying that the corroding environment (molten eutectic) would be static and in contact with the steel coupon. The temperature for testing was set at a constant 520° C, a temperature comparable to those encountered in a CSPP.

The following experimental setup was used to best mimic the walls of a storage tank of a CSPP. A “sample bomb” design was adopted that was a steel tube 3/8” in diameter and 3” in length, filled with a steel coupon surrounded by TES material, and sealed at both ends using compression fittings. This arrangement is shown schematically in Figure 22.

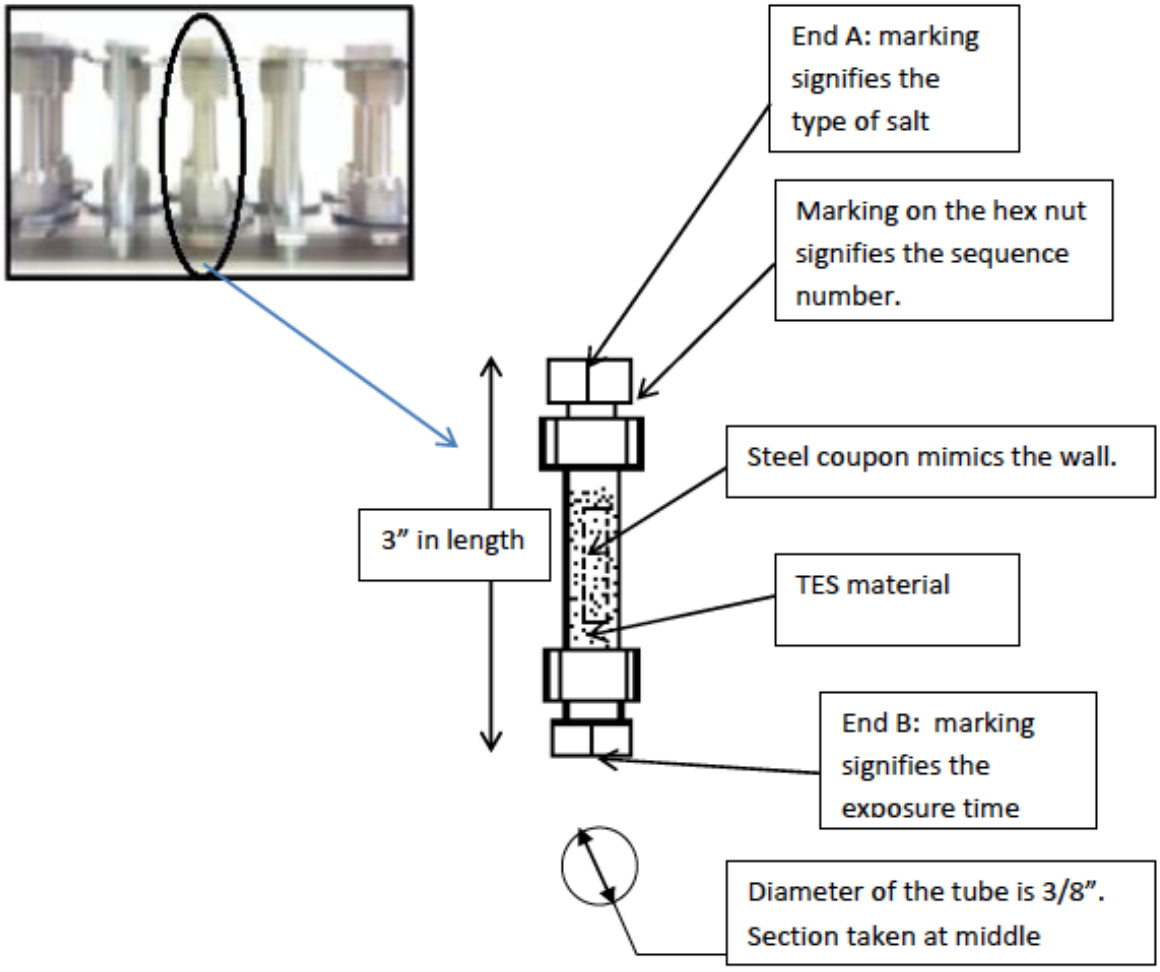

Figure 22: A Schematic of a Sample Bomb, with Reference to an Actual Sample Bomb Photograph.

Each cell in the test matrix given in Table 8 gives the number of samples per exposure time.

Table 8: Test Matrix

Test Time(wks)	Carbonate	Carbonate+Silica	Blank	Total/Time
2	3	3	3	9
4	3	3	3	9
6	3	3	3	9
Total Samples		27		

The corrosion time must be significant to have measurable mass loss - on the order of hundreds of hours as per Thomas et al [18] and Tzvetkoff et al [39]. A timeframe of 300 -1000 hours (2 to 6 weeks) was chosen.

A larger surface area yields better results, as a larger surface area will provide a larger mass loss

and a larger mass loss will reduce uncertainty in the results, but the surface area is constrained by the amount of salt available, the furnace size, and cost. Given these constraints the best option was to adopt a steel coupon design with dimensions of approximately 20x5x0.6 mm, weighing about 0.5 g. Both [18, 20] suggest a steel coupon design. In addition, the size chosen matches the size used in testing by Bradshaw et al [19]. The quantity of salt was determined by the need to completely cover the steel coupon in molten salt.

The length of the steel tubing, which was used as a housing to contain the steel coupon and the salt, was determined by the size of the oven, which in turn set the maximum size of the coupon and the amount of salt. The length of the steel tubing must also account for volume expansion, which is approximately 18% for the carbonate salts over the temperature range measured.

The temperature of the test was set at 520° C, a temperature comparable to those used in CSP operations (500° - 600° C) and above the melting point of the carbonate eutectic. The variation in temperature inside the oven was ±5° C, as measured using a thermocouple at regular intervals.

The coupons were cleaned after the test according to the procedure detailed in Bradshaw et al [19] and Watanabe et al [20]. According to those papers, the gravimetric mass loss was obtained by using concentrated HCl to descale the corroded coupons. A washing time in HCl of 1 minute was determined to be sufficient from previous tests.

The concentration of silica nanoparticles was kept at 1% by weight throughout the experiment.

The loaded sample bomb was kept vertical to ensure that the steel coupon was in constant contact with the molten carbonate salt. A frame was built to ensure that the sample bombs were always upright during the test.

One uncertainty in this experiment was the amount of physical cleaning. After descaling, the steel coupons were rinsed with distilled water and immediately wiped dry. The amount of physical cleaning was variable. The procedure was standardized by wiping the steel coupon just once in one direction, to minimize any biasing of the results due to physical cleaning.

The cleaned coupons were then weighed to determine their mass after exposure using a microgram balance.

3.5 System Modeling

3.5.1 Sensitivity Modeling

The National Renewable Energy Laboratory has an Excel based CSPP modeling package known as Excelergy, which was used to estimate total TES system costs. The model was modified to use the TES material's specific heat capacity to determine the mass of TES material needed for a given system. The original version from NREL used the enthalpy of the TES material to perform this calculation. The methodology of the modified model is presented below:

1. Determine baseline thermal demand to operate the turbine at 100% capacity

$$\text{ThermalInputDemand}[MW_t] = \frac{\text{TurbineOutput}[MW_e]}{\text{TurbineEfficency}} \quad (12)$$

2. Determine the amount of energy to be stored by the TES

$$\text{StoredEnergy}[MWh_t] = \text{ThermalInputDemand}[MW_t] \times \text{TESTime}[hr] \quad (13)$$

3. Convert energy storage units from MWh_t to kJ

$$\text{StoredEnergy}[kJ] = \text{StoredEnergy}[MWh_t] \times \frac{1000kJ}{MW \cdot s/MJ} \times \frac{3600s}{1hour} \quad (14)$$

4. Determine the mass of TES material needed for the TES system

$$\text{MassTESMaterial}[kg] = \frac{\text{StoredEnergy}[kJ]}{\text{Average}C_p[\frac{kJ}{kg \cdot C}] \times \Delta T_{TES}[C]} \quad (15)$$

5. Determine the tank volume

$$\text{TankVolume}[m^3] = \frac{\text{MassTESMaterial}[kg]}{\text{DensityTESMaterial}[\frac{kg}{m^3}]} \quad (16)$$

6. Use the Exelergy model to determine tank costs

$$\overset{\text{yields}}{\rightarrow} \text{TankCosts}[\$] \quad (17)$$

7. Determine the material costs

$$\text{MaterialCosts}[\$] = \text{MassTESMaterial}[kg] \times \text{UnitCosts}[\frac{\$}{kg}] \quad (18)$$

8. Determine cost of the TES system with 10% margin

$$\text{TotalTESCost}[\$] = (\text{TankCosts}[\$] + \text{MaterialCosts}[\$]) \times 1.1 \quad (19)$$

9. Determine \$/kWh_t cost of the TES system

$$\text{TESCost}[\frac{\$}{kWh_t}] = \frac{\text{TotalTEScost}[\$]}{\text{StoredEnergy}[MWh_t]} \times \frac{1MWh_t}{1000kWh_t} \quad (20)$$

10. Determine \$/kWh$_e$ cost of the TES system

$$\text{TESCost}[\frac{\$}{kWh_e}] = \frac{\text{TotalTEScost}[\$]}{\text{TurbineOutput}[MW_e] \times \text{TESTime}[hr]} \times \frac{1MWh_e}{1000kWh_e} \quad (21)$$

3.5.2 System Performance Model

The System Performance Model aims to model the real-time daily operation of a CSPP.

3.5.2.1 Performance Model

The model algorithms consist of three parts: pre-calculation, routine and result output as shown in Figure 27.

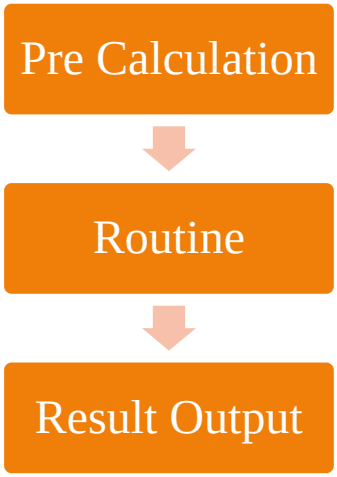

Figure 27: General Procedure for Performance Model

3.5.2.1.1 Pre Calculation

One time and check procedures are located in the pre-calculation section. This section contains routines that:

1) Calculate standard flow rate, solar concentration factor, and field area according to the reference situation. It program supplies an interface for calculation regardless of which solar field area input method or solar concentration method is used. The inputs for this part are the solar concentration, the rated input capacity of the power block, the direct normal irradiation at the site, and the system configuration. Iteration is used because the heat loss calculation depends on temperature.
2) If needed, calculate the two tanks/thermocline system tank specifications when the user selects the default mode. The program supplies a basic method to design the thermal storage system. There are two advantages: first, the thermal storage system is always covered with thick insulation material and it only loses a little heat to environment, so value does not affect the simulation result much. Second, it saves a lot of time when

comparing different thermal storage systems since it is not necessary to configure the details of the thermal storage system.

3) Calculates thermal storage system's maximum power discharge capacity and mass capacity, which tells the control unit how full the tank is and controls charging and discharging tanks.
4) Calculates converters minimum and maximum output ability and the start-up energy requirement that is used in the control part of the routine calculation. It is used to control the mass and energy flows.

3.5.2.1.2 Calculation Routine

The calculation routine is based on physical models because empirical models lose accuracy when the input outranges the regression area. The routine uses a variable time step simulation method during the calculation, shown in Figure 28. Each time step includes all the calculations of the procedure. The calculation order is explained below.

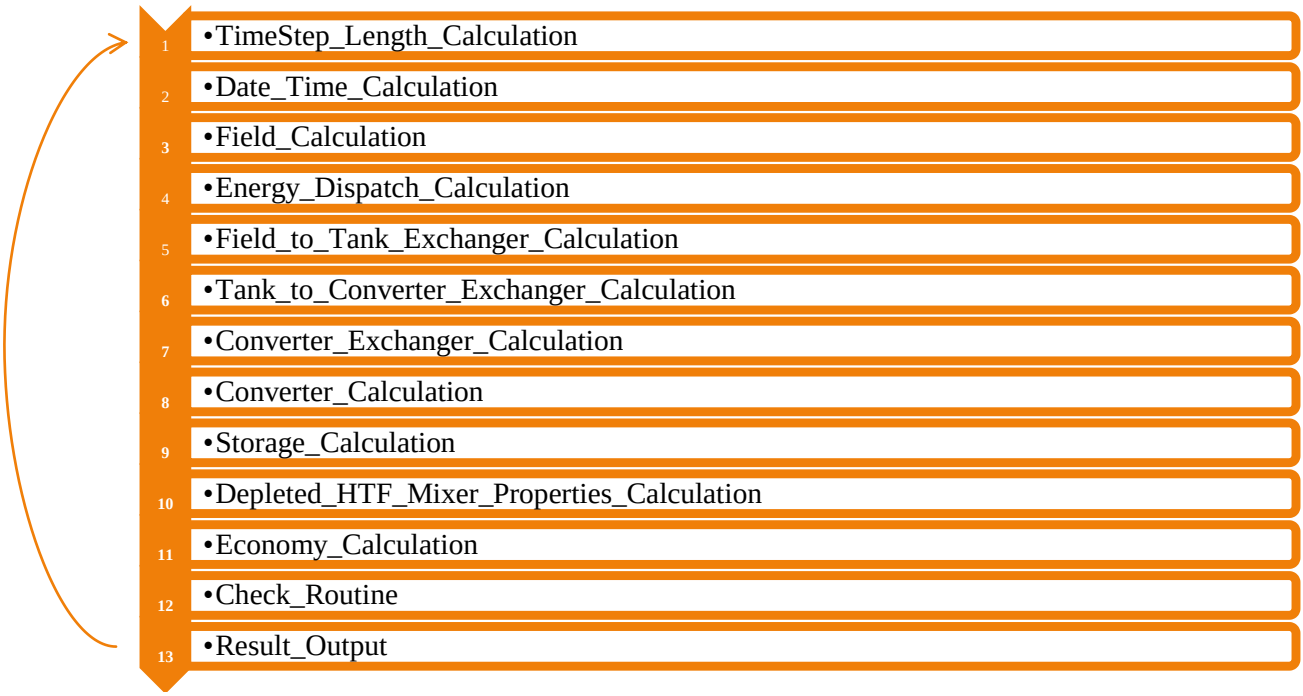

Figure 28: Inside of Calculation Routine

The time step calculation length is used to set the time step for this round. The default value is set to one hour. This value can be changed during the routine. In a transient situation, the time step can be set shorter to maintain high accuracy and it can be set longer in stable states to accelerate the calculation speed. Therefore, accuracy and speed can be balanced.

The date-and-time calculation is used to obtain end point year, month, day, hour, minute, second and weekday/weekend. The input is the previous end point date, time and time step. The current date and time are used in the direct normal irradiation intensity calculation, revenue calculation and result output.

The field calculation includes several subsystems, they are: Corrected direct normal irradiation calculation; Heat transfer fluid (HTF) heat gain calculation; Heat loss calculation; Net thermal output calculation; HTF flow rate/temperature calculation; Fossil fuel backup calculation; and Energy consumption calculation.

Direct normal irradiation is important for the simulation because it serves as the energy input for the whole CSPP system. Currently only hourly DNI data is available, which is not sufficiently accurate when the time step is variable, not to mention the error in sunset and sunrise time. So, in this routine, interpolated DNI are calculated for every time step by considering original DNI data, date and time (to calculate sunrise and sunset time), field location and deploy/stow angle. Figure 29 is one sample for the process. The assumed sunrise time is 7:20 AM and the sunset time is 6:20 PM and time step is 1 hour.

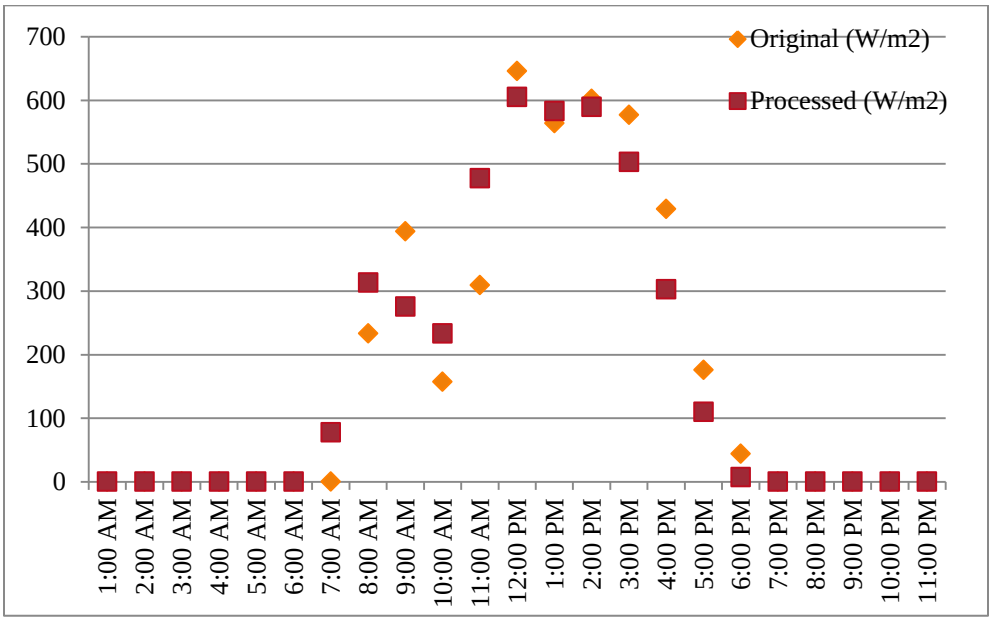

Figure 29: Sample Output from the DNI Calculation routine

The HTF heat gain calculation calculates the amount of thermal energy that arrives at the surface of the heat collection pipe. Various factors that affect the reflection and heat transfer processes are considered. Those factors include and are not limited to field error, reflecting mirror error, tracking angle cosine effect, optical efficiency, and end loss effect.

The heat loss calculation calculates the heat loss from the HTF in the collection and transfer pipes. Heat collection pipes contribute to most of the heat loss since they are the longest type of pipe and are not insulated. The transfer pipe is the second longest pipe in the field. Only these two kinds of pipes are considered.

A one-dimension model is used for the field model. During the calculation, the HTF in the field pipes is assumed to be a uniform temperature, which is the average value of inlet and outlet temperature of the field system. In the future, the model could be expanded to include individual heat collecting elements (HCE) with its own temperature value.

Several possible conditions of the heat collection pipe have been considered, some less than ideal – namely a normal working pipe, a pipe with the glass envelope broken, a pipe with a loss of vacuum in the pipe and a pipe with hydrogen in the vacuum pipe. Vacuum is an important consideration because it supplies the greatest heat resistance and it greatly affects the performance of the thermal energy collection element. Figure 30 shows heat transfer to the environment from the pipe.

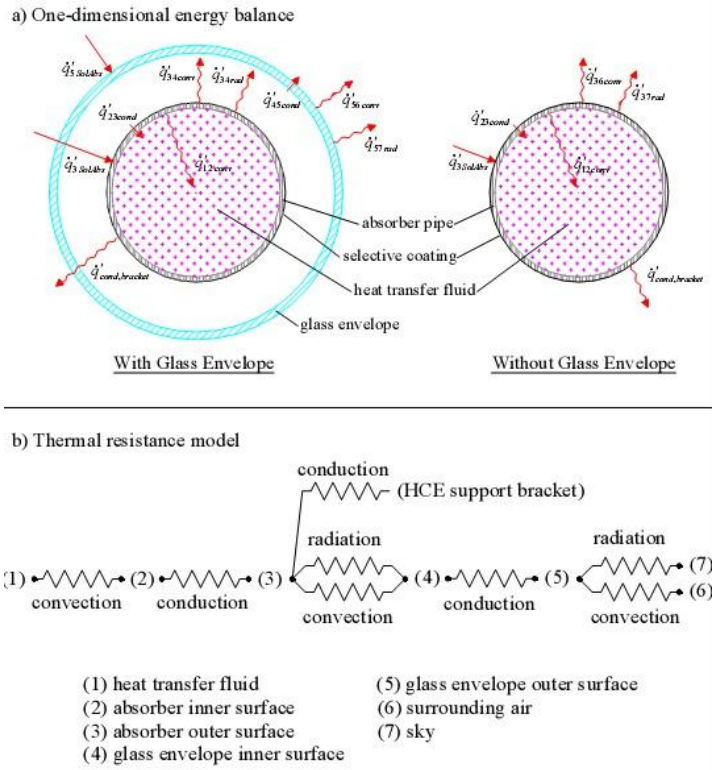

Figure 30: Energy balance and heat resistance for HCE

A test was conducted to verify the calculation accuracy of the HCE model. The performance of the PTR70 Parabolic Trough Receiver was simulated and compared with experimental results [40]. Table 9 and Figure 31 show the results of this comparison.

The uncertainty of the temperature sensor (thermocouple) is 1.1 $^{\circ}C$ or 0.4% T, whichever is greater, and the uncertainty for measuring heat loss is 10 W/m^2. According to the comparison, we can assume the simulation is accurate enough to reflect the real situation adequately.

Table 9: Surface temperature and heat loss compare between simulation and experiment result

Step No.	Ambient Temperature ° C	Absorber temperature ° C (measured)	HTF temperature ° C (Simulation)	Glass temperature ° C (measured)	Glass temperature ° C (Simulation)	Heat Loss W/m (Measured)	Heat Loss W/m (Simulation)
1	23	100	100	26	26	15	10.1
2	23	153	153	30	29	23	21.5
3	23	213	213	35	34	43	42.5
4	23	246	246	38	37.8	59	59.4
5	24	317	317	50	49.5	113	113.9
6	24	346	346	55	55.2	141	145.7
7	24	390	390	65	65.6	204	208
8	24	418	418	73	73.4	257	258.4
9	24	453	453	82	84.6	333	335.5
10	24	458	458	84	86.3	348	348
11	24	506	506	99	104.8	495	488.9

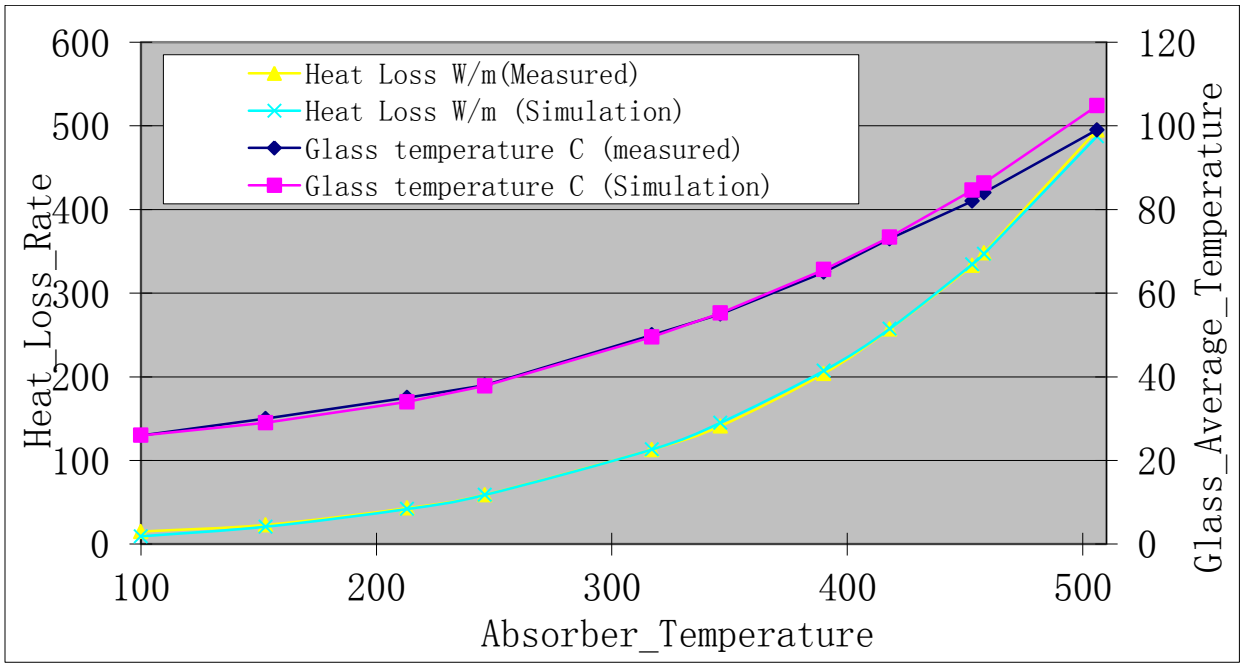

Figure 31: Surface temperature and heat loss compare between simulation and experiment result

The net thermal output, and the HTF flow rate/temperature calculations give the solar field's outlet HTF parameters, which includes HTF flow rate/temperature (in the configuration, only one of them can be set fixed) and available output thermal energy. The thermal energy is calculated according to the baseline temperature. Usually, the HTF inlet temperature is set as the default baseline temperature.

If the power plant is a hybrid type, the plant has a secondary heat source (to heat HTF)in order to overcome the solar variability problem (affected by weather, solar intensity and night time). This would allow the solar plant to be a reliable base load power plant for the grid. If the fossil fuel backup calculation is enabled by the configuration file, it calculates fossil fuel consumption and its thermal energy output.

The energy consumption calculation considers the electricity consumption in the field by the electric motors used to adjust the mirror position, the pump used to deliver the HTF, and the heater used to maintain the HTF temperature.

The energy dispatch calculation (step 4 of the calculation routine in Fig. 28) sets the working status of the thermal storage system and the power generation unit. It calculates the amount of thermal energy each system will receive or release in this time step. (All thermal energy is calculated from the same baseline.) The thermal energy flow is converted to a mass flow of HTF for delivering energy to the thermal storage system or power block.

Currently, the energy dispatch strategy is set to maintain maximum power block efficiency as well as keeping thermal dumping to a minimum. That means the power block always works at its rated power output (maximum efficiency). In addition, if the thermal storage system is full, the power block is set to convert as much thermal energy as possible to electricity (minimizing dumping).

The field-to-tank exchanger calculation, the tank-to-converter exchanger calculation, and the converter exchanger calculation (steps 5, 6, and 7 of the calculation routine in Fig. 28) are all heat exchangers, which are used to exchange heat among HTF, TES, and the working fluid (usually vapor and water) of the power block. Depending on the specification, some power plants may need three exchangers (two separate heat exchangers for the thermal storage system, one with the field and one with the power block) while some only need two heat exchangers (one heat exchanger for the thermal storage system), such as that shown in Figure 1. This model can work with either situation. In the two heat exchanger situation, we just need to set the same parameters for the field-to-tank exchanger calculation and the tank-to-converter exchanger calculation.

In the heat exchanger's sub-function, the mass and volume flow rate are calculated along with the delivered thermal energy and the heat loss in this component.

In the converter model, the electric generation rate and amount are obtained. A regression model is used in the converter model when the converter is working at steady state. Because the converter operates in a narrow range, the regression model is accurate enough for the simulation. The starting and stopping processes are considered separately to avoid errors from the regression model.

In the storage system calculation (step 9 of the calculation routine in Fig. 28), both two tank and thermocline systems are considered. The configuration file input chooses the one to be used in the simulation.

The storage model accomplishes several tasks:
Calculate heat loss during current time step from conduction, convection and radiation in three directions (bottom, top and sides). An iterative method is used since air and tank materials properties depend on temperature. This is similar to the pipe heat loss calculation.

Update tank(s) situation, including TES volume fraction, mass fraction and temperature and update available thermal energy of the storage system based on the heat loss calculation. The status of each tank (such as how full the tank is and the temperature of the TES in the tank) is obtained. Also, the available thermal energy is obtained. Those values are used for the next time step's heat loss calculation and energy dispatch calculation.

Calculate energy consumption in the storage system. The energy required for fluid pumping and the resistance heater is calculated. Since the flow rate is significant, the energy used to drive the pump cannot be ignored. If electrical resistance heating is adopted to maintain the tank temperature, that energy consumption is also accounted for in this part of the calculation.

The depleted HTF mixer properties calculation (step 10 of the calculation routine in Fig. 28) merges the HTF flows that come from the field-storage and field-converter exchangers to a single flow. The resulting temperature and the flow rate of the single flow are derived from mass and energy conservation laws.

In the real world, electricity is not a constant price, but changes in price according to supply and demand. High demand usually means a high sale price. In the economy calculation (step 11 of the calculation routine in Fig. 28), weekdays and weekends have different hourly prices. This includes both the sell price (the price at which the power plant sells electricity to the grid) and the buy price (the price at which the power plant buys electricity from the grid). Including these different prices may help give a more accurate and deeper understanding of the economics of a solar power plant.

The self-check routine (step 12 of the calculation routine in Fig. 28), assures the whole calculation worked.

3.5.2.1.3 Results Output

In the results output routine, (step 12 of the calculation routine in Fig. 28), each time step's results are saved to an Excel file and workspace. The Excel file contains one general result sheet and several detail sheets. Each component of the power plant has one sheet to display the detailed time step by time step results. The data in the workspace from the calculation routine in Fig. 28 forms part of the input parameters for the economic model.

3.5.2.2 Model Verification

In order to verify the reliability and accuracy of this model, the performance of the Andasol-1 solar thermal power plant is calculated with this model, and the result is compared with the Solar Advisor Model (SAM).

The Andasol-1 solar power station is Europe's first commercial parabolic trough solar thermal power plant. It located near Guadix in Andalusia, Spain. The site's coordinates are 37°13´N; 3°04´W. It went online in March 2009. Due to the high altitude and arid climate, it expects to have 2200 KWh/m^2 annual direct irradiation. The power plant has a gross electricity output of 50 megawatts (MW), producing around 180 gigawatt-hours (GWh) per year (21 MWyr per year). It has a two tank thermal storage system which can store around 7.8 hours' of energy for the converter system. The peak efficiency of the entire plant is about 28%, while its annual average efficiency is about 15%. Figure 32 and Figure 33 are the configuration and operation schematic for the plant during solar collection (Fig. 32) and stored energy operation (Fig. 33).

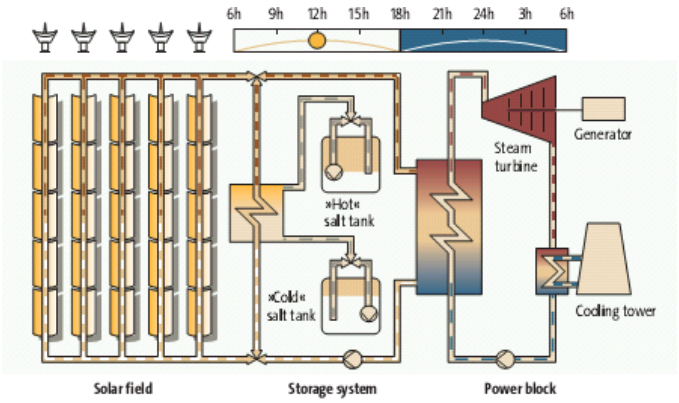

Figure 32: The thermal storage system is loaded during the day

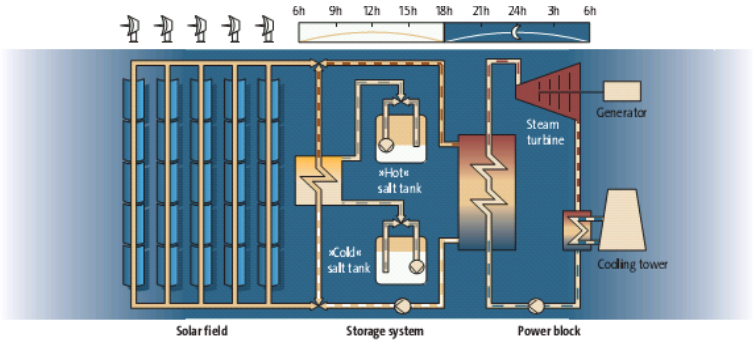

Figure 33: The power plant operates during the night with stored energy

The SAM model is a performance and economy model developed by the National Renewable Energy Laboratory (NREL). It widely used for predicting performance and economic estimation in grid-connected solar, small wind, and geothermal power systems. It is used in the renewable energy industry around the world, from project managers and engineers to technology developers and researchers.

SAM is based on an hourly simulation engine that works with performance, cost and finance models to calculate energy flow, electricity generation, and cash flows. Currently the SAM uses regression models to calculate energy-related results. SAM uses TRNSYS software to simulate the performance of photovoltaic, concentrating solar power (CSP), water heating, and other renewable energy systems using hourly resource data.

3.5.2.2.1 Environmental Conditions

During the simulation, the ambient temperature, direct normal radiation, and wind speed are loaded from the weather file (ESP_Granada.084190_SWEC.epw), which is downloaded from the internet [41]. This file contains measured hourly environmental data from 1989 that is used as input for the simulation.

The weather conditions are shown below: Figure 34 is the hourly ambient temperature; Figure 35 and Figure 36 are the hourly and monthly direct normal irradiation (DNI). Wind speed is a constant 6.7 m/s according to the file.

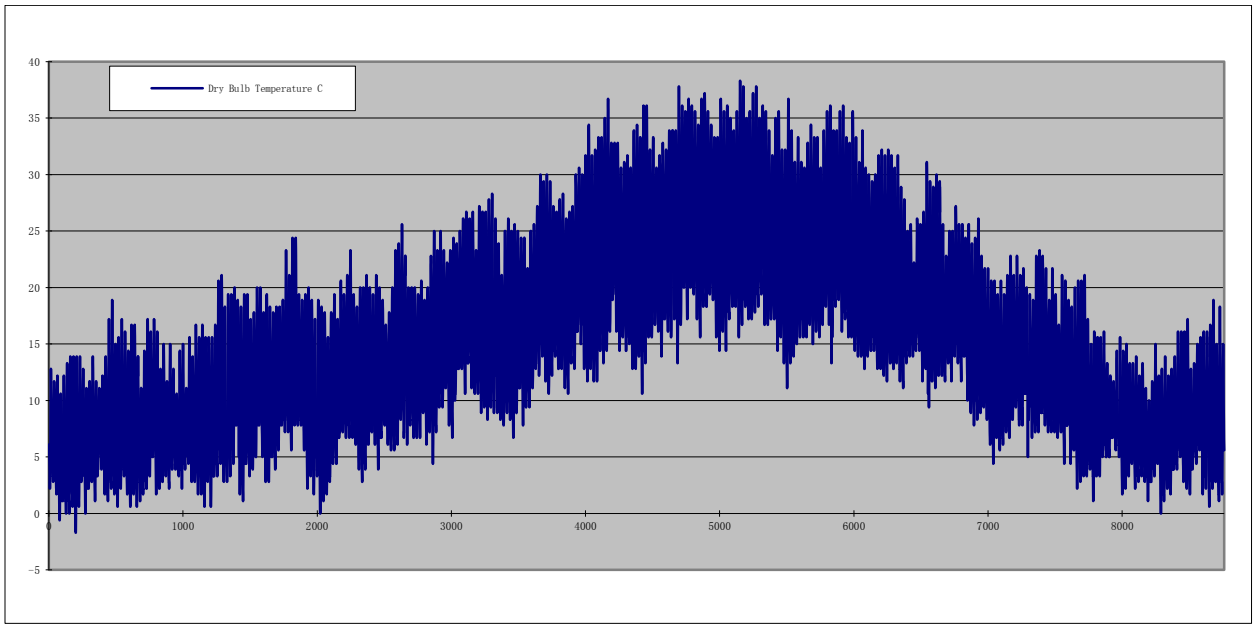

Figure 34: Hourly Ambient Temperature

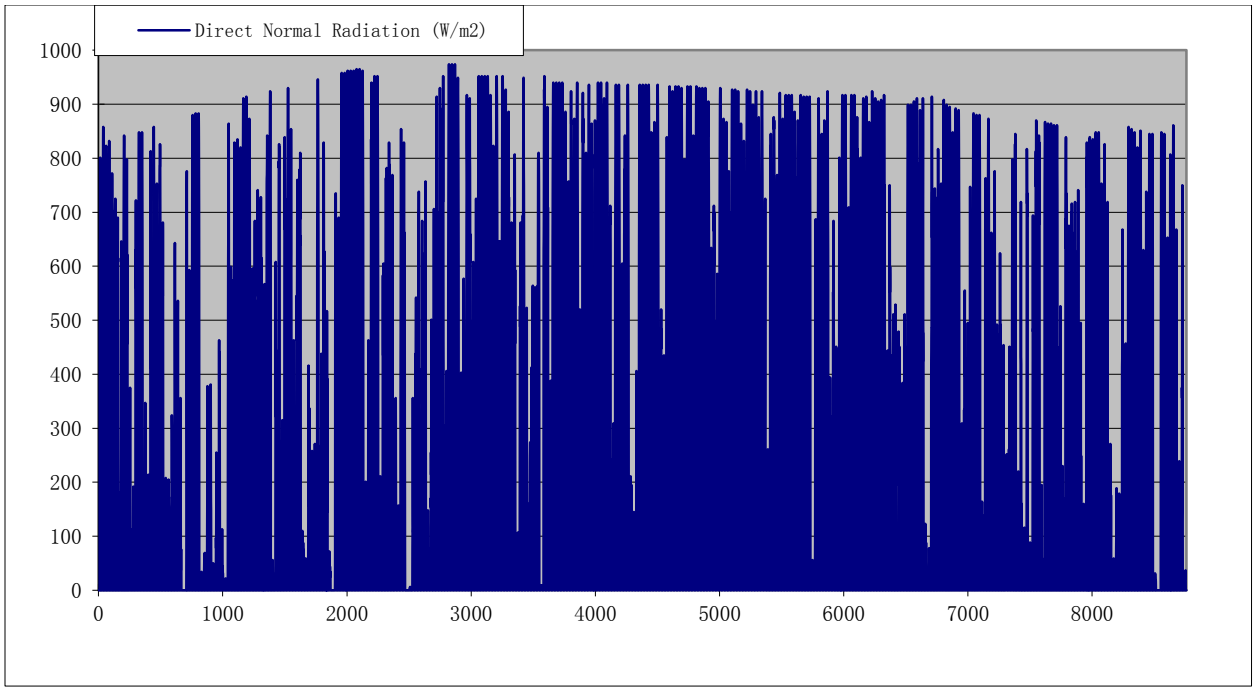

Figure 35: Hourly Direct Normal Irradiation

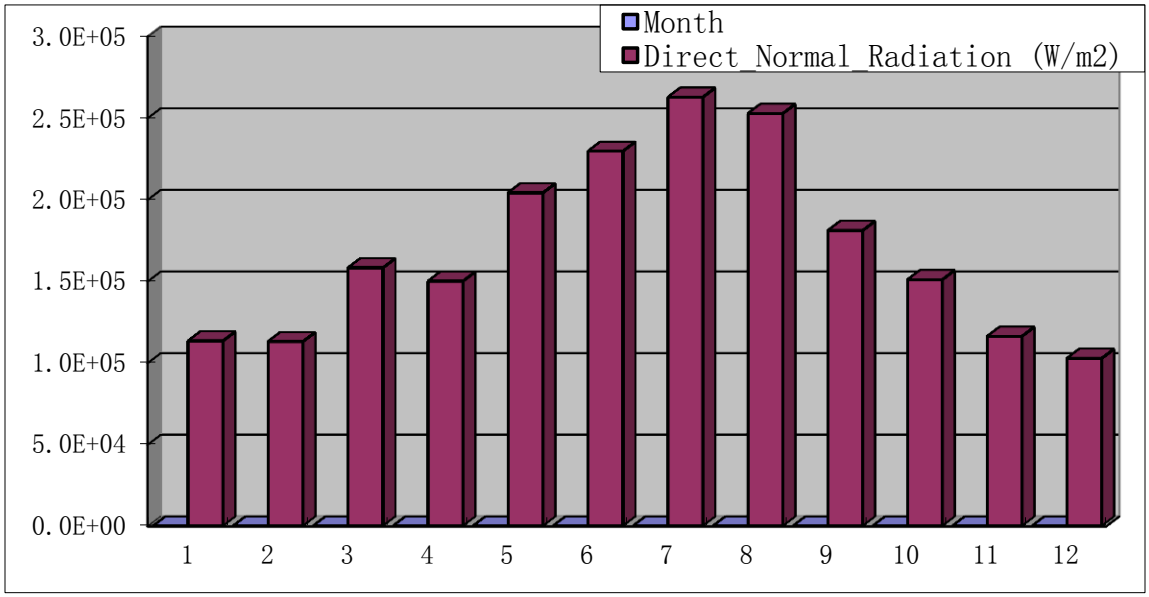

Figure 36: Monthly Direct Normal Irradiation

3.5.2.2.2 Comparison of Results

The annual absorbed energy calculated from Matlab/Simulink is 1.25 MWh/m^2 while the SAM's result is 1.29 MWh/m^2, as shown in Figure 37. The difference is 0.04 MWh/m^2 or 3%. The difference is mainly due to different treatment of hour-by-hour direct normal irradiation, as shown in Figure 38.

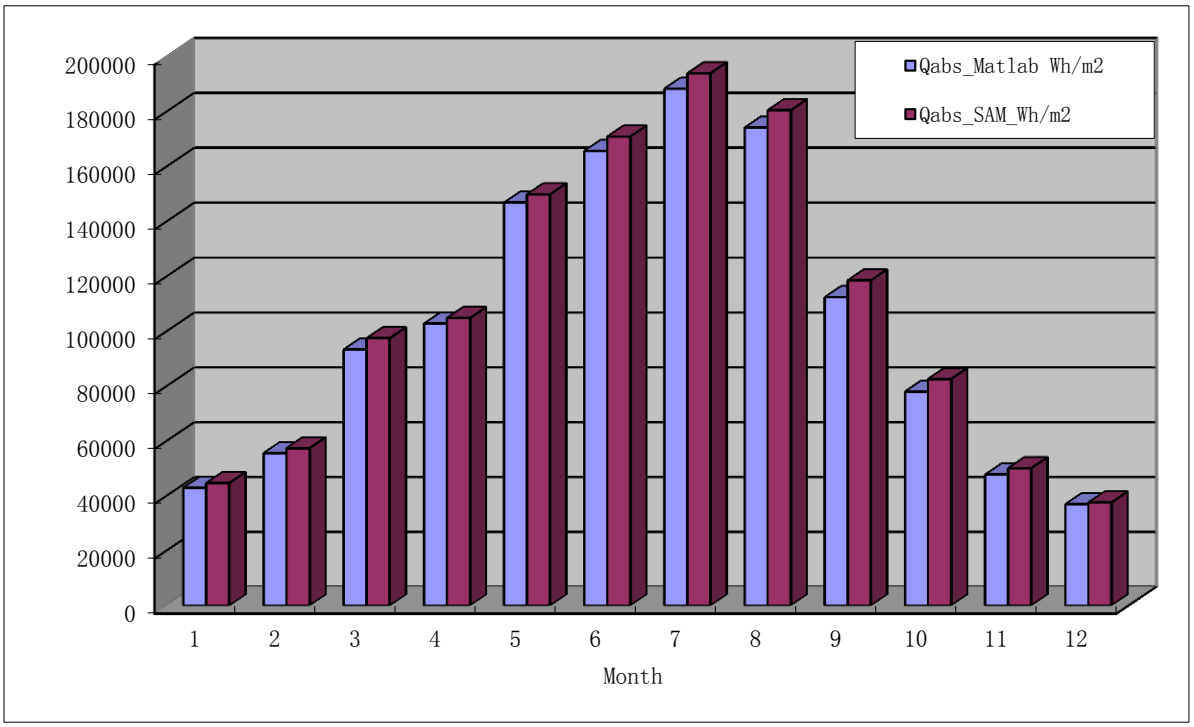

Figure 37: Monthly Absorbed Thermal Energy

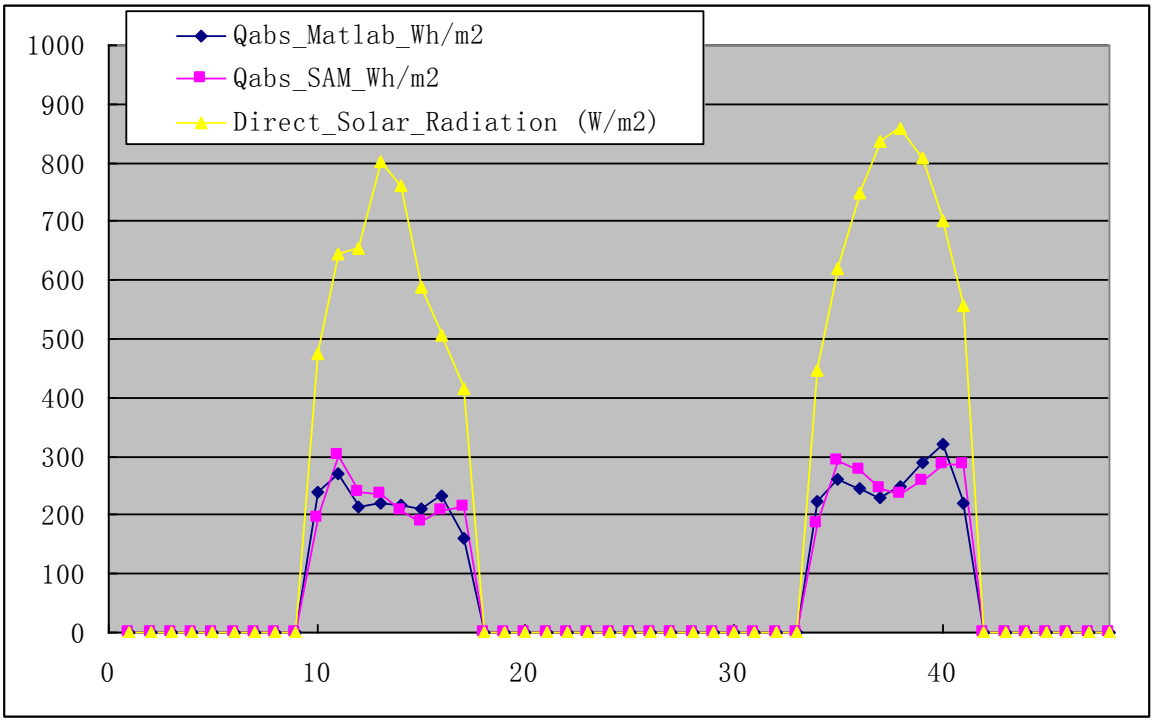

Figure 38: Absorbed Radiation for Jan 1 and 2, 1989

Annual heat loss in the collection field is 67605.5 MWs in the Matlab/Simulink model and is 90449.1 MWs in the SAM model. Figure 39 is the monthly heat loss energy for the HCE.

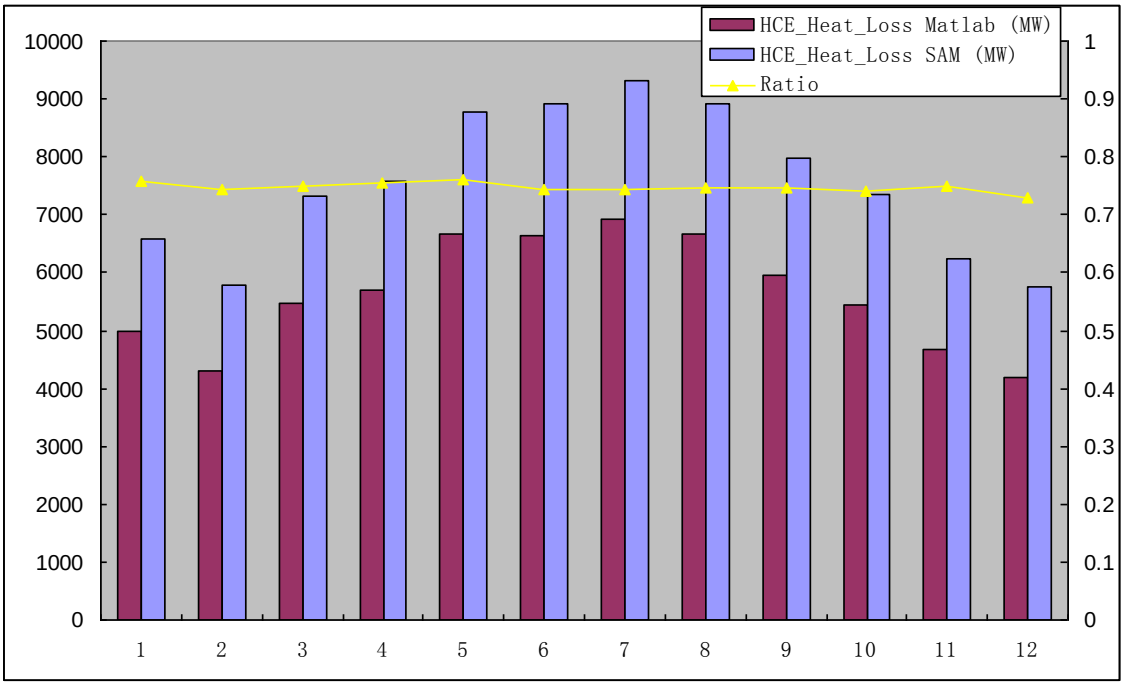

Figure 39: Monthly HCE Heat Loss

A transfer pipe is used to transfer the HTF between the HCE and the storage system or electricity generation system. The detailed information for the transfer pipe is unknown, so the values were estimated for use in the calculation, namely and outer radius of 0.18 m, an inner radius of 0.178 m, a pipe length of 0.035 m per square meter of collection area, with pipe conductivity of 0.2 W/mK and surface emissivity of 0.2.

The annual heat loss in the transfer pipe is 32393.3 MWs in the Matlab/Simulink model and 26209.2 MWs in the SAM model. The annual heat loss for the HCE and the transfer pipe is 99998.7 MWs (Matlab/Simulink model) or 116658.3 MWs (SAM model). Figure 40 is the monthly heat loss for the transfer pipe and Figure 41 is the heat loss for the solar energy collection field.

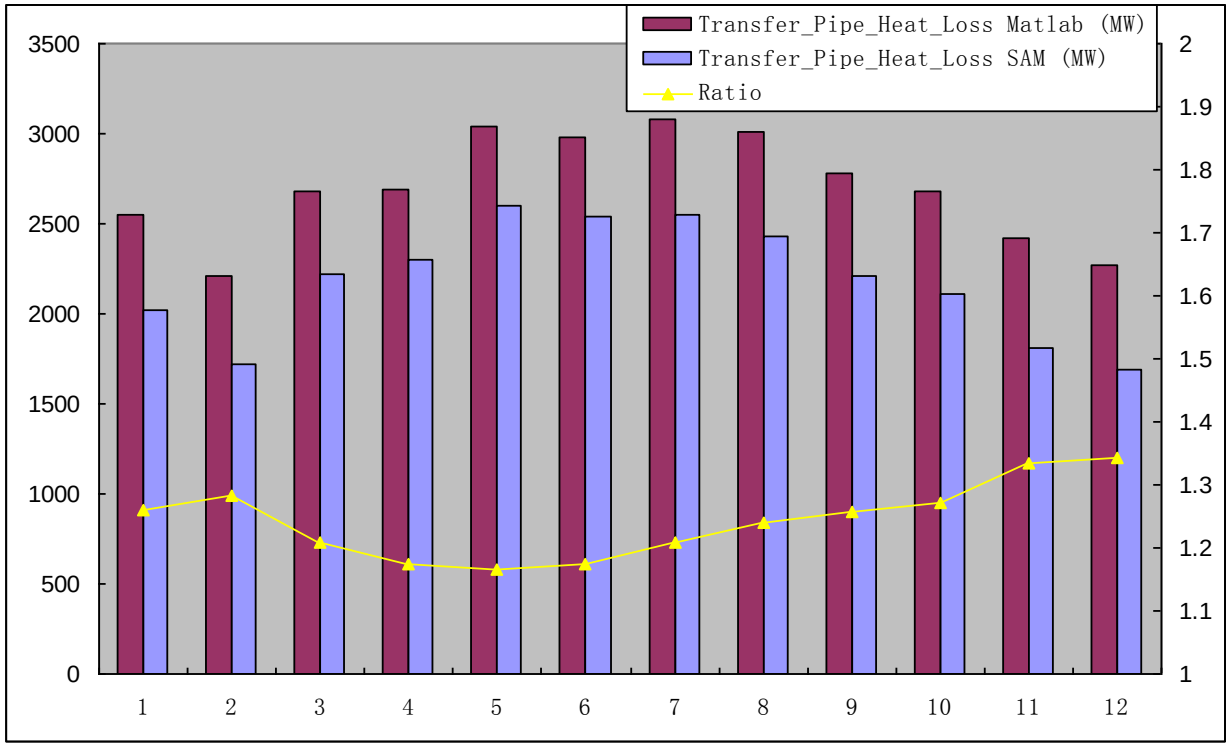

Figure 40: Monthly Transfer Pipe Heat Loss

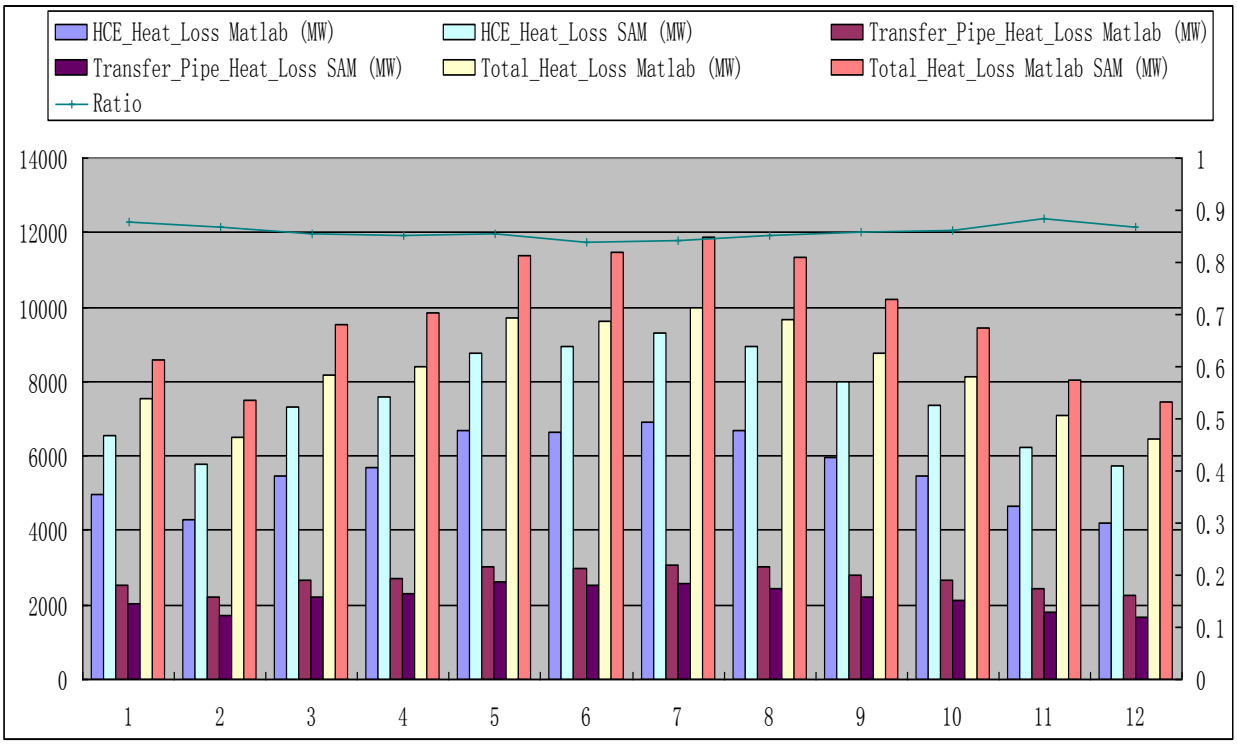

Figure 41: Monthly Solar Collection Field Heat Loss

The annual thermal energy flow output is 532615.1 MW (Matlab/Simulink) and 540336.4 MW (SAM). Figure 42 shows the monthly thermal energy output from the field. Figure 43 shows the monthly energy flow summary for the filed.

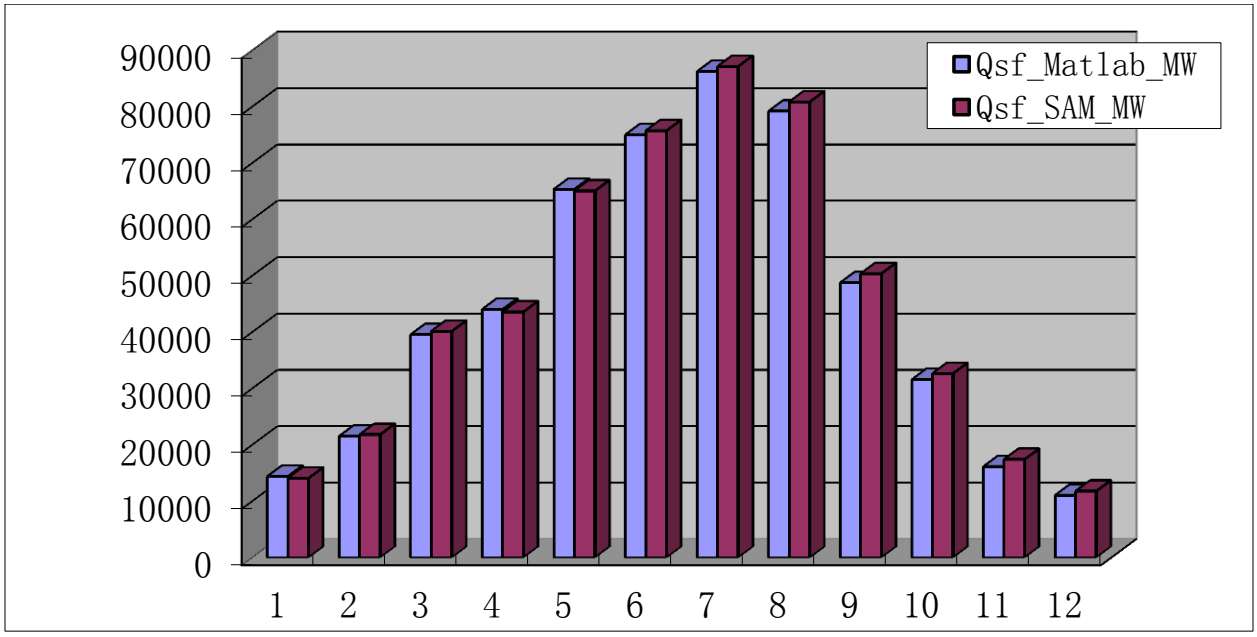

Figure 42: Monthly Solar Field Thermal Energy Output

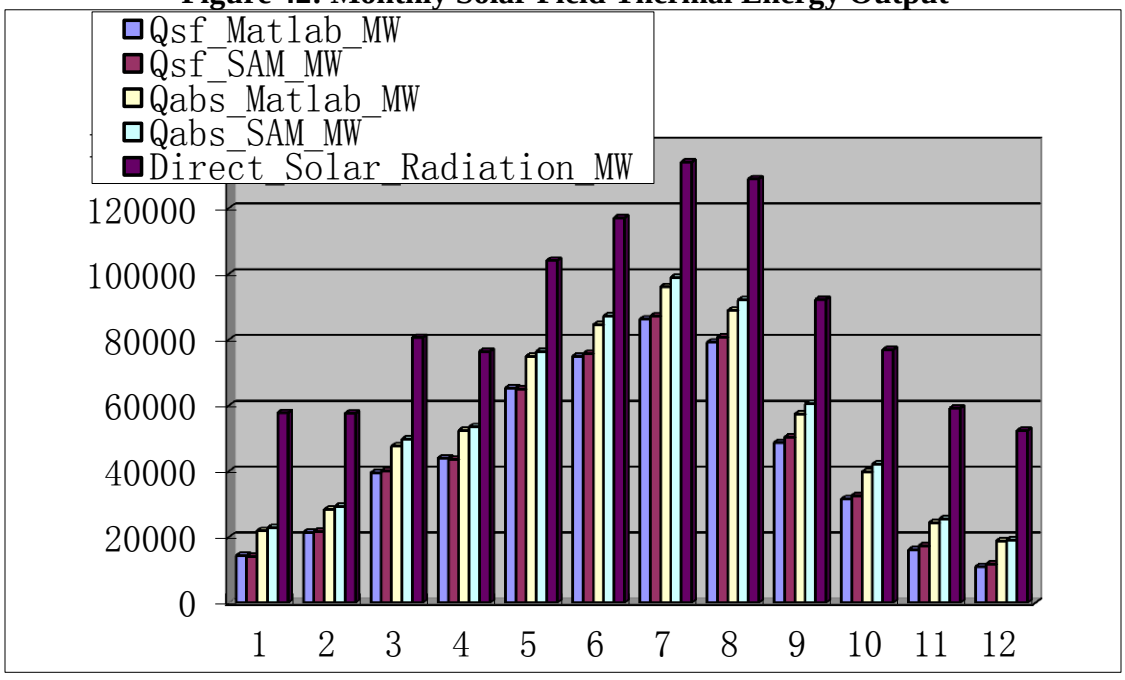

Figure 43: Monthly Summary for Solar Collection Field

The thermal storage system in Andasol-1 consists of two tanks. The hot tank is used for heated thermal energy storage (TES) material, and the cold tank is used for depleted TES material (after

releasing heat to water in electricity generation). The height of the tank is 14 meters while its radius is 18 meters. Other parameters are unknown and have been estimated for the Matlab/Simulink model, as: an isolation layer 0.432 m thick composed of mineral wool with conductivity 00.9 to 0.1 W/mK (depending on temperature), a tank top thickness of 0.15 m with conductivity 1.5 W/mK and emissivity 0.3, a surface emissivity of 0.3, bottom material 0.079 m thick with conductivity 1.5 W/mK, and a bottom isothermal layer 0.61 m thick with conductivity 0.5 W/mK. The ground temperature is 289 K

In the SAM model, the heat loss from the thermal storage system is 0.97 MWs/day This figure represents the sum of hot and cold tank heat loss.

The heat loss in thermal storage system is shown in Figure 44:

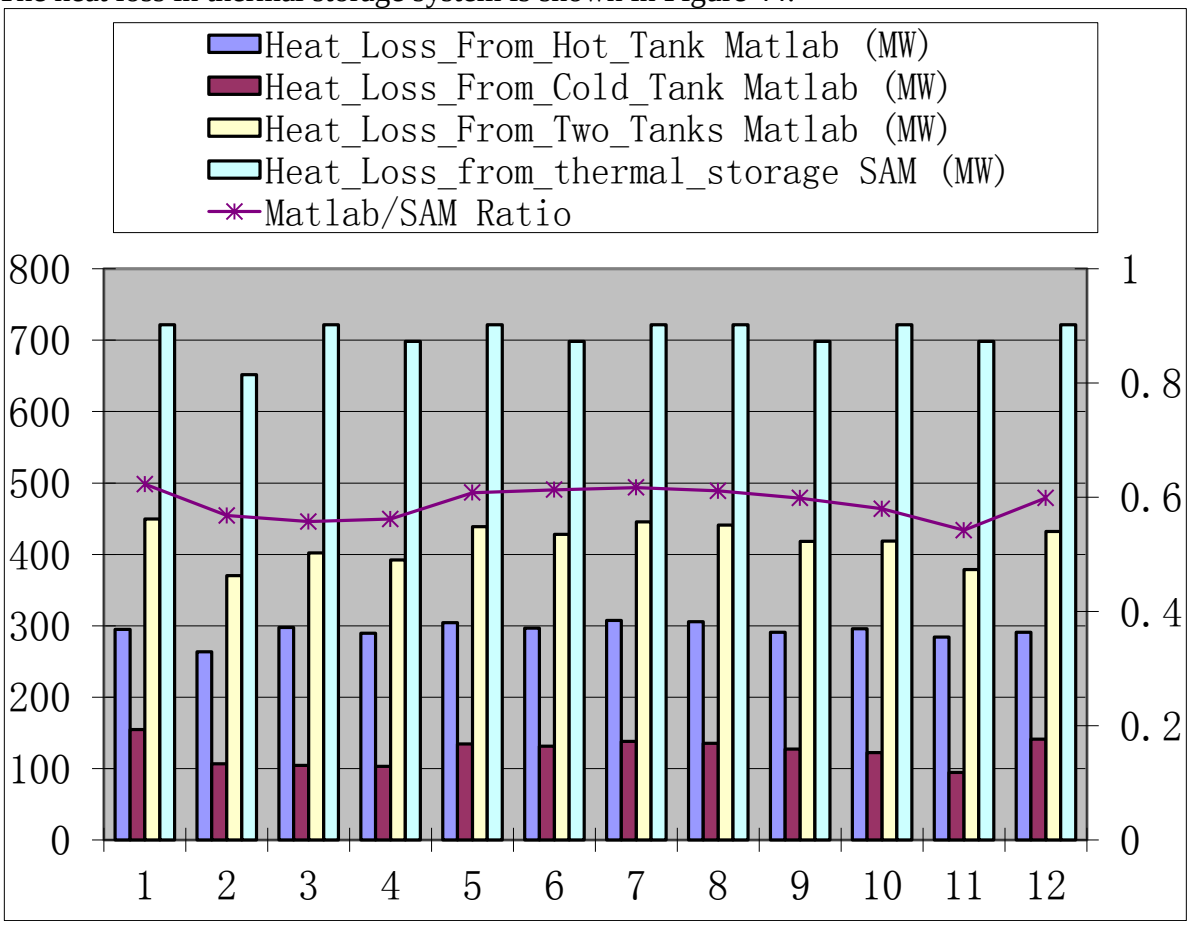

Figure 44: Monthly Heat Loss in thermal storage system

Figures 45, Figure 46 and Figure 47 show the monthly thermal energy flow to electricity generation, dumped energy, and the electricity generation respectively.

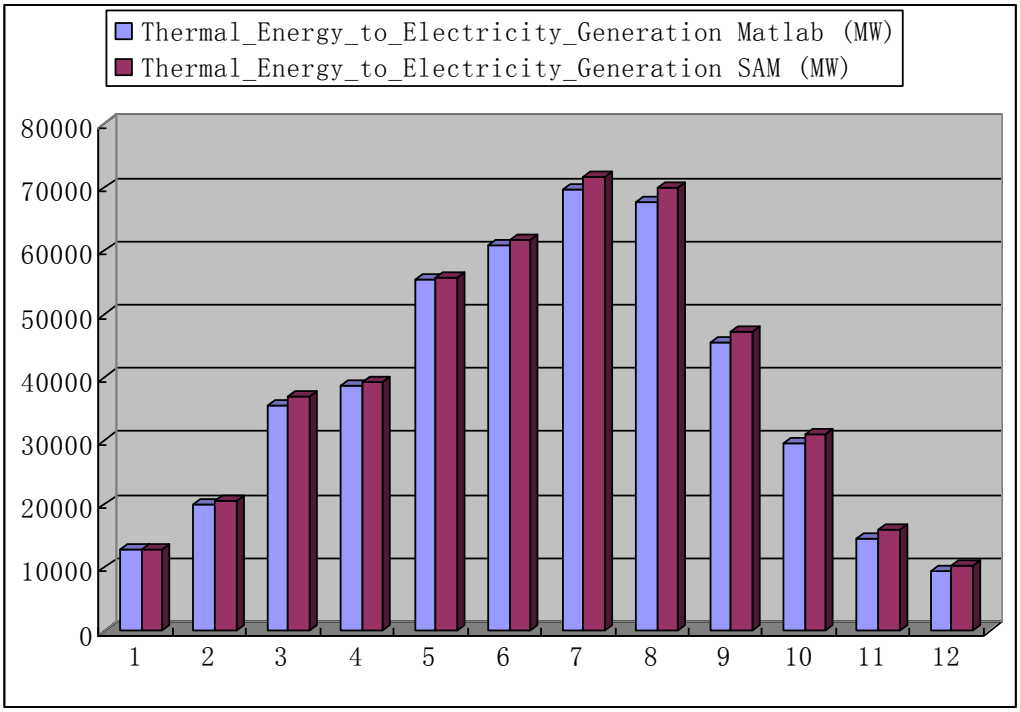

Figure 45: Monthly Thermal Energy Flow to Electricity Generation System (Starting energy does not count)

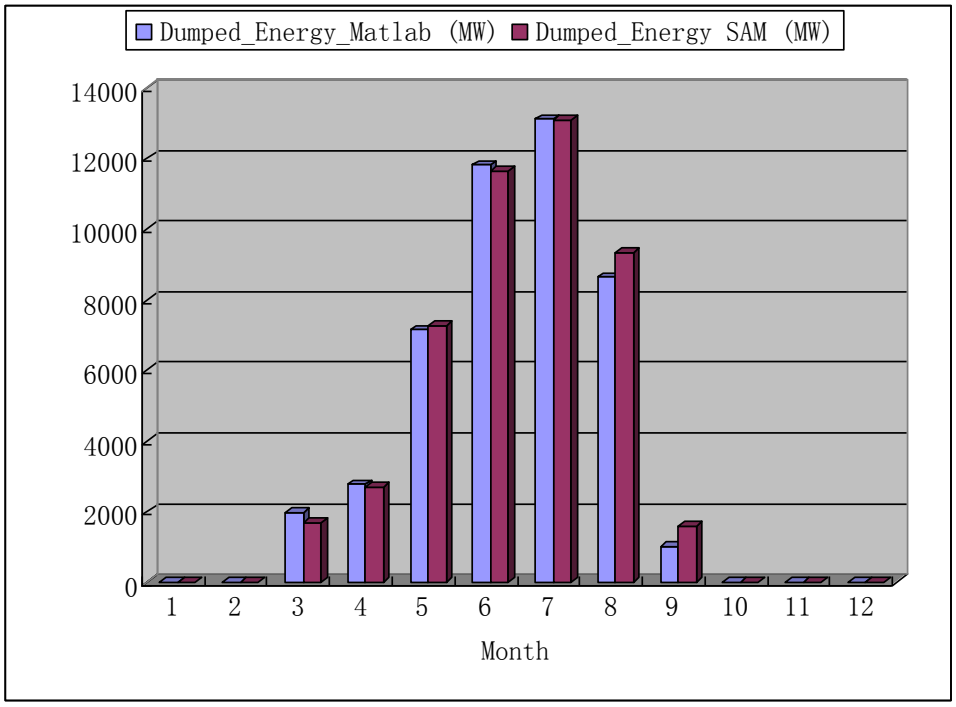

Figure 46: Monthly Dumped Energy

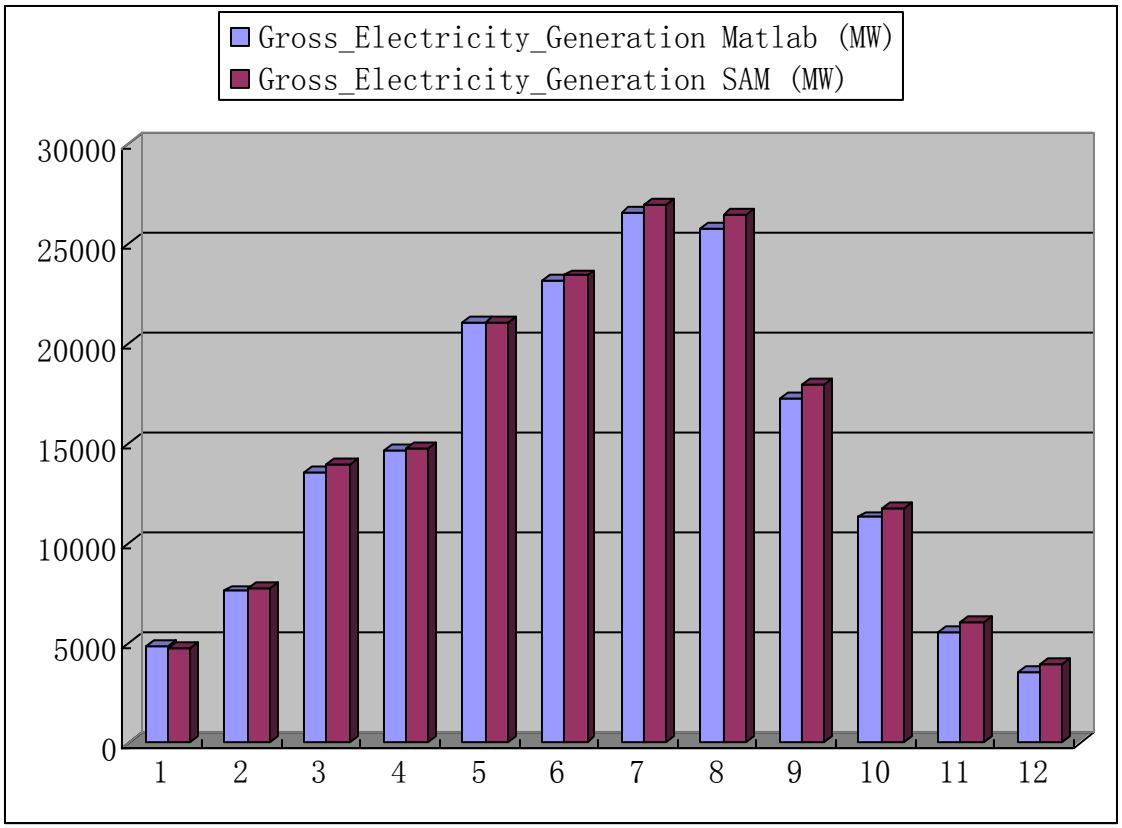

Figure 47: Monthly Gross Electricity Generation

3.5.2.3 Economic Model

Discussion of CSPP is not complete without an examination of economic performance. The economic performance of CSPP will decide whether this technology will survive or die in the future alternative energy competition.

An economic model can help analysts understand how CSPP performs as a system and what affects the cost of energy produced by that system. It supplies a tool to compare the levelized energy cost (LCOE) in the system base, instead of just comparing technologies only. LCOE is useful for comparing alternative options for projects based on different configurations. LCOE indicates the true cost of electricity price rather than the market price.

The economic model is based on cash flow. The income cash flow consists of the electricity sales price, incentive payments, tax deductions, and depreciation debt. The total cost consists of installation, operation and maintenance costs, equipment replacement, salvage cost, and debt payment and interest.

Due to the character of a CSPP plant, only a public utility or independent power producer (IPP) is considered in this model, which means the project earns revenues through electricity sales to cover project costs. The owner pays cash for the equity part of the total installed cost at the

beginning (year 0) of the cash flow, and makes payments on interest and principal in subsequent years.

According to real electricity market requirements, several advanced parameters can be set or obtained to avoid iterative calculations. These parameters include: LCOE, internal rate of return (IRR), minimum DSCR, First year PPA, PPA increase rate, debt fraction.

In this economic model, the time step is a year. Each year's income and cost is sum up to calculate the electricity price. The details of the cost and revenue are given below.

3.5.2.3.1 Cost

The installment is the initial cost to build the power plant. It contains direct and indirect cost. Devices and related labor cost are included in the direct cost category. The indirect cost includes other costs such as management, tax, margin and land-related cost. The direct cost is calculated based on land area, power rate, thermal storage size, and field collection area. The indirect cost is derived from the direct cost.

Loans are money borrowed from a bank at the initial period (year 0), with payback beginning in year 1. In this model, the payback amount is constant over the payback period, and the interest rate does not change with time. At the end of the loan period, the payback should equal all the principal and related interest. The payback period is set and is no longer than the lifetime of power plant. Usually, interest is tax-deductible.

Three kinds of tax are considered. In the initial period, sales tax is considered when purchasing devices. In the operation period, relevant state and federal taxes are considered. However, the tax base requires a complex calculation since some of the cash flow is tax-exempt or tax-deductible. The tax amount is regarded as cost in the economic model.

Operation costs include labor and device operation costs. Generally, this value is set as a constant and escalates by a fixed percentage every year. Maintenance costs include the cost of normal wear and device replacement and may change greatly due to varying needs for component replacement in certain years.

After the lifespan of the power plant, the plant needs to be dismantled. If dismantling leads to negative cash flow, it is considered salvage cost. If dismantling leads to positive cash flow, it is regarded as income. This cash flow is put in the last year of the whole lifespan of the power plant.

3.5.2.3.2 Income

Electricity sales is the revenue from selling the generated electricity. It is the source of most of the revenue of the power plant. The electricity generation amount may decrease over time as devices age and efficiency decreases. In the economic model, a constant decreasing percentage is used for this trend. The electricity price may increase due to inflation or supply and demand). A constant is used for the percentage escalation.

Several kinds of incentives are also considered. These incentives may match part of the investment, or supply a certain credit. Also, it may be supplied only once or last for several

years. The different types of incentives can be used individually or in combination in the economic model. Each incentive has an option to choose whether it is tax-exempt or not.

According to current law, a CSP plant has a 5-year depreciation period. The total depreciation value is defined as equal to the device cost. Two kinds of depreciation methods are included in the model, middle-quarter and half year types. Although depreciation is counted as a cost in the economic definition, it reduces the tax basis and counted as revenue.

Salvage is defined in the cost column. However, as mentioned in the previous section, if the salvage value is positive, the economic model will put the salvage value in the income category.

3.5.2.3.3 Other Limitations

The program has internal bounds that affect the cash flow. These are minimum pre-tax debt Ratio (DSCR), which is the operating income divided by debt and minimum cash flow, which is the minimum cash flow required over the lifespan of the plant. Setting these two values maintains the project risk within limits.

3.5.2.3.4 Calculation

The economic model calculation uses an iterative method to obtain the LCOE price of electricity. The result is output to the same Excel file as the performance model in a separate sheet. Figure 48 shows the economic model calculation procedure.

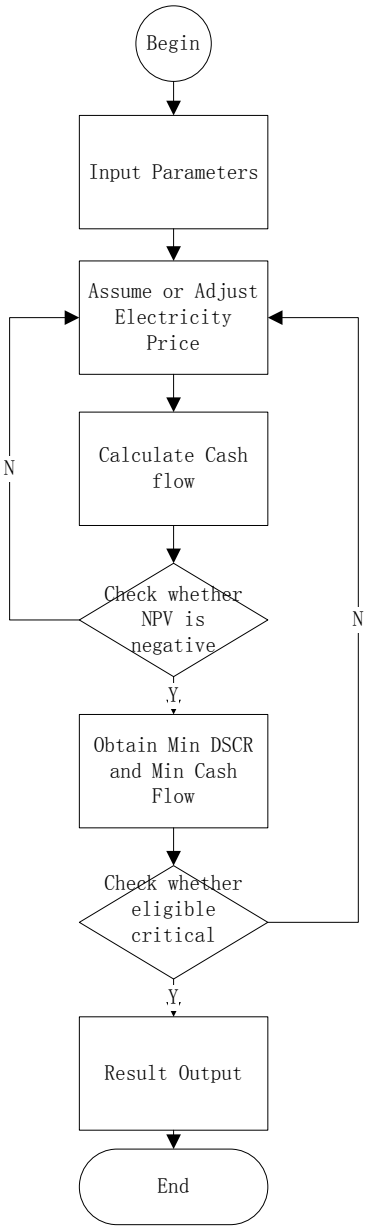

Figure 48: Calculation routine for economy model

4 Results

4.1 Nitrate Eutectic Salt Mixtures

As discussed above, the MDSC method is still relatively new, and used exclusively with Thermal Analysis (TA) products. Therefore, a series of validation runs were performed to demonstrate the accuracy of the MDSC method using the parameters listed. Since the method used was MDSC, the raw output was specific heat, in J/gK. All tests were performed with the same sapphire sample, but were run on different dates with different pan pairs, in order to emulate standard MDSC test runs using different samples. Four such tests were performed, with two tests using a temperature range of 100° C to 600° C, and the other two ranging from 300° C to 600° C. The specific heat results are shown in Figure 49, with the error compared to reference values shown in Figure 50. While the sapphire specific heat data was taken over a wider range than shown in the figures, the accuracy at temperatures lower and higher than the nitrate thermal profile measurement cycles is irrelevant to this investigation, and was therefore not shown. The error was found by calculating percentage difference between the reference and observed specific heat.

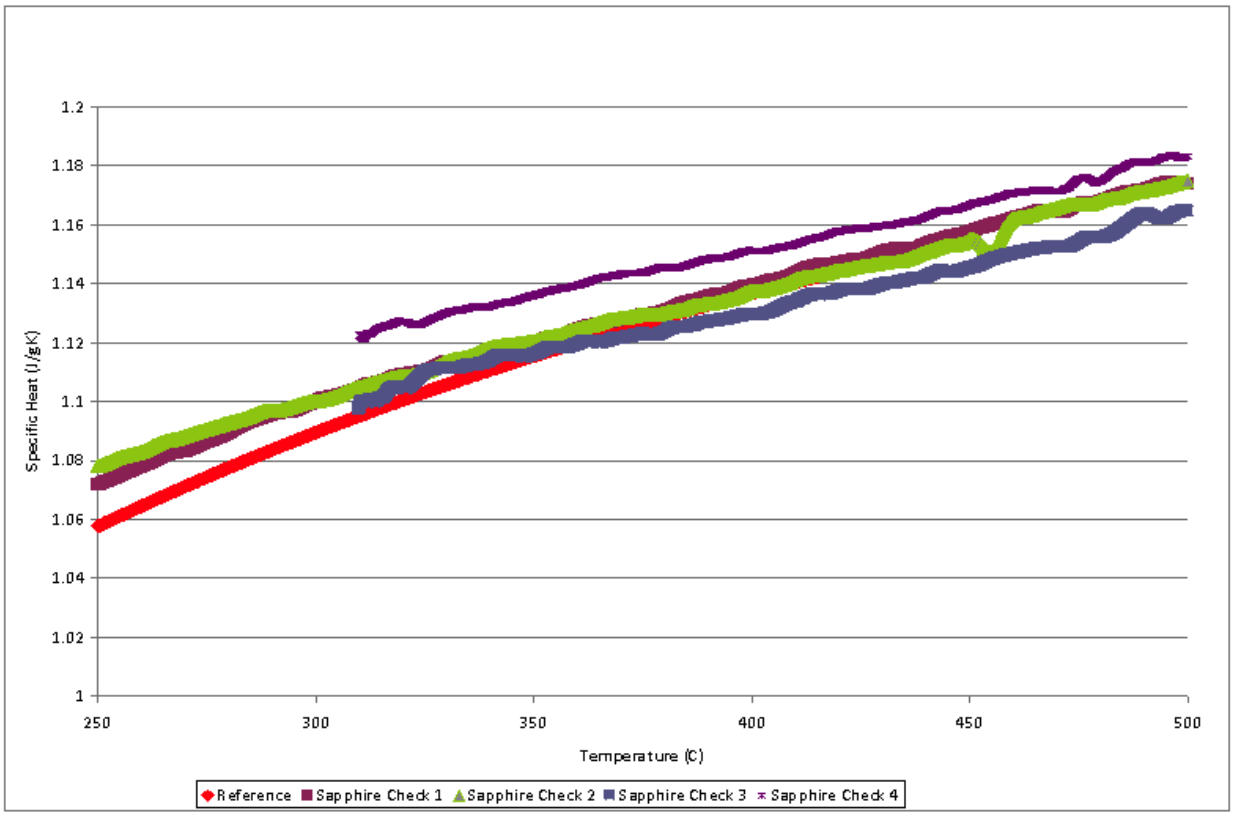

Figure 49: MDSC Observed Sapphire Specific Heat. The observed specific heat matches very closely to reference values.

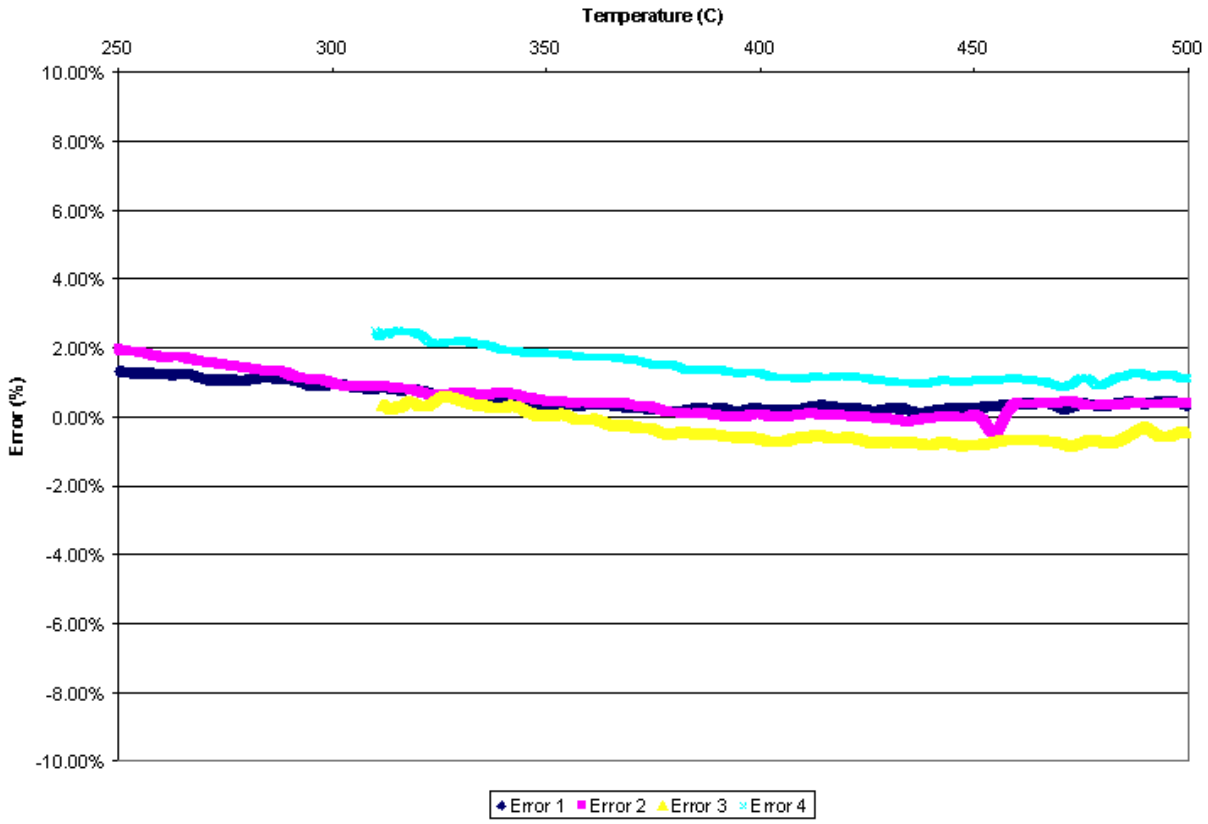

Figure 50: Observed Sapphire MDSC Error, showing an average error of approximately 2-3%.

Based on the observed error shown in Figure 50, a standard uncertainty range of approximately 3% seems to be sufficient to encompass most of the observed error. The observed error is within the manufacturer's specifications of 5% error. There was a large initial error present in every MDSC measurement, and MDSC parameter testing not included in this investigation showed it to be a time-based, rather than temperature-based effect. Therefore, MDSC measurements require a certain amount of "settling time" to come to the true observed value. The large initial error seems to be inherent to the MDSC method, as every MDSC test performed, regardless of the material or parameters used, showed the same initial error spike. The MDSC method using the parameters discussed in the Method section showed superb correlation with expected reference values, and showed an average error below 2%. This performance allows for great confidence in the MDSC specific heat results outside the ASTM E2716 temperature range. The specific heat accuracy also suggests the MDSC settings as described in the Method section were optimal for the pan and temperature range used in this investigation.

4.1.1 Specific Heat Results

The summarized results of all measurements are shown in Table 10. The data was taken using measurement techniques as described in the Method section. A sample consists of one mass-matched reference and sample pan set, and the contents of the sample pan, which was the material being tested. The temperature profiles given in Figure 13 and Figure 14 show a total of

four temperature ramps. The first ramp, as mentioned in the Method section, is to melt the sample into a liquid and condition the machine. The other three ramps are the measurement cycles to gather the data. A run consists of the data gathered from executing the temperature profile once. The specific heat values shown in Table 10 are the averaged values from each of the three measurement cycles for each sample. The heat of fusion measurements were taken after the specific heat measurements, in order to prevent geometry effects (as the material freezes and melts) from altering the specific heat data.

Table 10: Summarized specific heat and heat of fusion results for all tests.

Test Number	Nano-particle	Measurement Type	Maximum Temperature (° C)	Sample Mass (mg)	Cp at 350C Average (J/gK)	Heat of Fusion Average (J/g)
1	none	ASTM	450	12.62	1.54	n/a
2	none	ASTM	450	8.66	1.61	n/a
3	none	ASTM	450	18.57	1.59	n/a
4	none	MDSC	400	10.20	1.57	87.84
5	none	MDSC	400	11.00	1.46	88.37
6	none	MDSC	450	7.21	1.54	101.50
Group Average					1.55	92.57
7	alumina	ASTM	450	6.48	2.07	n/a
8	alumina	ASTM	450	7.10	1.90	n/a
9	alumina	ASTM	450	17.47	1.80	n/a
10	alumina	MDSC	450	9.86	varies	n/a
11	alumina	MDSC	450	7.94	1.81	97.29
12	alumina	MDSC	450	10.45	1.73	101.27
13	alumina	MDSC	450	8.56	1.91	99.59
14	alumina	MDSC	450	8.20	1.84	103.77
Group Average					1.87	100.48
15	silica	ASTM	350	5.18	1.91	n/a
16	silica	ASTM	400	9.77	2.00	n/a
17	silica	ASTM	450	10.44	1.76	115.73
18	silica	MDSC	450	7.26	varies	n/a
19	silica	MDSC	425	9.41	varies	n/a
20	silica	MDSC	400	9.77	n/a	n/a
21	silica	MDSC	400	9.77	1.84	97.62
22	silica	MDSC	400	10.23	1.72	91.43
23	silica	MDSC	400	12.99	1.82	95.56
Group Average				average	1.84	100.09

The statistical analysis of the data in Table 10 is shown in Table 11. The average values in Table 11 were generated using the data from both methods for each material. The standard deviation was generated in the same way, using all the data for each material type. The 90% confidence interval was generated using the standard deviation given in the first column of Table 10, and the maximum and minimum were created using the 90% confidence interval data.

Table 11: Statistical analysis of the data from Table 9, showing the 90% confidence interval and standard deviation**.**

Test Material	Measured Heat of Fusion			
	Average Value J/g	Standard Deviation J/g	90% Confidence Maximum J/g	90% Confidence Minimum J/g
Nitrate	92.57	7.738	105.3	79.8
Nitrate + $Al2O_3$	100.48	2.734	104.9	95.9
Nitrate + SiO_2	100.09	10.744	117.8	82.4
	Specific Heat at 350° C			
	J/gK	J/gK	J/gK	J/gK
Nitrate	1.55	0.050	1.63	1.47
Nitrate + $Al2O_3$	1.87	0.108	2.04	1.69
Nitrate + SiO_2	1.84	0.103	2.01	1.67

The averages of each material's specific heat values over the temperature range are shown in Figure 51. The data presented in the figures was generated by both the ASTM 1269E calculations as presented in the Method section and by MDSC results as a direct output of the DSC. The results of both methods were then plotted against temperature to generate Figure 51. Figure 52 shows the same data as presented in Figure 51, but presents it as a ratio against the base nitrate. A value greater than 100% indicates the specific heat is higher than the base nitrate. As can be seen in Figure 52, the specific heat of the composite materials is always higher than the base nitrate.

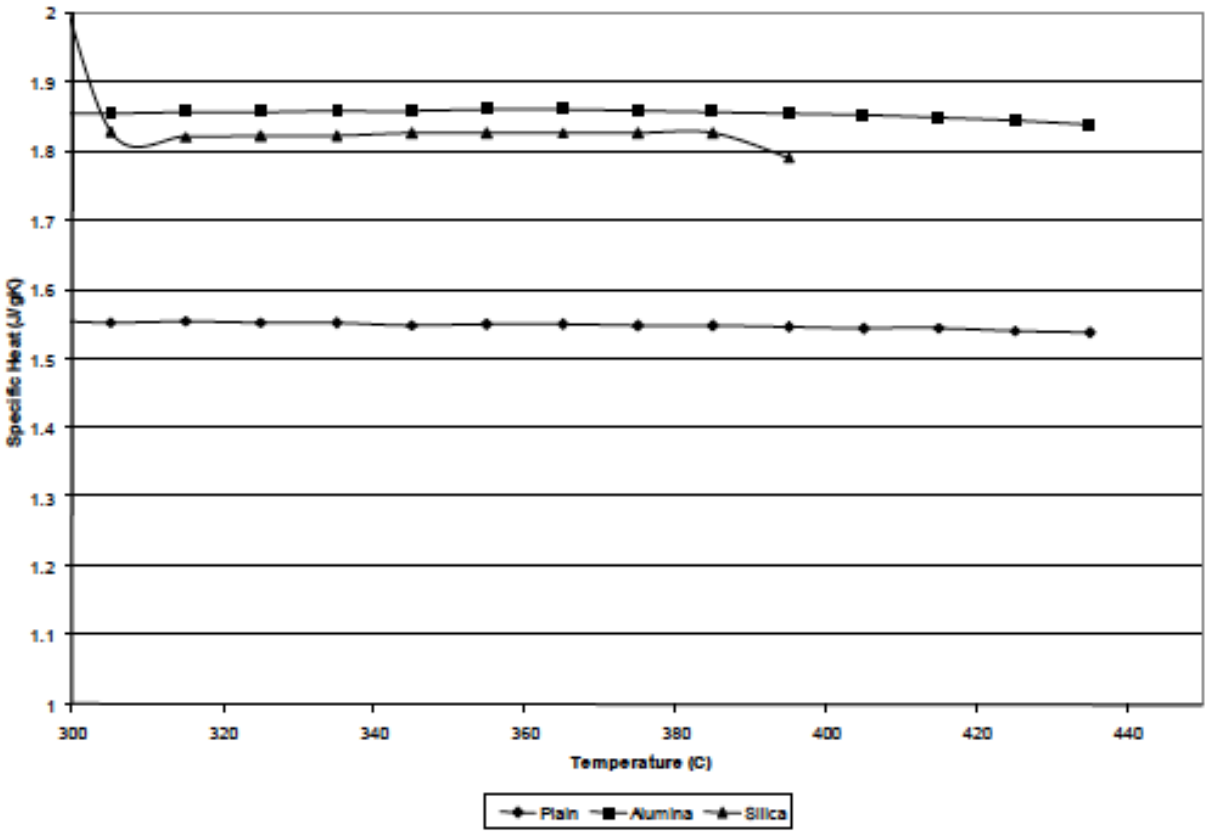

Figure 51: Specific Heat Results for All Tested Materials.
These results are the averages of all tests at specific temperatures. The composite materials always showed a higher specific heat than the plain nitrate.

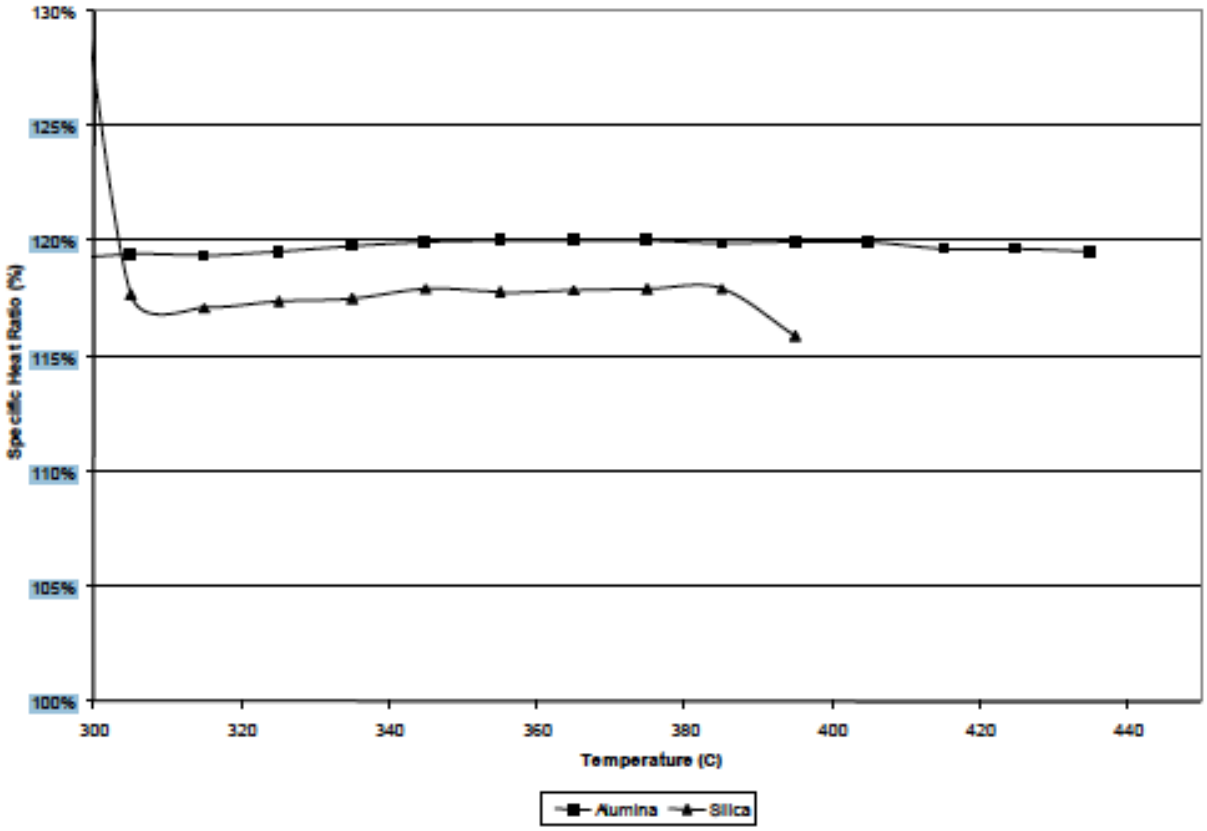

Figure 52: Specific Heat Ratios of All Tested Materials.
This plot shows the specific heat ratio between the composite and base material at investigated temperatures. In this plot, the base nitrate always has a value of 100%. The composite materials always showed at least 15% improvement in specific heat compared to the base nitrate.

The ASTM and MDSC specific heat results for each material are shown in Table 12. These results were generated using the data shown in Table 10. Each material's method-specific data was used to generate the data in Table 12, meaning, for example, that the ASTM standard deviation for the plain nitrate was generated only using ASTM 1269E plain nitrate results, listed as runs 1, 2, and 3 in Table 9. The other table entries were generated in the same manner. The enhancement percentage was found by comparing the specific heat results of the composite nitrate against the plain nitrate.

The overall specific heat results shown in Table 10 and Table 11 support the hypothesis that the addition of nanoparticles improves the specific heat capacity. The exact degree of improvement is unclear, as evidenced by the standard deviation values shown in Table 11. Based on the average values, the nitrate and alumina showed approximately equivalent enhancement of the specific heat as the nitrate and silica. The results are a combination of MDSC and ASTM methods, and both methods provided similar results. The combined method improvement values are shown in Table 13, and are taken from Table 10.

Table 12: ASTM and MDSC specific heat statistics. The observed specific heat enhancement for both methods is approximately the same. The MDSC had lower standard deviation results than ASTM for almost all runs.

	ASTM			MDSC		
	Average	Standard Deviation	Enhancement	Average	Standard Deviation	Enhancement
Nitrate	1.58	0.037	0.0%	1.52	0.053	0.0%
Nitrate + $Al2O_3$	1.93	0.116	22%	1.82	0.073	20%
Nitrate +SiO_2	1.89	0.122	20%	1.80	0.068	18%

Table 13: Combined Specific heat enhancement percentage. Note that the enhancement for both materials is approximately the same.

Material	Average Specific Heat (J/gK)	Enhancement(%)
Nitrate	1.55	n/a
Nitrate + $Al2O_3$	1.87	20%
Nitrate + SiO_2	1.84	19%

The exact quantity of enhancement is somewhat open for interpretation, given the 90% confidence interval range as seen in Table 11, but the same data suggests there is a clear enhancement based on the same 90% confidence interval range. The average values presented in Table 13 were determined using both MSDC and ASTM methods to provide a wider range of data from which to pull.

4.1.1.1 ASTM and MDSC Result Comparison

Both the ASTM and MDSC methods provided specific heat data within one standard deviation of the reference value for the plain nitrate, as can be seen in Table 11. This suggests that both methods were accurate at the temperatures used for the tested materials. However, for the nanoparticle composite materials, the two methods provided specific heat information outside of one standard deviation relative to the average of the other method for the same material. Each method's average is within the other method's 90% confidence interval, however, suggesting the two methods at least provide similar data. The other disparity between the two methods is in their standard deviations. The MDSC standard deviations are, with the exception of the plain nitrate, smaller than those of the ASTM method. This suggests the MDSC method has lower uncertainty than the ASTM method, at least under the conditions outlined in the Method section. A potential additional uncertainty source is the multi-step nature of the ASTM method. Since the method is comprised of three individual runs, the sample pan must be removed and placed on the sensor three different times, compared to the single time required by the MDSC method. A second possible reason for the higher uncertainty stems from the use of hermetic pans. The hermetic pans must be crimped shut once the sample is inside. However, since the ASTM

method requires the use of the same pans with different samples (nothing, sapphire, and unknown sample) the pan could not be sealed until the unknown sample was put in the pan. Therefore, the pan may have behaved differently during the sample run compared to the previous runs.

The larger question is which method is closer to the actual specific heat of the composite materials as the ASTM method always gave higher specific heat results than the MDSC method for the composite materials. It then becomes a question of which method is more accurate. The ASTM method has been verified and used for many decades, while the MDSC method is still relatively new. The MDSC method is also not approved by the ASTM committee for the same temperature range used in this thesis. The MDSC method has been shown to be valid at the tested temperatures using sapphire standards tested under the same conditions as the unknown samples, as seen in Figure 49. The ASTM method internally validates itself by recalibrating itself in every run. Therefore, it could be concluded that both methods are valid, even though they give different results.

With this in mind, the approximate specific heat enhancement for both of the composite materials is 20%, as shown by both the ASTM 1269E method and the MDSC method.

4.1.1.2 Nitrate + Alumina Specific Heat vs Alumina Concentration

Hot plate evaporation was used to synthesize nanofluid with nominal Al_2O_3 nanoparticle mass fractions of 0.125%, 0.25%, 0.5%, 0.75%, 1%, 1.5%, and 2%. For this set of samples, the actual Al_2O_3 nanoparticle mass fraction was measured by Neutron Activation Analysis; the specific heat, melting point and heat of fusion by Differential Scanning Calorimetry; and thermal diffusivity and thermal conductivity by Laser Flash Analysis.

4.1.1.2.1Alumina mass Fraction from Neutron Activation Analysis.

The actual mass fraction values of aluminum $\varphi'(Al)$ in the nanofluid were measured using NAA. The actual mass fraction of alumina $\varphi'(Al_2O_3)$ was calculated using Eq. 11. Three separate NAA tests were run for each nominal mass fraction of alumina. The nominal mass fraction of alumina $\varphi(Al_2O_3)$, actual mass fraction of aluminum $\varphi'(Al)$ and alumina $\varphi'(Al_2O_3)$ of each sample are presented in Table 14. In the following discussion, actual alumina mass fraction will be used in analysis.

Table 14: Actual mass fraction of alumina nanoparticle from NAA

$\varphi_{Al_2O_3}$ (%)	φ'_{Al} (%)	$\varphi'_{Al_2O_3}$ (%)	STDEV
0	0	0	0
0.125	0.05	0.09	0.011
0.25	0.09	0.17	0.004
0.50	0.16	0.30	0.032
0.75	0.28	0.53	0.039
1	0.41	0.78	0.059
1.5	0.51	0.96	0.171
2	0.63	1.19	0.120

4.1.1.2.2 DSC Results.

The specific heats for all nanofluids with different alumina nanoparticle mass fractions were measured on a DSC with three repeats. The specific heats (C_p) of each nanofluid at 350° C are shown in Table 15. The coefficients of variation of the tests are within 5%.

Table 15: The specific heat of the nanofluids at 350 °C from DSC

$\varphi'_{Al_2O_3}$ (%)	Average Specific Heat (J/gK)	STDEV	Coefficient of Variation (%)
0	1.47	0.042	2.8
0.09	1.69	0.012	0.7
0.17	1.62	0.035	2.1
0.30	1.77	0.015	0.9
0.53	1.83	0.006	0.3
0.78	1.92	0.029	1.5
0.96	1.82	0.050	2.7
1.19	1.68	0.029	1.7

According to the specific heat values shown in Table 15, the nanofluid exhibits a maximum 30.6% enhancement of specific heat with 0.78% mass fraction of alumina nanoparticles (about 1.92 J/gK). Figure 53 shows the specific heat of alumina-nitrate nanofluid as a function of nanoparticle mass fraction with the uncertainties of both the alumina mass fraction and the specific heat. It is noticeable that there exists a parabolic relation between specific heat and mass fraction of alumina nanoparticles. A polynomial curve fit to the data is shown in Eq. (22).

$$C_p = 1.43 + 1.39\varphi - 1.08\varphi^2 + 0.074\varphi^3 \qquad (22)$$

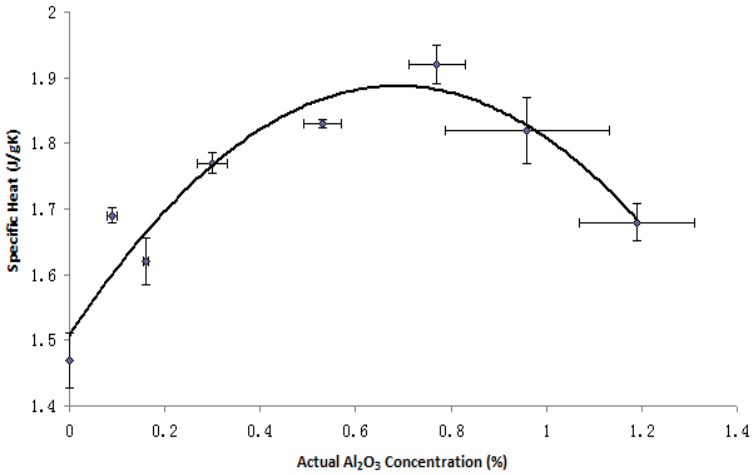

Figure 53: The Specific Heats of the Nanofluids with Different Mass Fractions of Alumina Nanoparticle

4.1.2 Heat of Fusion Results

The heat of fusion results and statistical analysis are shown in Table 10 and Table 11. The heat of fusion measurement, as described in the Method section, is the definite integral of the heat flow, with the integration limits of the onset to the offset temperature of the melt. The heat of fusion measurements were taken after specific heat data was taken. The heat of fusion measurements were taken only during the MDSC runs because the ramp rates required by the heat of fusion measurement match those required by the MDSC specific heat measurement. The observed heat of fusion is significantly lower than the reference value given by the base material manufacturer. The reason for this alteration is unknown. If the observed heat of fusion of the plain processed material is considered a baseline value, then the nanoparticle composite materials do not seem to have significantly altered the heat of fusion.

4.1.2.1 Heat of Fusion and Melting Point vs Alumina Concentration

Table 16 presents heat of fusion and melting point data of the nanofluids with varying alumina concentrations. As shown in the table, there is no large difference among them. The coefficient of variation for the heat of fusion is only 2% and for the melting point only 0.2%.

Table 16: Heat of fusion and melting point of the nanofluids from DSC

$\varphi_{Al_2O_3}$ (%)	Heat of Fusion (J/g)	Melting Point (^{o}C)
0	105.3	213.4
0.09	100.0	213.7
0.17	99.6	214.1
0.30	101.1	213.5
0.53	102.1	214.7
0.78	99.7	214.8
0.96	101.8	213.8
1.19	100.3	214.5
Average	101.2	214.1
STDEV	1.8	0.5
Coefficient of Variation (%)	2.0	0.2

4.1.3 Stability Results

As described in the Method section, the stability of nitrate eutectic nanoparticle mixtures was determined by comparing the specific heat at a given temperature between successive measurement cycles. A stable mixture will show a small change between cycles, lower than the machine's uncertainty. An unstable material will show a significant change in specific heat between cycles. Each material has its own table, shown in Table 17, Table 18, and Table 19. These tables were generated by the procedure described in the Method section. All specific heat values were taken at 350C, and all tables used the same runs from Table 10.

Plain Nitrate Stability Results

Table 17: Plain Nitrate Stability Analysis. The plain nitrate was shown to be stable, as the cycle-to-cycle changes were within the DSC's uncertainty.

Nitrate Run Number	**Method**	**Date**	Temp. (° C)	Mass **(mg)**	Cycle 1	Cycle 2	Cycle 3	Cycle 1->2 (%)	Cycle 2->3 (%)
1	ASTM	8/10/2010	450	12.62	1.512	1.545	1.550	2.18%	0.32%
2	ASTM	8/16/2010	450	8.66	1.583	1.616	1.619	2.08%	0.19%
3	ASTM	8/30/2010	450	18.57	1.580	1.588	1.591	0.51%	0.19%
6	MDSC	9/28/2010	450	7.21	1.544	1.536	1.533	-0.52%	-0.20%

Based on the previously established stability criterion, the nitrate was stable up to 450° C, as all the cycle-change analysis showed, at worst, a change below 1%. This change is well within the uncertainty of the DSC, which, as established by the test sapphire runs, is approximately 3%. The other runs all showed a per-cycle difference of no more than 2.5%, so there was no significant shift in the specific heat of the nitrate over the run duration. As seen in Table 17, Runs 4 and 5 are not present. This is because those runs did not have the multiple cycles of other runs, but were valid specific heat tests of the plain nitrate using MDSC under the same conditions as the other tests.

Table 18: Nitrate + Alumina Stability Analysis. The nitrate + alumina was stable in nearly every test.

Nitrate +Alumina Run Number	**Method**	**Date**	Temp (° C)	Mass (mg)	Cycle1 (J/gK)	Cycle 2 (J/gK)	Cycle3 (J/gK)	Cycle 1->2 (%)	Cycle 2->3 (%)
7	ASTM	8/12/2010	450	6.48	2.022	2.086	2.095	3.17	0.43
8	ASTM	8/13/2010	450	7.10	1.872	1.915	1.922	2.30	0.37
9	ASTM	11/11/2010	450	17.47	1.807	1.863	1.742	3.10	-6.49
10	MDSC	11/5/2010	450	9.86	1.561	1.548	1.260	0.83	-18.60
11	MDSC	9/18/2010	450	7.94	1.799	1.808	1.813	0.50	0.28
12	MDSC	10/1/2010	450	10.45	1.733	1.725	1.756	0.46	1.80
13	MDSC	10/2/2010	450	8.56	1.888	1.901	1.931	0.69	1.58
14	MDSC	10/3/2010	450	8.20	1.824	1.845	1.856	1.15	0.60

The majority of the tests showed cycle to cycle variations below the DSC uncertainty. The exceptions are runs 9 and 10. These runs showed significant variations between cycles. Run 9 is strange in that is shows an increase, then a decrease in specific heat. The total percentage shift between cycle 1 and cycle 3 is small, but it is unknown why there would be an increase followed by a decrease. The other aberrant sample, run 10, showed a significant decrease in the cycle 2 to 3 comparison. The reasons for this are unclear, but as it only happened in one cycle of one sample, it seems to be an outlier. Additionally, that single sample showed a significantly lower specific heat than any other nitrate + alumina sample, so it seems that the sample itself was different from the other tested samples.

Table 19: Nitrate + Silica Stability Analysis. Above 400 C, the nitrate + silica was unstable.

Nitrate +Silica Run Number			Temp (° C)	Mass (mg)	Cycle 1 (J/gK)	Cycle 2 (J/gK)	Cycle 3 (J/gK)	cycle 1->2 (%)	cycle 2->3 (%)
15	ASTM	7/30/2010	350	5.18	1.706	1.842	1.876	7.97%	1.85%
16	ASTM	8/2/2010	400	9.77	1.943	1.999	2.002	2.88%	0.15%
17	ASTM	8/20/2010	450	10.44	1.824	1.737	1.727	-4.77%	-0.58%
18	MDSC	11/1/2010	450	7.26	1.359	1.190	1.079	-12.44%	-9.33%
19	MDSC	11/1/2010	425	9.41	1.720	1.668	1.599	-3.02%	-4.14%
20	MDSC	11/3/2010	400	9.77	1.731	1.728	1.727	-0.17%	-0.06%
21	MDSC	9/20/2010	400	9.77	1.825	1.849	1.854	1.32%	0.27%
22	MDSC	9/29/2010	400	10.23	1.688	1.721	1.743	1.95%	1.28%
23	MDSC	9/30/2010	400	12.99	1.806	1.825	1.839	1.05%	0.77%

A significant observed secondary property of the nitrate + SiO_2 1% mixture was a temperature-dependent specific heat reduction during the runs. Above 400° C, the composite material showed a discernable decline in observed specific heat. Several runs were used to determine this temperature limit, as seen in Table 19. Figures 54-59 show the time and temperature based specific heat plots, to show more clearly the decay effect. The plots show the data from two separate runs of the same sample, one using the ASTM method, the other using the MDSC method. For example, Figure 54 and Figure 55 show tests of the same sample, with Figure 54 being the ASTM test and Figure 55 being the MDSC test. The ASTM test was run first, then the MDSC test was run on the same sample second. The time plots use the MDSC method, as the individual profile duration of the MDSC method is several times longer than the ASTM sample run. This difference in duration allows the MDSC run to more clearly show the property changes over time.

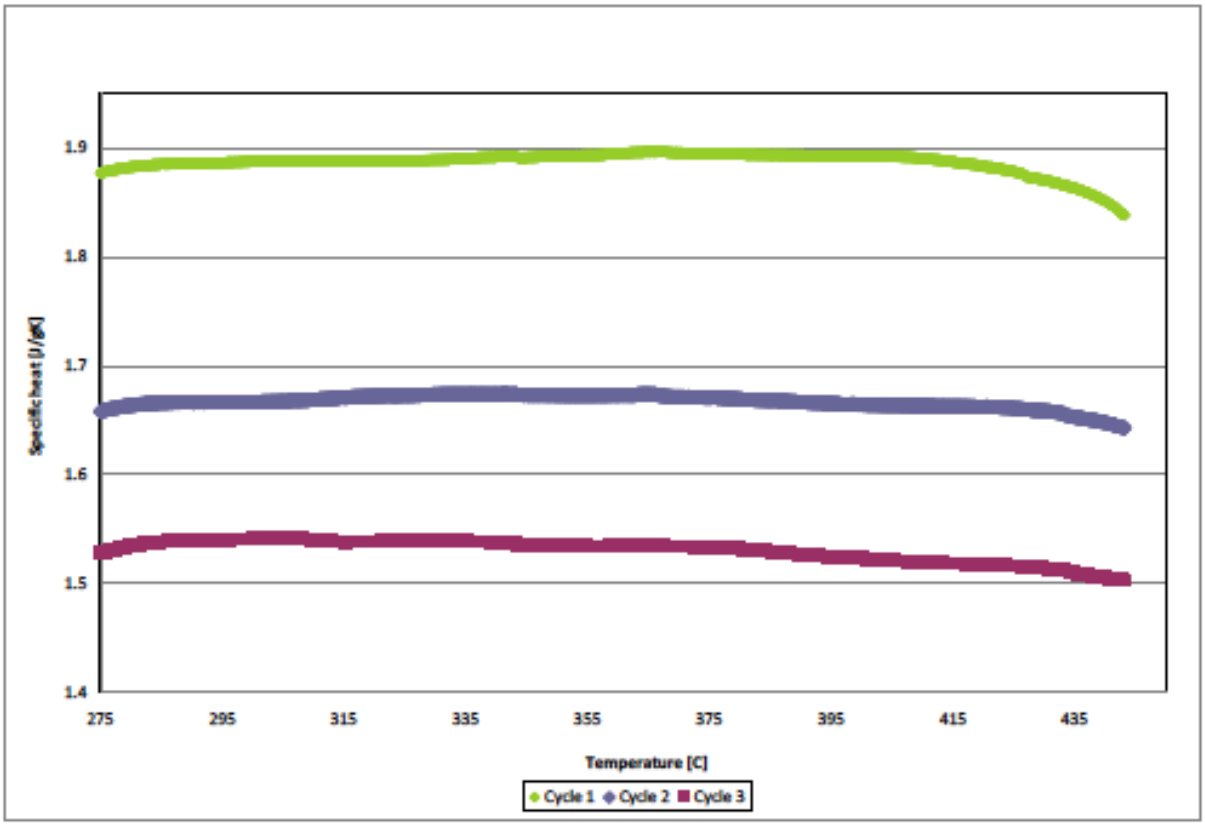

Figure 54: Specific Heat of Nitrate and Silica 450° C Maximum Temperature Run, showing the significant decrease in specific heat from cycle to cycle. Cycle 1 has the highest specific heat, followed by cycle 2 in the middle, and cycle 3 with the lowest.

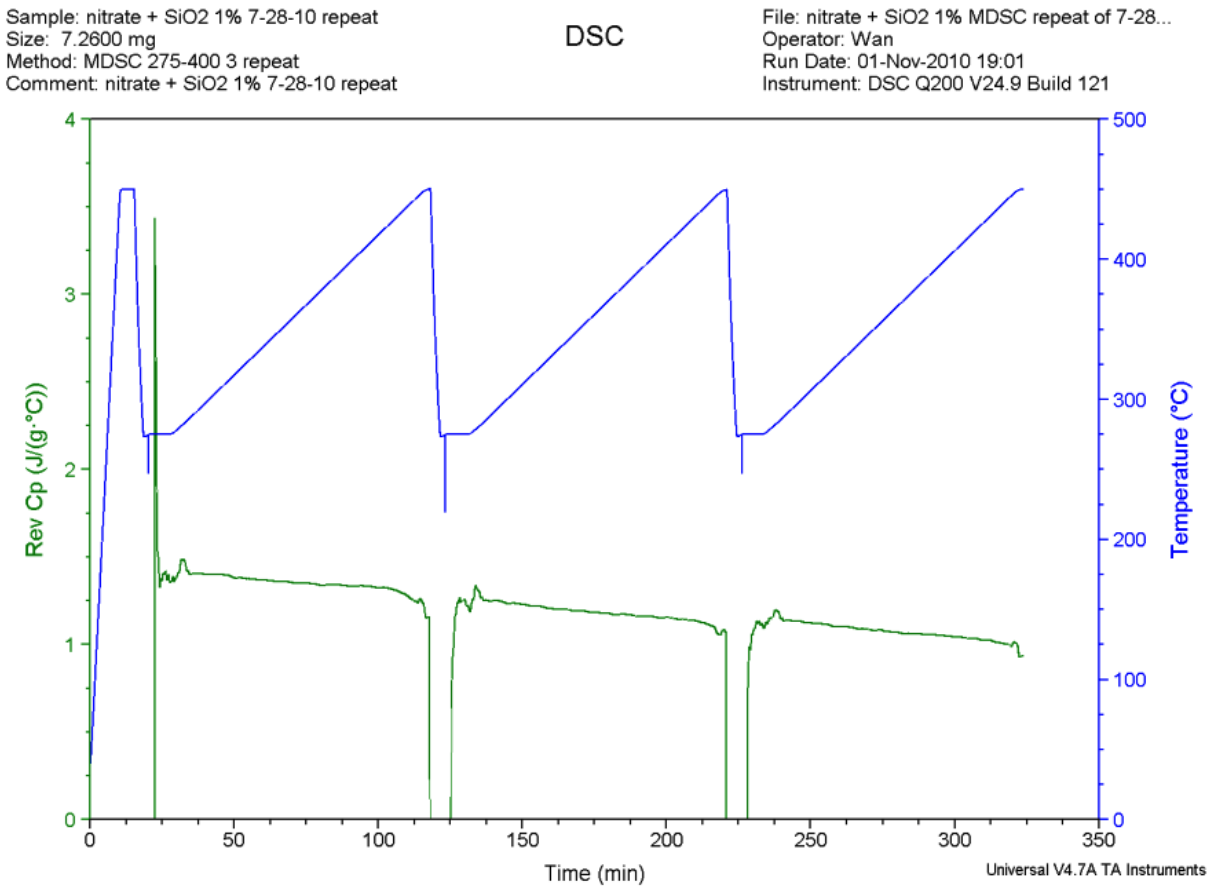

Figure 55: Second Run of Figure 54 Sample using MDSC, Maximum Temperature of 450° C. The specific heat decreases over time, even when the temperature is below 450 C. The upper line is the temperature, and the lower line is the specific heat.

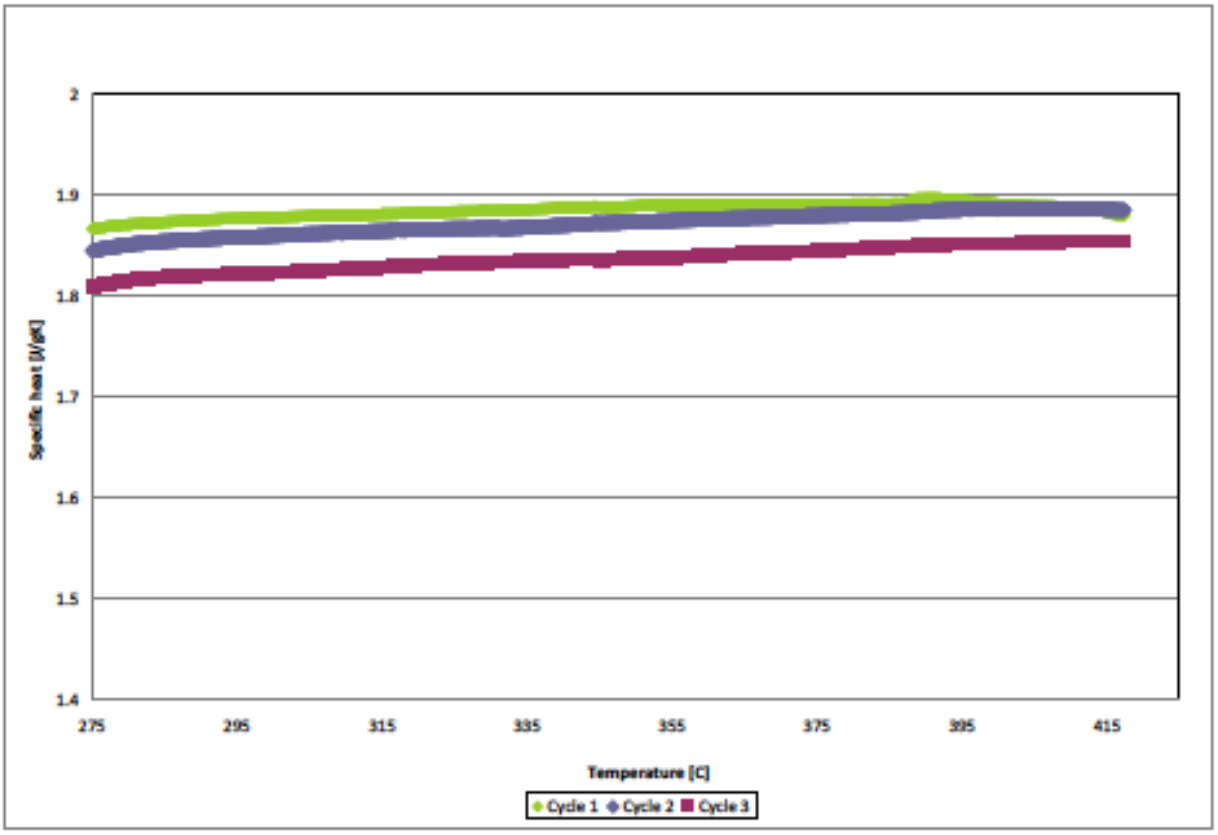

Figure 56: Nitrate and Silica 425° C Maximum Temperature Run, showing a smaller decrease in specific heat when compared to the results shown in Figure 54. Cycle 1 has the highest specific heat, followed by cycle 2 with slightly lower specific heat, and cycle 3 with the lowest specific heat.

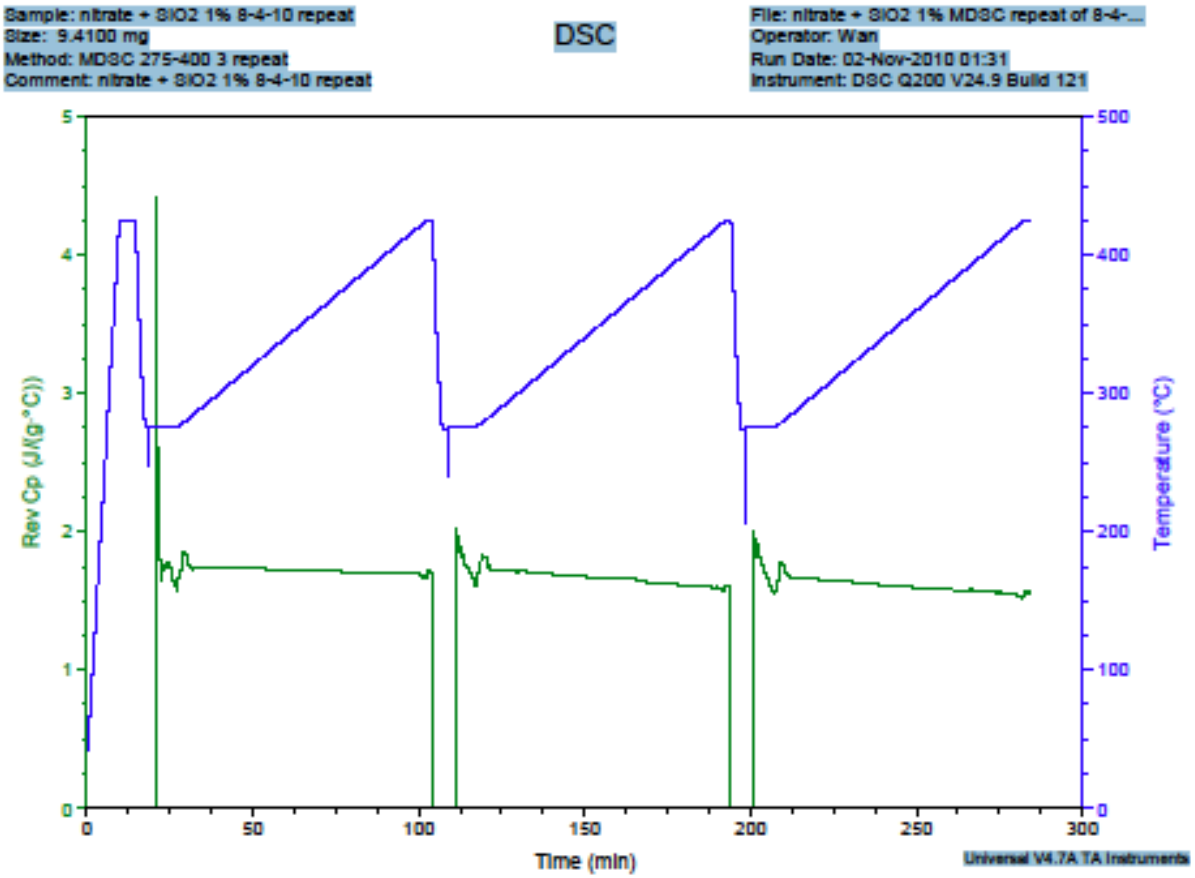

Figure 57: Nitrate + Silica 425° C Maximum Temperature Run using MDSC, second run of the sample from Figure 56. The specific heat decreases over time, even when the temperature is below 425 C. The upper line is the temperature, and the lower line is the specific heat.

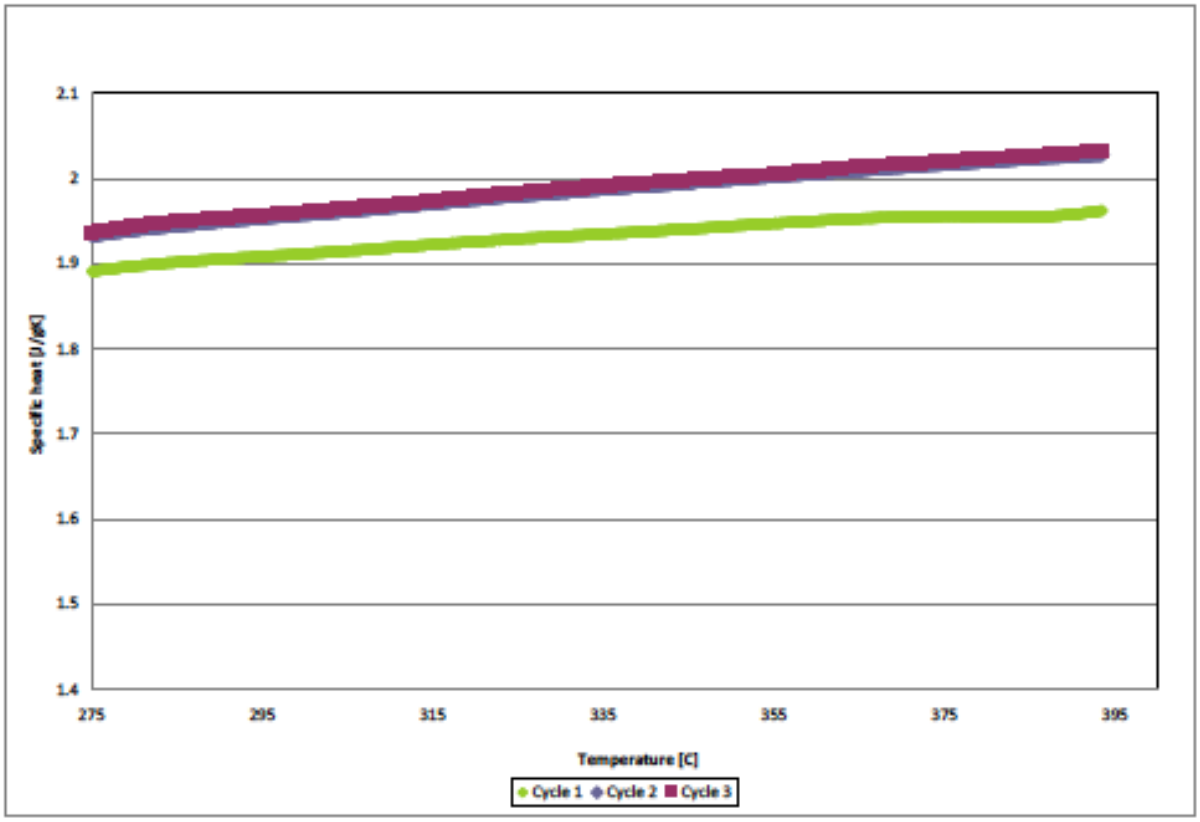

Figure 58: Specific Heat of Nitrate + Silica, Maximum Run Temperature of 400° C. Cycle 1 has the lowest specific heat, but cycle 2 and cycle 3 have nearly the same specific heat, which indicates a stable specific heat.

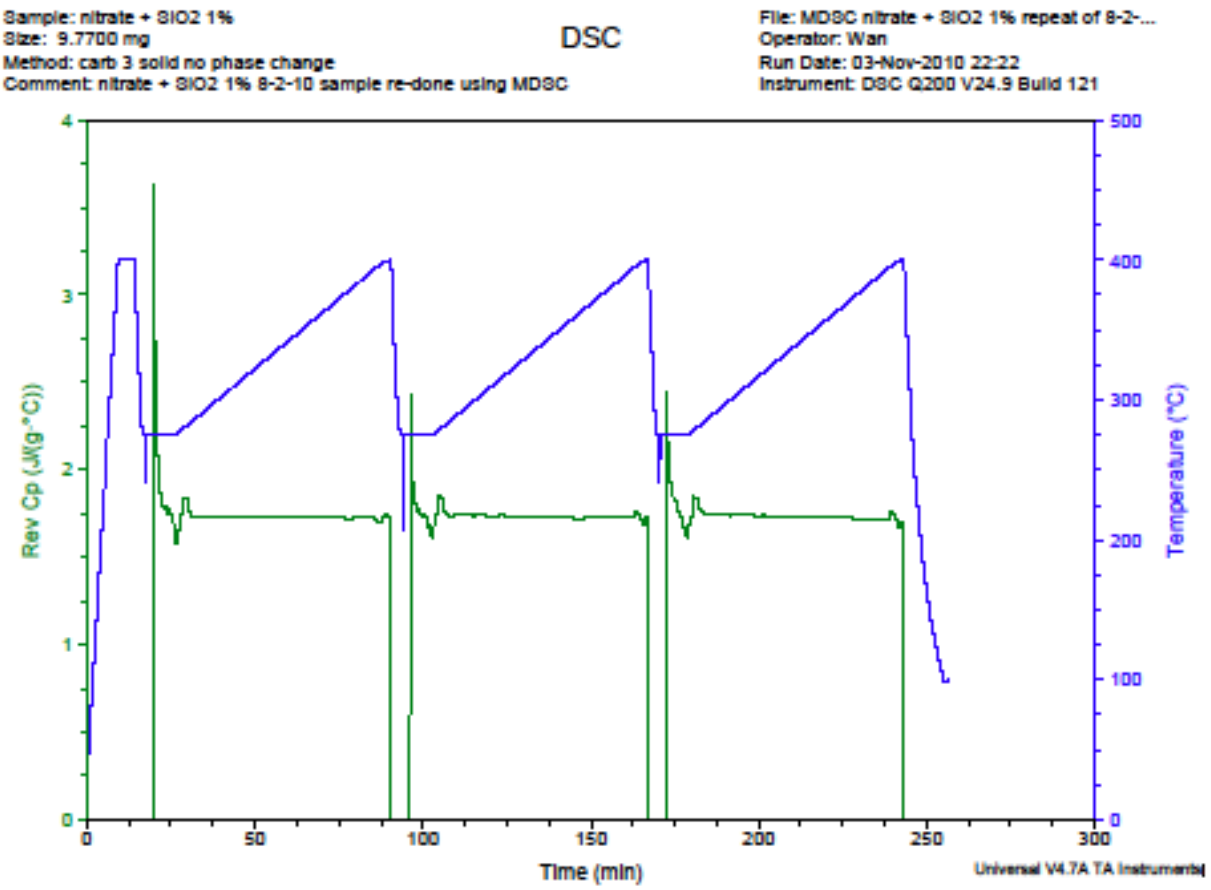

Figure 59: Specific Heat of Nitrate + Silica 400° C Maximum Temperature Run using MDSC, second run of the sample from Figure 58. The specific heat is stable over time, even when at the maximum temperature of the test. The upper line is the temperature, and the lower line is the specific heat.

As can be seen in Figures 54-59, the specific heat changes only when the run temperature goes above 400° C. For all runs, the maximum temperature given was the maximum temperature of all ramp segments in the thermal profile. The change rate also seems to be related to the maximum run temperature, as the change in specific heat is larger at a 450° C maximum run temperature than at a 425° C maximum run temperature. The 400° C maximum temperature run showed no significant change over time. For this reason, the rest of the silica composite runs (as listed in Table 19) were limited to 400° C. In comparison, the nitrate + Al_2O_3 had no such observed behavior and was stable up to 450° C in the runs. The observed maximum temperature of 400° C is a major limitation of the silica composite material, as current trough systems operate between 300° C to 400° C. Future improvements may increase the operational temperature range of trough systems, which would prevent the silica composite from functioning properly in a TES system for a trough CSP plant. Additionally, the current tower systems operate at temperatures up to 600° C, much higher than the 400° C maximum temperature of the stable silica composite. Therefore, the nitrate and silica composite, while useful in current systems, may have limited future utility due to the observed stability issues.

4.1.3.1 Stability of Specific Heat of Nitrate + Alumina Salts of Varying Composition

Samples used in the alumina composition study were stored and retested after 1 and 2 months with the DSC. As shown in Table 20, all compositions of the nitrate + alumina remained stable.

Table 20. Stability results of the specific heat of the nanofluids

$\varphi_{Al_2O_3}$ (%)	Specific Heat (J/gK)		Difference (%)
	Repeat 1	Repeat 2	
0	1.58	1.60	1.35
0.09	1.68	1.68	-0.10
0.17	1.70	1.68	-1.27
0.30	1.90	1.89	-0.77
0.53	1.75	1.69	-3.54
0.78	1.74	1.73	-0.82
0.96	1.76	1.70	-3.22
1.19	1.70	1.68	-1.08

4.1.4 Extended thermal cycling stability

An alumina-nitrate eutectic salt mixture was cycled in separate containers for up to 16 weeks as described in Section 3. The samples were removed from the furnace at the end of the fixed number of hours when the desired numbers of thermal cycles had been completed. The samples were then measured to determine the alumina concentration through different thermal cycles.

Table 21 summarizes the cycling time for each sample. The total time for a single thermal cycle was 6 hours, as was the time for the "zero thermal cycle" batch. We also made a reference run of pure nitrate for 6 hours and a duplicate run of nitrate with alumina for 224 thermal cycles.

Table 21 Sample batches and respective cycle time

Sample batch	Materials	Time length	Time loaded	Time taken out
A	Plain	6hr	4/20/2011	4/20/2011
B	Alumina	6hr	4/20/2011	4/20/2011
C	Alumina	2weeks	4/22/2011 4:00pm	5/6/2011 4:00pm
D	Alumina	4weeks		5/20/2011 4:00pm
E*	Alumina	8weeks		6/17/2011 4:00pm
F	Alumina	12weeks		7/15/2011 4:00pm
G	Alumina	16weeks		8/12/2011 4:00pm
E	Alumina	8 weeks duplicate run	6/17/2011 4:00pm	8/12/2011 4:00pm

4.1.4.1 Specific heat of different thermal cycles

1) Batch A-plain nitrate-6hr cycle
   This cycle served as the reference cycle.

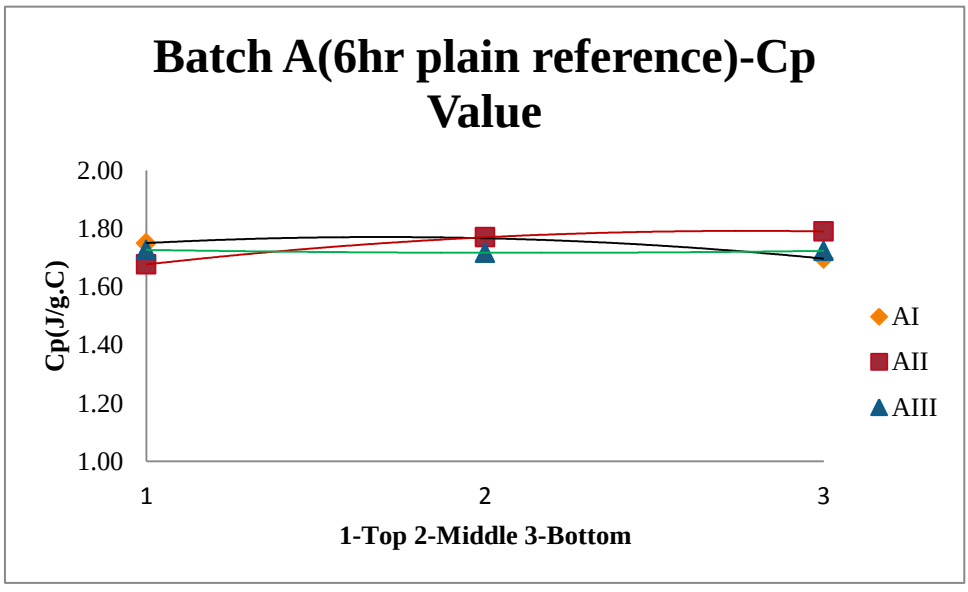

Figure 60: C_p value for Batch A (6hr cycle-Refernce)

2) Batch B-alumina+nitrate-6hr cycle

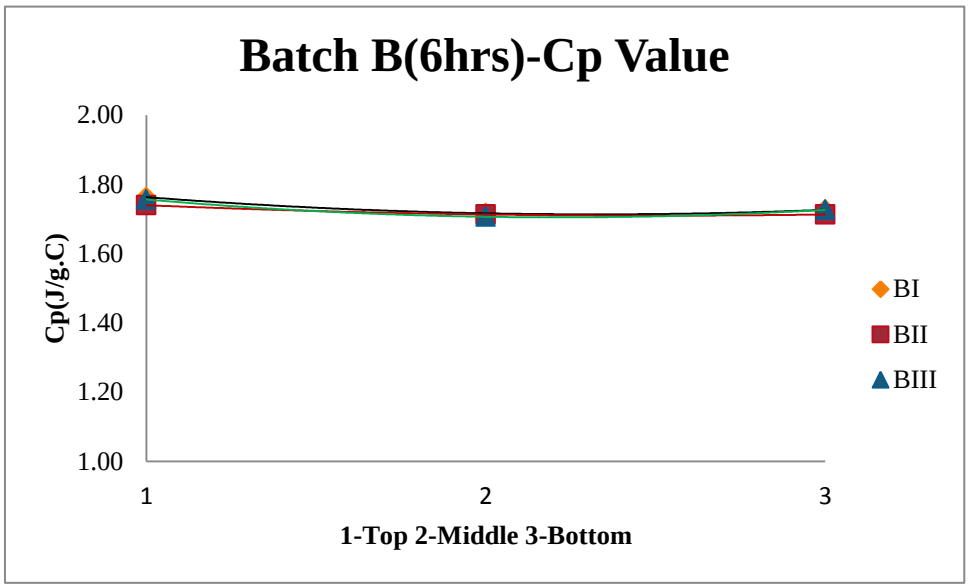

Figure 61: C_p value for Batch B (6hr cycle)

Figure 61 shows the C_p values from the three samples are in good agreement, giving confidence for the reliability of the method.

3) Batch C-alumina+nitrate-2weeks cycle

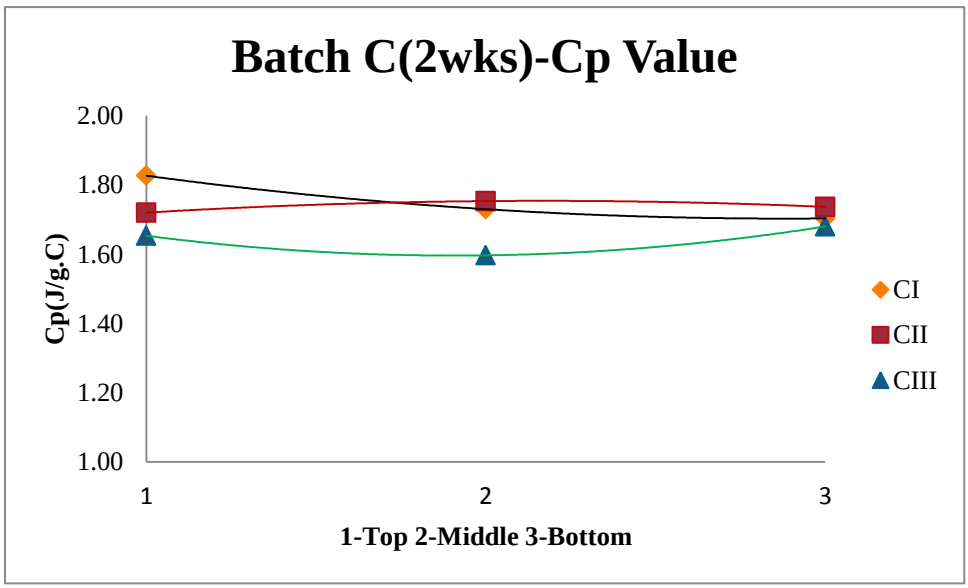

Figure 62: C_p value for Batch C (2 weeks cycle)

Figure 62 shows both some spatial and sample-to-sample variation in the measured C_p after 2 weeks of thermal cycling.

4) Batch D- alumina+nitrate-4weeks cycle

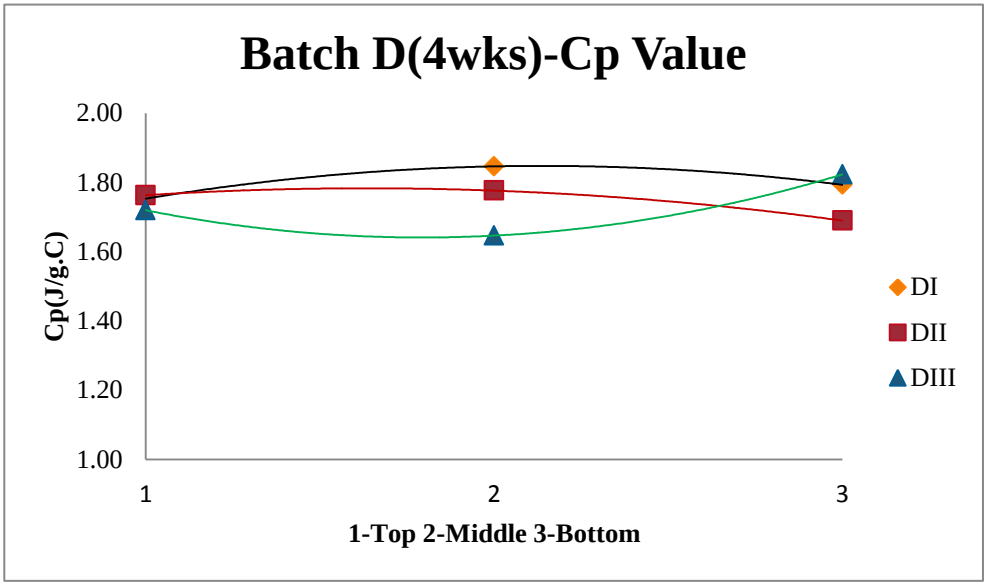

Figure 63: Cp value for Batch D (4 weeks cycle)

5) Batch F- alumina+nitrate-12 weeks cycle

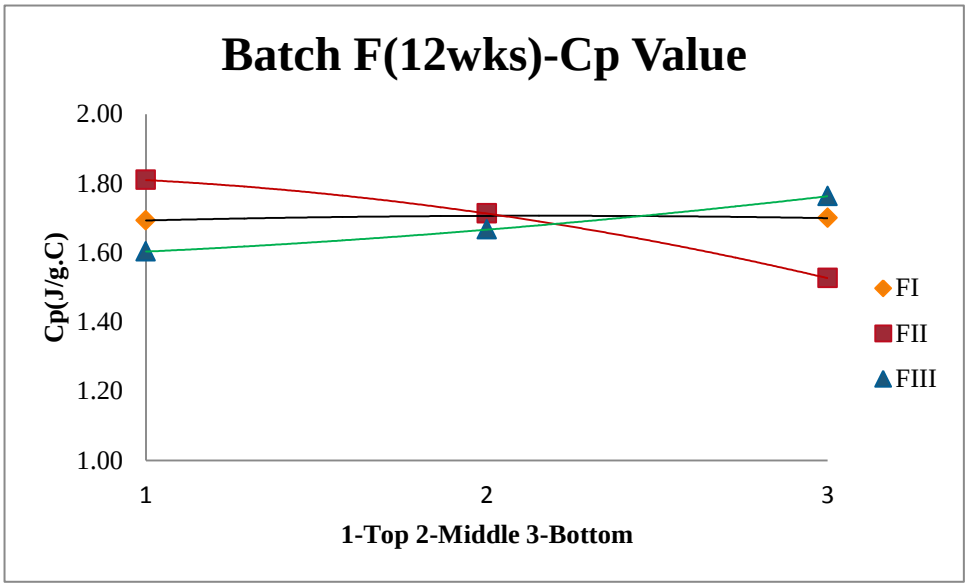

Figure 64: Cp value for Batch F (12 weeks cycle)

4.1.4.2 Overall change of Cp value through different time span

The overall trend of the change of Cp value was obtained by averaging all the Cp values for each section (top, middle, bottom) from all the MDSC runs with the same time of thermal cycling (3specimen × 3 runs/specimen =9 results) .

Figure 65 shows the change in Cp values with time, based on data from 6hr, 2wks, 4wks, and 12wks.

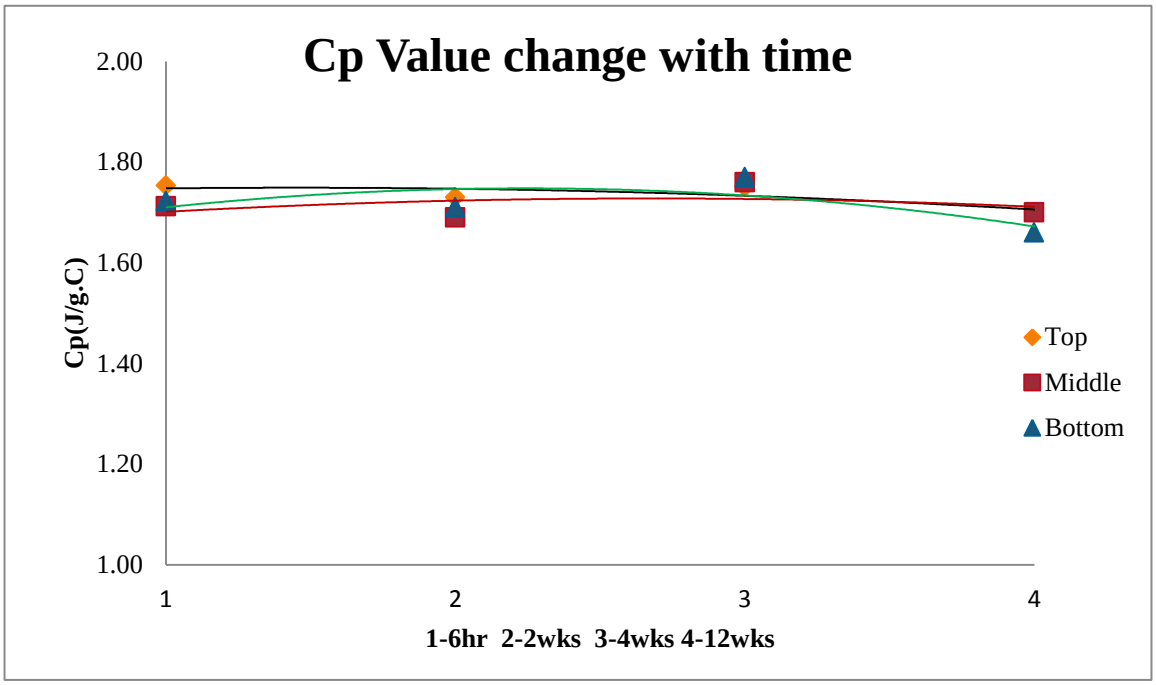

Figure 65: Overall change of Cp value with time

Figure 65 shows the specific value Cp does not vary much over the 12 week period. Thus far, the composite of alumina nanoparticles and nitrate salt seems stabile to thermal cycling. Further proof will be needed to support this observation.

4.1.5 Alumina-Nitrate Nanofluids from Air Dryer Method.

Nanofluids with nominal Al_2O_3 nanoparticle mass fractions of 0.0625%, 0.125%, 0.25% and 0.5% were synthesized using the air dryer method. The specific heat, melting point and heat of fusion were measured using the DSC.

4.1.5.1 DSC Results.

Specific Heat.

The same measurement techniques were used for the material produced in the air dryer as for the material produced by evaporation: the specific heat of all the nanofluids was measured for three repeats. The specific heats (C_p) of each nanofluid at 350 ^oC are shown in Table 22.

Table 22: The specific heat of the nanofluids at 350 ^{o}C from DSC

$\varphi'_{Al_2O_3}$ (%)	Average Specific Heat (J/gK)	STDEV	Coefficient of Variation (%)
0.0625	2.07	0.085	4.1
0.125	1.92	0.008	0.4
0.25	1.93	0.021	1.1
0.5	2.04	0.052	2.6

As shown in table 22, the specific heats of the nanofluids are very high, up to 2.07 J/gK at 0.0625% mass fraction of alumina nanoparticles. However, the difference between the specific heats among all the nanofluids was not very large. The largest difference of the specific heat among them is 8%.

Heat of fusion and Melting Point.

Table 23 presents heat of fusion and melting point results for the nanofluids tested by DSC (40^{o}C/min ramp rate). As shown in the table, there is no large difference among them. The coefficient of variation of heat of fusion is 6% and melting point only 0.3%.

Table 23: Heat of fusion and melting point of the nanofluids from DSC

$\varphi_{Al_2O_3}$ (%)	Heat of Fusion (J/g)	Melting Point (^{o}C)
0.0625	130.2	217.5
0.125	130.9	219.0
0.25	121.6	219.2
0.5	126.7	217.6

Stability of Specific Heat.

After 1 month in storage at room temperature, the same samples were tested again by using DSC. The results are shown in Table 24. The coefficient of variation of DSC runs for each mass fraction samples is within 8.2%, indicating no effect on the specific heat due to storage.

Table 24: Stability results of the specific heat of the nanofluids

$\varphi_{Al_2O_3}$ (%)	Repeated Specific Heat (J/gK)	STDEV	Coefficient of Variation (%)
0.0625	1.88	0.15	8.16
0.125	1.97	0.05	0.03
0.25	1.83	0.08	4.29
0.50	2.09	0.12	5.80

4.1.6 Thermal Conductivity and Thermal Diffusivity.

The thermal diffusivities and thermal conductivities of the nanofluid were measured at temperatures of 65° C, 85° C, 105° C, 125° C and 145° C by using Laser Flash Analysis. For each nanofluid, three samples were used. Figure 66 shows the average thermal diffusivities and the average thermal conductivities of plain nitrate. From the figure, we know that the thermal diffusivities and the thermal conductivities of plain nitrate decrease with the increasing temperature.

A polynomial fitting curve for the thermal conductivities k of plain nitrate at temperatures of 65°C to 145°C is shown in the Eq. (23).

$$k = 1.044 - 0.002T - 2.338 \times 10^{-5} T^2 + 1.042 \times 10^{-7} T^3 \qquad (23)$$

By using this equation, the thermal conductivity of plain nitrate at 222°C, is calculated to be about 0.563 W/mK. Compared with the literature value of 0.536 W/mK [41], it is within 5% difference. Therefore, the thermal conductivities from LFA are reasonably reliable.

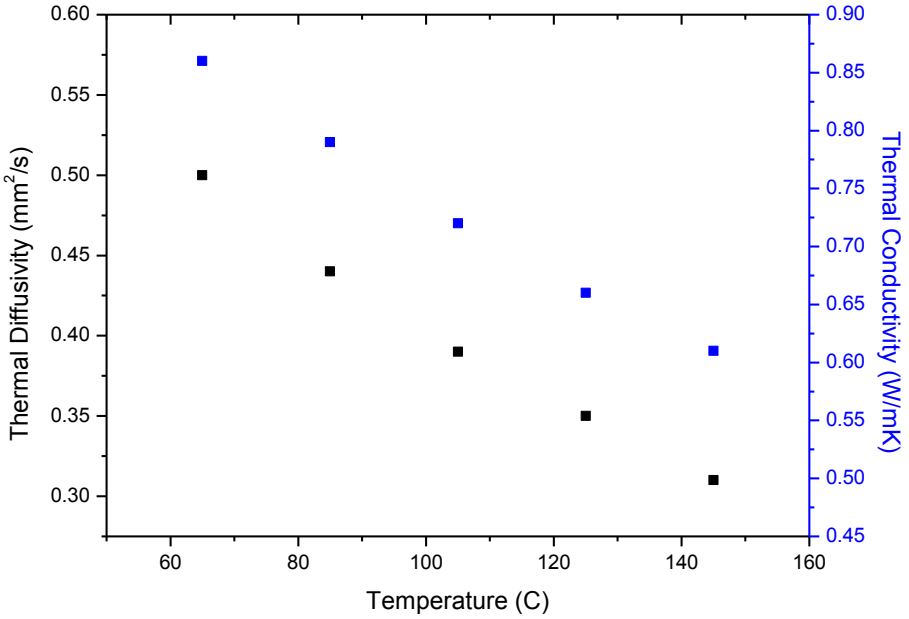

Figure 66. Thermal diffusivity and thermal conductivity of plain nitrate

Table 25 presents the thermal diffusivities and the thermal conductivities of the nanofluids at 145^{o} C, respectively. It can be found that plain nitrate has the highest thermal diffusivity and thermal conductivity at 145^{o} C compared with other nanofluids, about 0.31 mm^{2}/s and 0.61 W/mK. The coefficients of variation of them are within 7.5%, which demonstrates a set of reliable experimental results.

Table 25.Thermal diffusivities and thermal conductivities of the nanofluids at 150 ^{o}C

$\varphi'_{Al_2O_3}$ (%)	Thermal Diffusivity (mm^2/s)	STDEV 1	Thermal Conductivity (W/mK)	STDEV 2	Coefficient of Variation (%)
0	0.31	0.012	0.61	0.022	3.7
0.09	0.26	0.019	0.46	0.034	7.3
0.17	0.30	0.021	0.53	0.037	6.9
0.30	0.24	0.006	0.44	0.011	2.5
0.53	0.24	0.005	0.46	0.009	1.9
0.78	0.26	0.013	0.52	0.025	4.8
1.19	0.26	0.012	0.46	0.022	4.8

4.2. Carbonate Eutectic Salt

4.2.1 Specific heat of the plain carbonate

The specific heat of the plain carbonate eutectic (without any nanoparticles) was measured. The specific heat of the plain material is measured by following the same MDSC temperature profile that was used for the enhanced samples.

The plot of the measured value compared to the calculated values obtained using equation [24] is shown in Figure 67.

$C_p = 0.562 + 1.16 * 10^{-3} * T$ kJ.kg^{-1}.K at $365 < T < 631$K [24]

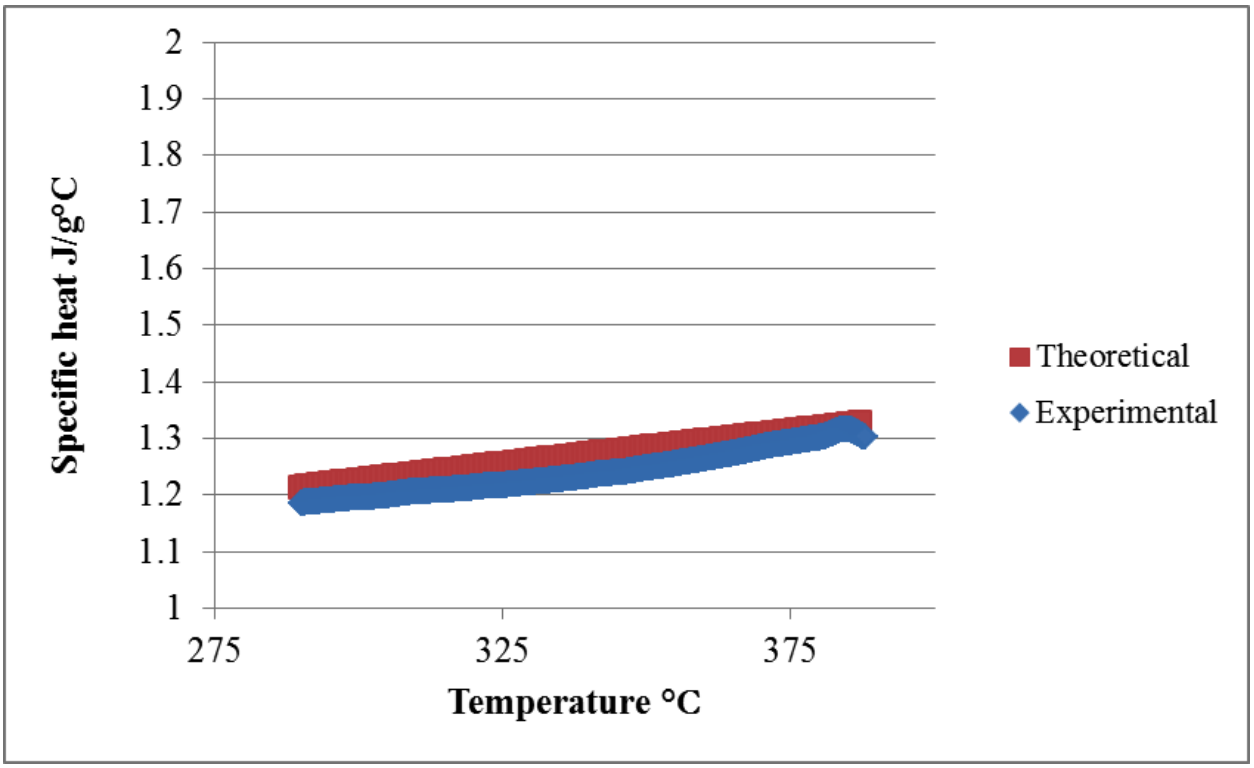

Figure 67: Comparison between specific heat of plain carbonate measured using the MDSC method and the calculated values

4.2 2 Thermal Cycling Stability of Carbonate + Alumina

4.2.2.1 Concentration of Alumina in the Mixture Before Thermal Cycling

Table 26 shows the mass percentage of alumina present in each of the 6 batches of the original uncycled material, measured using neutron activation analysis. The average mass percentage of the nanoparticles in the starting material is 0.96% with a standard deviation of 0.13%. 35

Table 26 : Concentration of alumina in the uncycled material

Batch	Alumina %	Std Dev
Batch 1	0.91	0.02
Batch 2	0.92	0.08
Batch 3	0.85	0.02
Batch 4	0.99	0.03
Batch 5	1.22	0.11
Batch 6	0.89	0.11

4.2.2.2 Specific Heat of the Carbonate + Alumina Before Thermal Cycling

The specific heat of the original material is measured using the MDSC method, following the

temperature profile described in the experimental procedure section. A typical MDSC run result is shown in Figure 68. The observed value of the specific heat of the original uncycled material is given in Table 27. The average specific heat is 1.38 J/g°C with a standard deviation of 0.15 J/g°C. The properties of the original uncycled material are the reference values to which the properties post-thermal cycling are compared. Therefore it is important to establish these values in the beginning.

Table 27 : Average specific heat of material in each batch of original uncycled material

Average Specific heat (J/g°C)		
Sample	**Average**	**Std Dev**
Batch 1	1.60	0.53
Batch 2	1.32	0.12
Batch 3	1.20	0.17
Batch 4	1.23	0.24
Batch 5	1.31	0.21
Batch 6	1.53	0.29

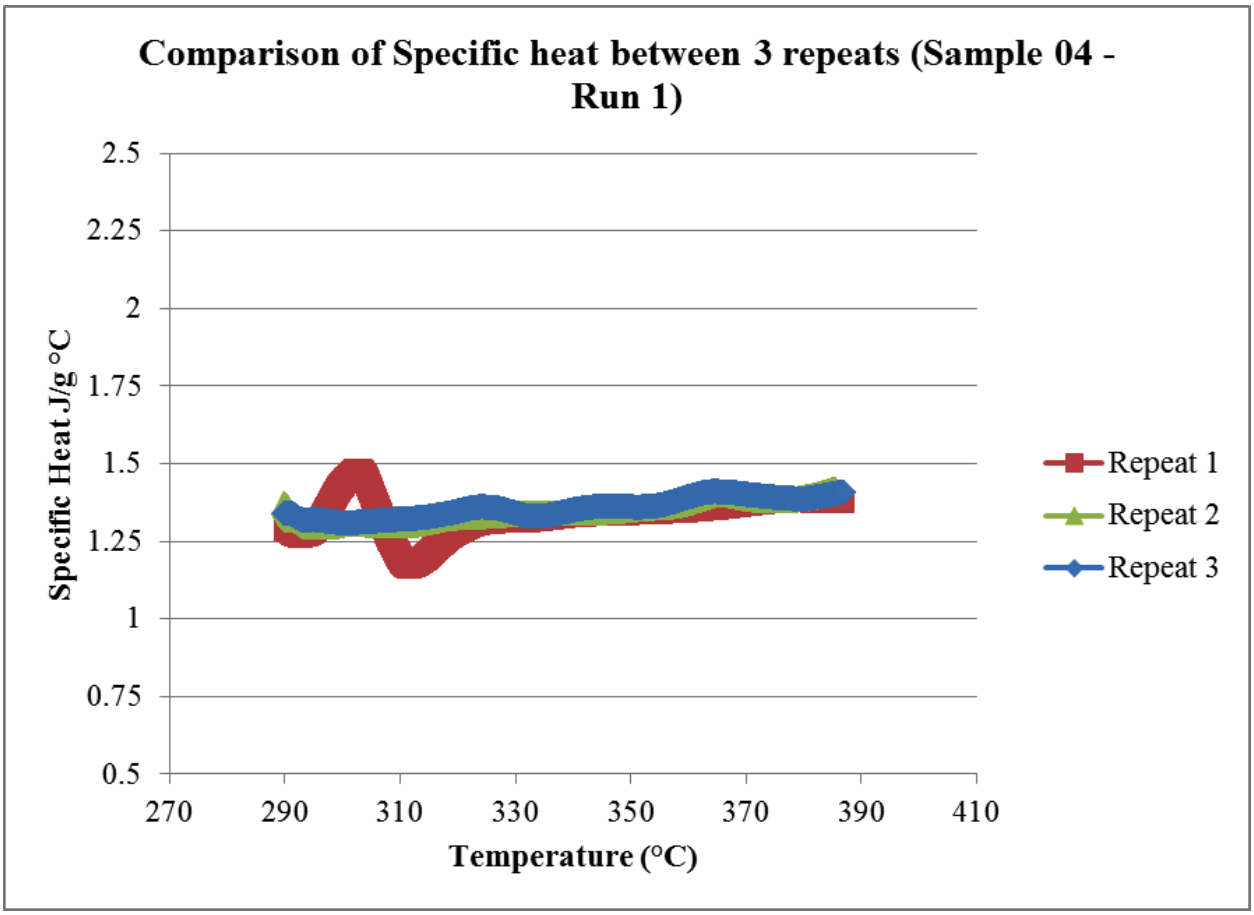

Figure 68: Results of a typical MDSC run showing the 3 repeats

4.2.2.3 Properties of Material Post - Thermal Cycling

The materials undergo thermal cycling in a temperature-controlled furnace. The temperature profile and the process in which the thermal cycling is carried out are described in section 3. Each batch of thermally cycled material has 3 sample tubes and each sample tube is sectioned into 3 parts – to, middle and bottom. Specimen material taken from each of the sections is tested using neutron activation and DSC runs. The average values measured by subjecting 3 specimens to each test is presented next.

4.2.2.3.1 Stability of Nano composite with thermal cycling

The mass percentage of alumina is measured in the material taken from the central portion of the section and also from the portion near the wall of each section. The average mass percentage of alumina in the central portion of each section is listed in Table 28. The mean and standard deviation of the concentration of alumina in each section is also given. The batch number in the parentheses indicates the source of the starting material of each sample.

Table 29 shows the mass percentage of alumina in the material taken from the portion near the wall in each section. (Not enough material could be recovered near the wall from the top section of Sample 7, so that place in the table has been left blank.) The values given are the average percentage of alumina by mass in each section.

Table 28: Mass percentage of alumina in the thermally cycled material (material taken from the central portion of the sections)

No of thermal cycles	Sample	Mass percentage of alumina in the sample					
		Top		Middle		Bottom	
		Average	Std Dev	Average	Std Dev	Average	Std Dev
1	Sample 1 (Batch 1)	0.21	0.15	1.6	0.048	2.04	0.026
	Sample 2 (Batch 1)	0.053	0.0080	1.7	0.038	1.9	0.083
	Sample 3 (Batch 2)	0.026	0.0020	0.24	0.14	2.2	0.15
20	Sample 4 (Batch 2)	0.18	0.11	0.0060	0.0020	0.015	0.0070
	Sample 5 (Batch 3)	0.016	0.0010	0.024	0.0030	0.018	0.0020
	Sample 6 (Batch 3)	0.022	0.0010	0.024	0.0070	0.022	0.0010
40	Sample 7 (Batch 4)	0.012	0.0020	0.0050	0.0010	0.56	0.13
	Sample 8 (Batch 4)	0.030	0.013	0.011	0.0030	0.21	0.065
	Sample 9 (Batch 5)	0.028	0.018	0.016	0.0020	0.016	0.0010
60	Sample 10 (Batch 5)	0.0090	0.0040	0.016	0.0010	0.026	0.0020
	Sample 11 (Batch 6)	0.010	0.0020	0.0040	0.0010	0.053	0.043
	Sample 12 (Batch 6)	0.023	0.015	0.016	0.0010	0.069	0.027

Table 29: Mass percentage of alumina in the thermally cycled material (material taken from near the wall of the sections)

No of thermal cycles	Sample	Mass percentage of alumina in the sample near wall					
		Top		Middle		Bottom	
		Average	Std Dev	Average	Std Dev	Average	Std Dev
1	Sample 1 (Batch 1)	0.44	0.019	0.59	0.36	0.39	0.24
	Sample 2 (Batch 1)	0.21	0.049	0.96	0.038	1.3	0.098
	Sample 3 (Batch 2)	0.030	0.0040	0.13	0.010	1.6	0.20
20	Sample 4 (Batch 2)	0.031	0.0040	0.0070	0.0020	0.96	0.47
	Sample 5 (Batch 3)	0.051	0.026	0.015	0.0040	0.49	0.20
	Sample 6 (Batch 3)	0.019	0.020	0.0090	0.0010	0.18	0.16
40	Sample 7 (Batch 4)	NA	NA	0.11	0.0050	2.7	0.73
	Sample 8 (Batch 4)	0.32	0.18	0.061	0.0050	3.7	0.27
	Sample 9 (Batch 5)	0.27	0.15	0.64	0.37	4.7	0.32
60	Sample 10 (Batch 5)	0.98	0.21	0.021	0.0080	0.29	0.044
	Sample 11 (Batch 6)	1.3	0.62	0.024	0.0070	0.27	0.019
	Sample 12 (Batch 6)	0.018	0.0030	0.011	0.0010	0.89	0.54

The mass percentage in the central portion is compared to the average concentration of alumina in the original uncycled material, which is 0.96%. These ratios are shown in Table 30, with the log averaged values in Table 31. Similar values, but for samples taken near the cylinder walls, are tabulated in Table 32, with the log averaged values shown in Table 33. The relative mass percentage of alumina in the material taken from the portion near the wall section to the mass percentage of alumina in the material taken from the central portion of the section is useful for studying the radial distribution and clustering of the nanoparticles. These ratios are shown in Table 34.

Table 30: Mass percentage of alumina in the thermally cycled material relative to the mass percentage of alumina in the original uncycled material (material taken from the central portion of the section)

		Relative mass percentage of alumina		
No of thermal cycles	Sample	Top	Middle	Bottom
1	Sample 1 (Batch 1)	0.22	1.6	2.2
	Sample 2 (Batch 1)	0.055	1.7	2.06
	Sample 3 (Batch 2)	0.027	0.25	2.3
20	Sample 4 (Batch 2)	0.18	0.0060	0.016
	Sample 5 (Batch 3)	0.017	0.025	0.019
	Sample 6 (Batch 3)	0.023	0.024	0.023
40	Sample 7 (Batch 4)	0.012	0.0050	0.58
	Sample 8 (Batch 4)	0.031	0.011	0.22
	Sample 9 (Batch 5)	0.029	0.017	0.017
60	Sample 10 (Batch 5)	0.010	0.016	0.027
	Sample 11 (Batch 6)	0.010	0.0040	0.055
	Sample 12 (Batch 6)	0.024	0.016	0.072

Table 31:Log Average of Mass percentage of alumina in the thermally cycled material relative to the mass percentage of alumina in the original uncycled material (material taken from the central portion of the section)

Number of thermal cycles	Log Average of relative percentage of alumina		
	Top	Middle	Bottom
1	0.07	0.88	2.18
20	0.04	0.02	0.02
40	0.03	0.01	0.13
60	0.01	0.01	0.05

Table 32: Mass percentage of alumina in the thermally cycled material relative to the mass percentage of alumina in the original uncycled material (material taken from near the wall of the section)

		Relative mass percentage of alumina		
No of thermal cycles	Sample	Top	Middle	Bottom
1	Sample 1 (Batch 1)	0.46	0.62	0.41
	Sample 2 (Batch 1)	0.22	0.99	1.3
	Sample 3 (Batch 2)	0.031	0.14	1.6
20	Sample 4 (Batch 2)	0.032	0.0070	0.99
	Sample 5 (Batch 3)	0.053	0.015	0.51
	Sample 6 (Batch 3)	0.020	0.010	0.19
40	Sample 7 (Batch 4)	NA	0.12	2.8
	Sample 8 (Batch 4)	0.34	0.063	3.8
	Sample 9 (Batch 5)	0.28	0.67	4.9
60	Sample 10 (Batch 5)	1.02	0.022	0.29
	Sample 11 (Batch 6)	1.3	0.025	0.28
	Sample 12 (Batch 6)	0.019	0.011	0.93

Table 33: Log Average of Mass percentage of alumina in the thermally cycled material relative to the mass percentage of alumina in the original uncycled material (material taken from near the wall of the section)

Number of thermal cycles	Log Average of relative percentage of alumina		
	Top	Middle	Bottom
1	0.15	0.44	0.95
20	0.03	0.01	0.46
40	0.31	0.17	3.74
60	0.29	0.02	0.42

Table 34: Mass percentage of alumina near the wall vs. from the central sections

		Relative mass percentage of alumina		
No of thermal cycles	Sample	Top	Middle	Bottom
1	Sample 1 (Batch 1)	2.09	0.39	0.19
	Sample 2 (Batch 1)	3.9	0.59	0.66
	Sample 3 (Batch 2)	1.2	0.56	0.70
20	Sample 4 (Batch 2)	0.17	1.1	64.0
	Sample 5 (Batch 3)	3.2	0.60	27.0
	Sample 6 (Batch 3)	0.86	0.40	8.3
40	Sample 7 (Batch 4)	NA	22.0	4.9
	Sample 8 (Batch 4)	11.0	5.7	17.0
	Sample 9 (Batch 5)	9.5	39.0	290.0
60	Sample 10 (Batch 5)	105.0	1.4	11.0
	Sample 11 (Batch 6)	134.0	5.9	5.05
	Sample 12 (Batch 6)	0.79	0.68	13.0

4.2.2.3.2 Specific Heat of the Thermally Cycled Material

The average specific heat of the thermally cycled material after each thermal cycle is presented in Tables 35, 36, 37 and 38. The average specific heat in each section of the sample after a specific number of thermal cycles is considered for analysis. The average specific heat is the specific heat taken over the temperature range of 290°C to 397°C.

Table 35: Average specific heat (in J/g°C) of the material in Batch A (1 thermal cycle)

Batch A	**Sample 1**		**Sample 2**		**Sample 3**	
Section	**Average Specific Heat**	**Std Deviation**	**Average Specific Heat**	**Std Deviation**	**Average Specific Heat**	**Std Deviation**
Top	1.95	0.26	1.63	0.039	1.76	0.109
Middle	1.62	0.26	1.77	0.21	1.9	0.078
Bottom	1.80	0.105	1.92	0.091	1.61	0.14

Table 36: Average specific heat (in J/g°C) of the material in Batch B (20 thermal cycles)

Batch B	**Sample 4**		**Sample 5**		**Sample 6**	
Section	**Average Specific Heat**	**Std Deviation**	**Average Specific Heat**	**Std Deviation**	**Average Specific Heat**	**Std Deviation**
Top	2.10	0.075	1.98	0.37	1.92	0.13
Middle	1.9	0.13	1.8	0.25	1.94	0.031
Bottom	1.8	0.099	1.8	0.12	1.9	0.23

Table 37: Average specific heat (in J/g°C) of the material in Batch C (40 thermal cycles)

Batch C	**Sample 7**		**Sample 8**		**Sample 9**	
Section	**Average Specific Heat**	**Std Deviation**	**Average Specific Heat**	**Std Deviation**	**Average Specific Heat**	**Std Deviation**
Top	2.3	0.14	1.9	0.11	1.99	0.087
Middle	1.8	0.31	1.7	0.11	1.9	0.061
Bottom	1.9	0.15	1.85	0.11	2.02	0.089

Table 38: Average specific heat (in J/g°C) of the material in Batch D (60 thermal cycles)

Batch D	**Sample 10**		**Sample 11**		**Sample 12**	
Section	**Average Specific Heat**	**Std Deviation**	**Average Specific Heat**	**Std Deviation**	**Average Specific Heat**	**Std Deviation**
Top	1.95	0.27	1.99	0.16	1.9	0.014
Middle	1.6	0.26	1.88	0.13	1.7	0.063
Bottom	1.8	0.105	1.7	0.059	1.9	0.045

It is useful to compare the specific heat of the thermally cycled material with the specific heat of the uncycled material. This relative value is obtained by dividing the specific heat of the thermally cycled material by the specific heat of the uncycled material from the batch corresponding to the original starting material. Tables 39-42 contains these values.

Table 39: Average specific heat of the material relative to the thermally uncycled material (Batch A – 1 thermal cycle)

Batch A	**Sample 1**		**Sample 2**		**Sample 3**	
Section	**Relative Average Specific Heat**	**Std Deviation**	**Relative Average Specific Heat**	**Std Deviation**	**Relative Average Specific Heat**	**Std Deviation**
Top	1.2	0.26	1.01	0.039	1.3	0.11
Middle	1.007	0.26	1.1	0.21	1.4	0.078
Bottom	1.12	0.105	1.12	0.091	1.22	0.14

Table 40: Average specific heat of the material relative to the thermally uncycled material (Batch B- 20 thermal cycles)

Batch B	Sample 4		Sample 5		Sample 6	
Section	**Relative Average Specific Heat**	**Std Deviation**	**Relative Average Specific Heat**	**Std Deviation**	**Relative Average Specific Heat**	**Std Deviation**
Top	1.59	0.074	1.64	0.37	1.59	0.132
Middle	1.41	0.13	1.47	0.25	1.62	0.031
Bottom	1.37	0.099	1.45	0.11	1.57	0.23

Table 41: Average specific heat of the material relative to the thermally uncycled material (Batch C – 40 thermal cycles)

Batch C	Sample 7		Sample 8		Sample 9	
Section	**Relative Average Specific Heat**	**Std Deviation**	**Relative Average Specific Heat**	**Std Deviation**	**Relative Average Specific Heat**	**Std Deviation**
Top	1.83	0.14	1.57	0.11	1.52	0.087
Middle	1.44	0.31	1.39	0.11	1.45	0.061
Bottom	1.56	0.15	1.49	0.11	1.55	0.089

Table 42: Average specific heat of the material relative to the thermally uncycled material (Batch D – 60 thermal cycles)

Batch D	Sample 10		Sample 11		Sample 12	
Section	**Relative Average Specific Heat**	**Std Deviation**	**Relative Average Specific Heat**	**Std Deviation**	**Relative Average Specific Heat**	**Std Deviation**
Top	1.49	0.26	1.306	0.16	1.22	0.014
Middle	1.24	0.27	1.23	0.13	1.12	0.063
Bottom	1.38	0.105	1.089	0.059	1.24	0.045

4.2.2.3.3 Correlation Between Concentration of Nanoparticles and the Specific Heat of the Nanomaterial

The influence of the concentration of the nanoparticles in the composite material on the specific heat is studied by correlating the specific heat in each section of the sample with the concentration of alumina in that section. The semi log plots of the average specific heat of the sample with the average concentration of alumina in the respective section are shown in Figures 69-72.The semi log plots of the relative average specific heat of the sample (relative to the specific heat of the uncycled material) with the concentration of the alumina is shown in Figures 73-76.

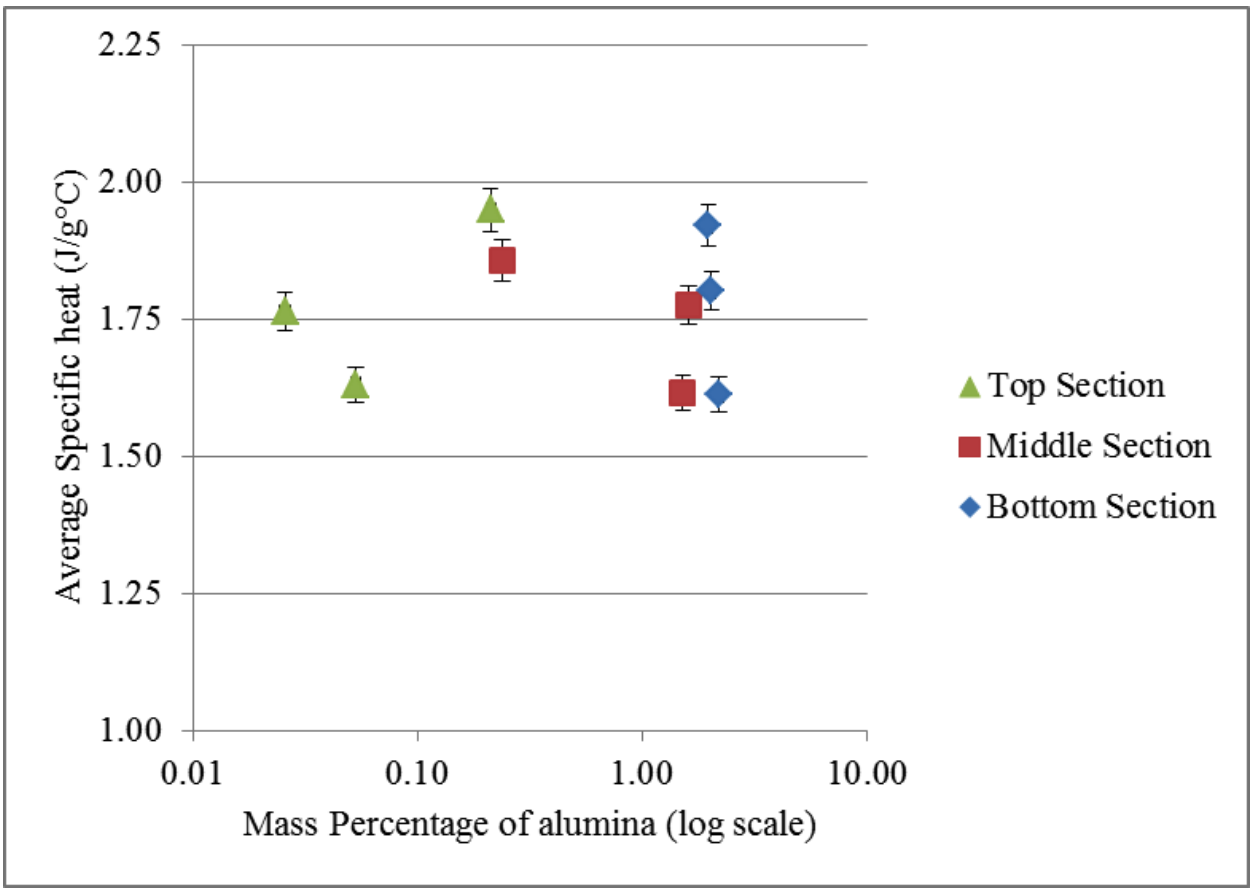

Figure 69: Correlation between the average mass percentage and average specific heat in Batch A (1 thermal cycle)

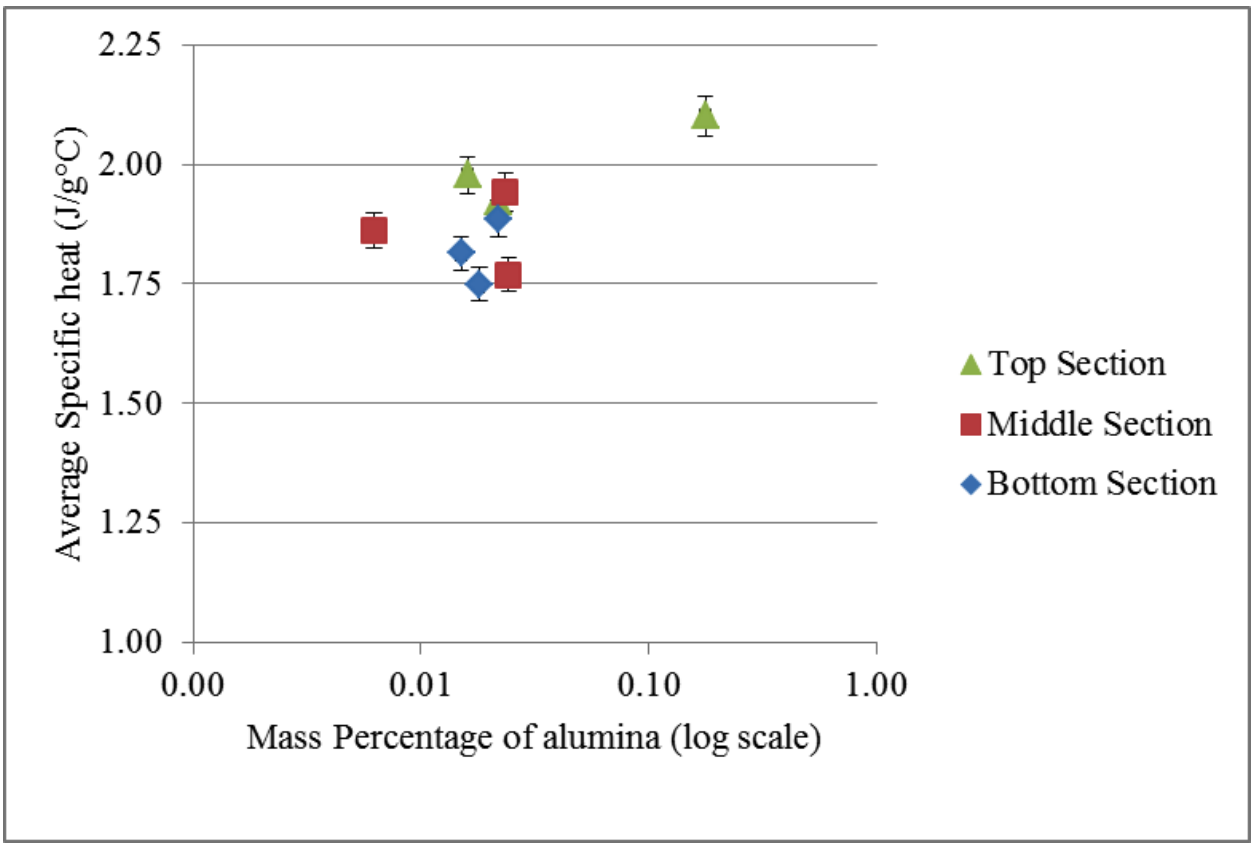

Figure 70: Correlation between the average mass percentage and average specific heat in Batch B (20 thermal cycles)

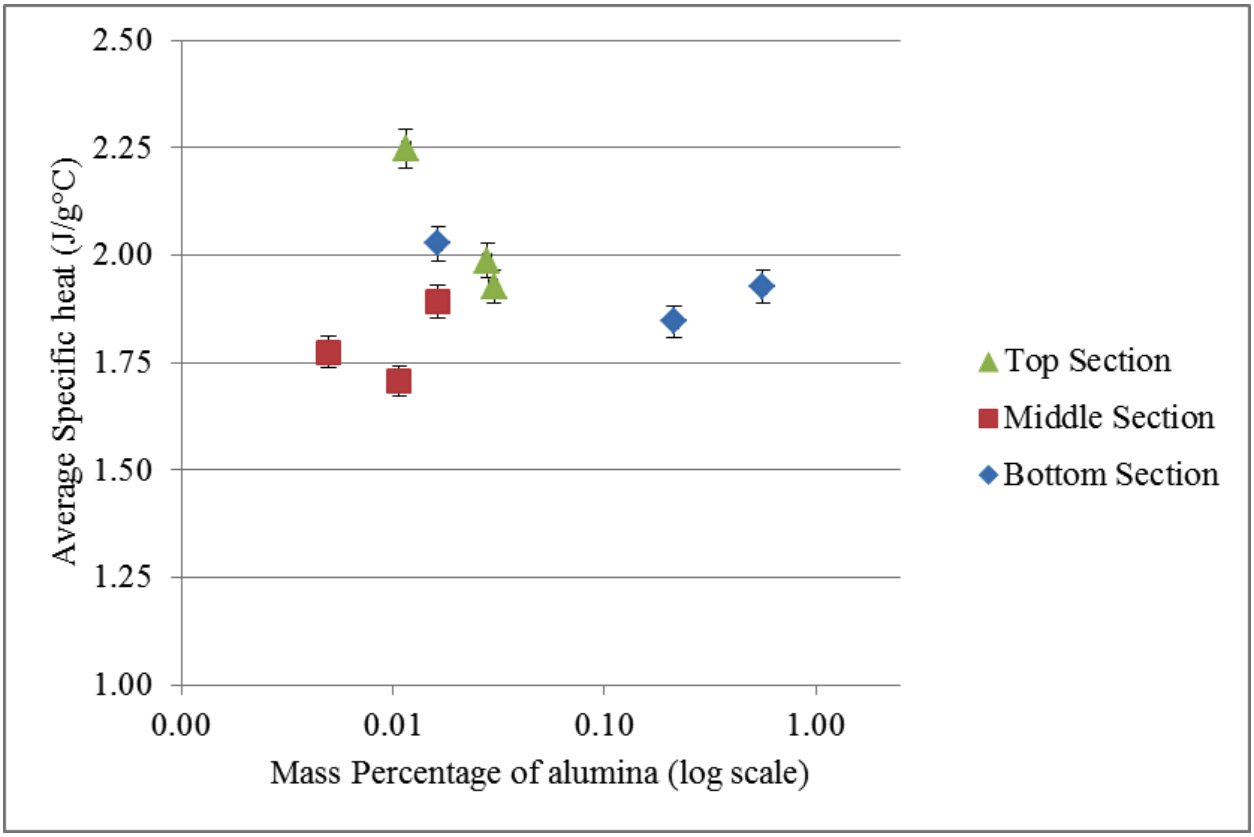

Figure 71: Correlation between the average mass percentage and average specific heat in Batch C (40 thermal cycles)

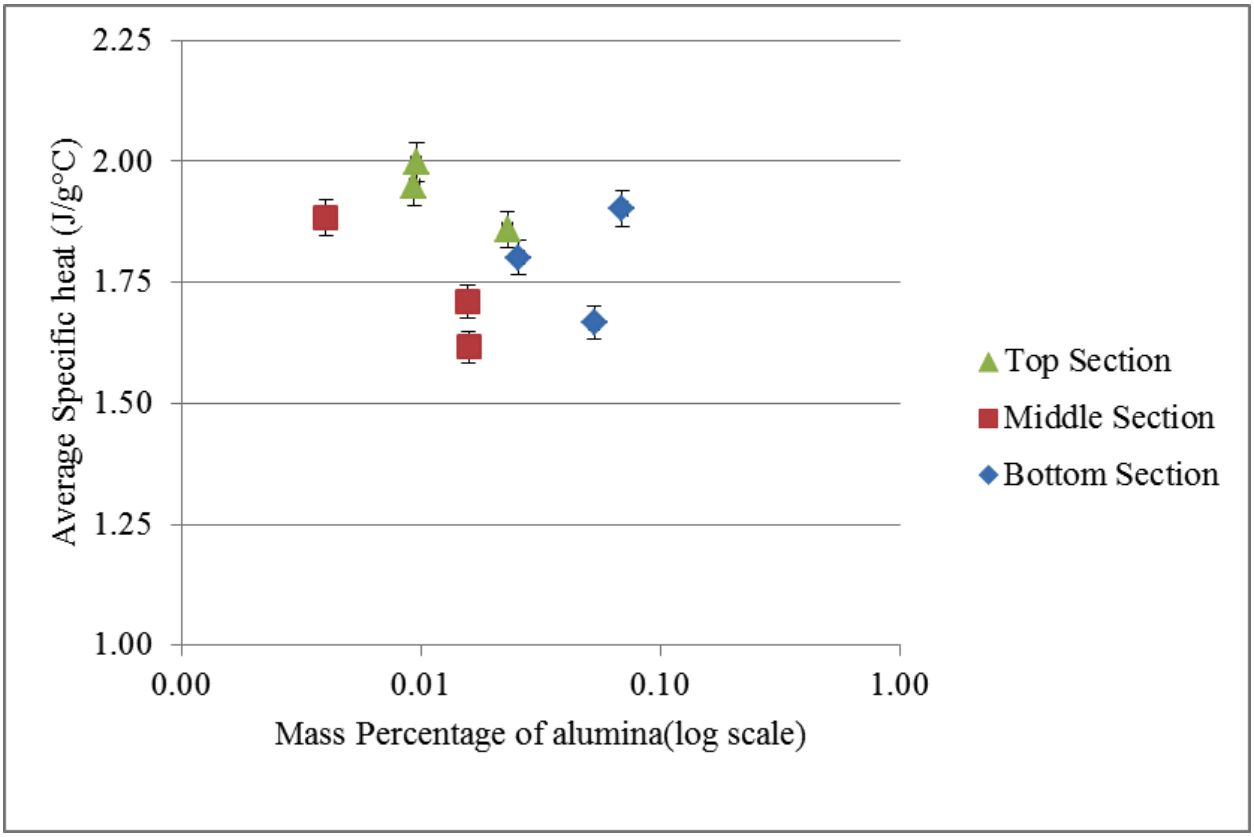

Figure 72: Correlation between the average mass percentage and average specific heat in Batch D (60 thermal cycles)

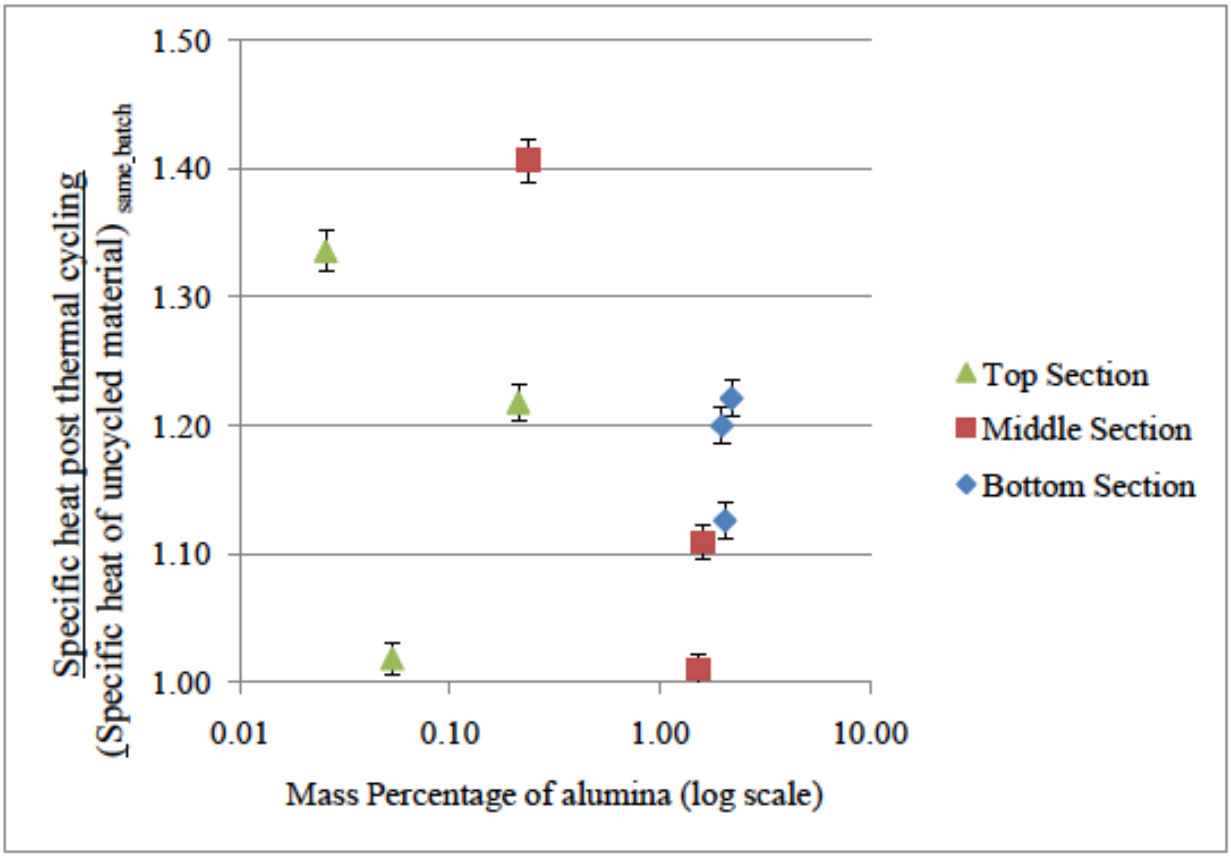

Figure 73: Correlation between the average mass percentage and relative average specific heat in Batch A (1 thermal cycle)

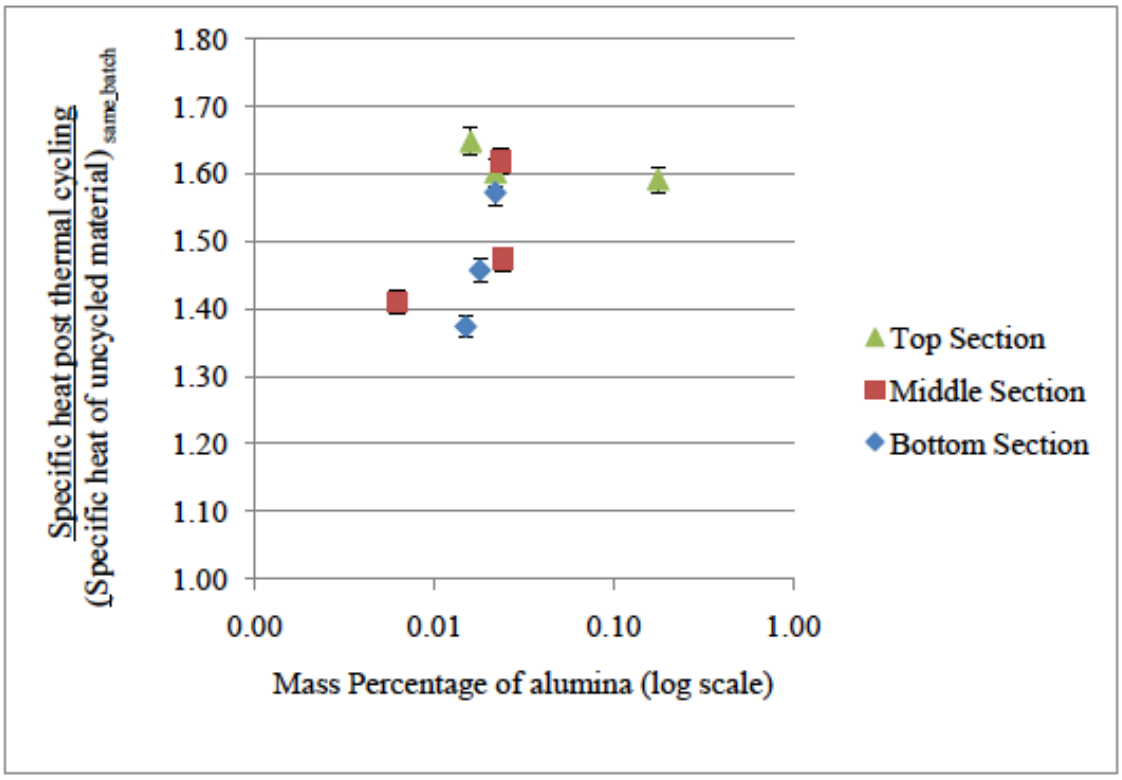

Figure 74: Correlation between the average mass percentage and relative average specific heat in Batch B (20 thermal cycles)

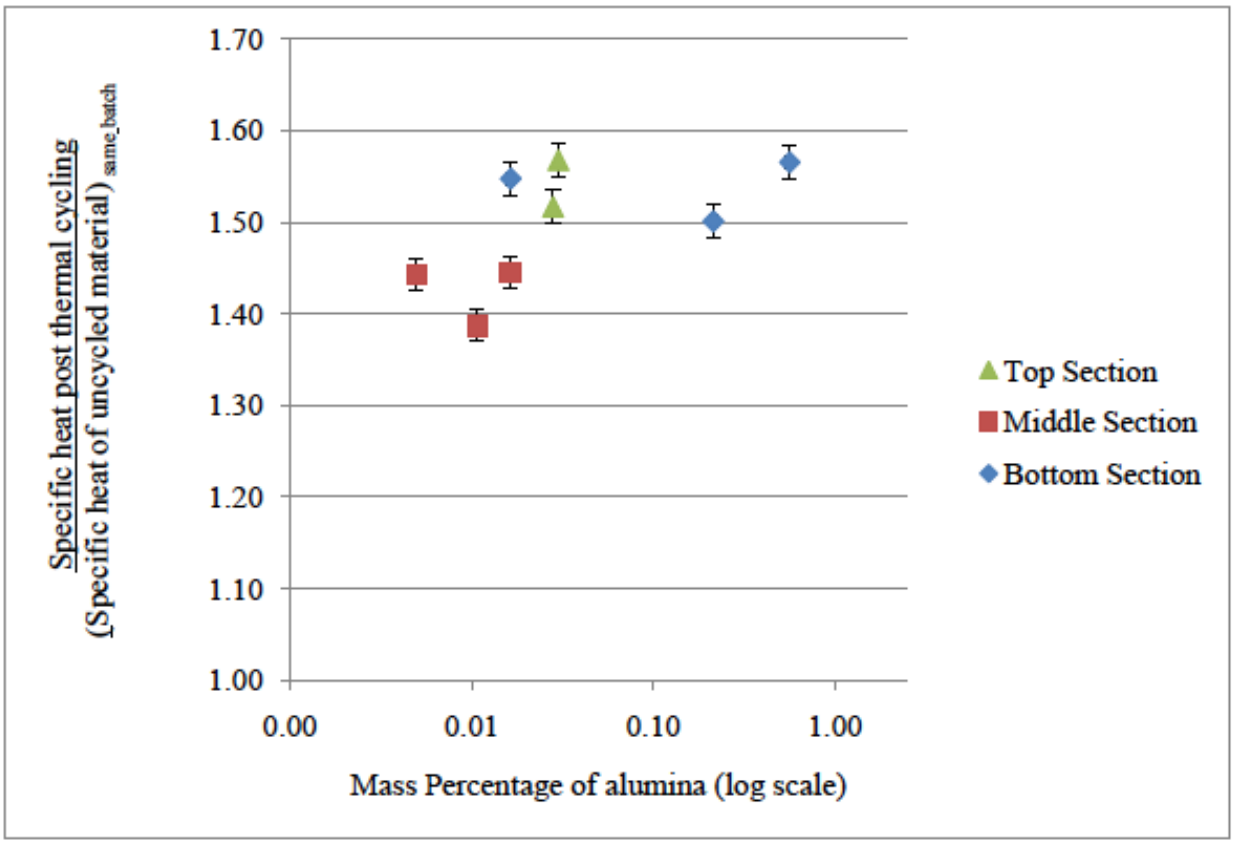

Figure 75: Correlation between the average mass percentage and relative average specific heat in Batch C (40 thermal cycles)

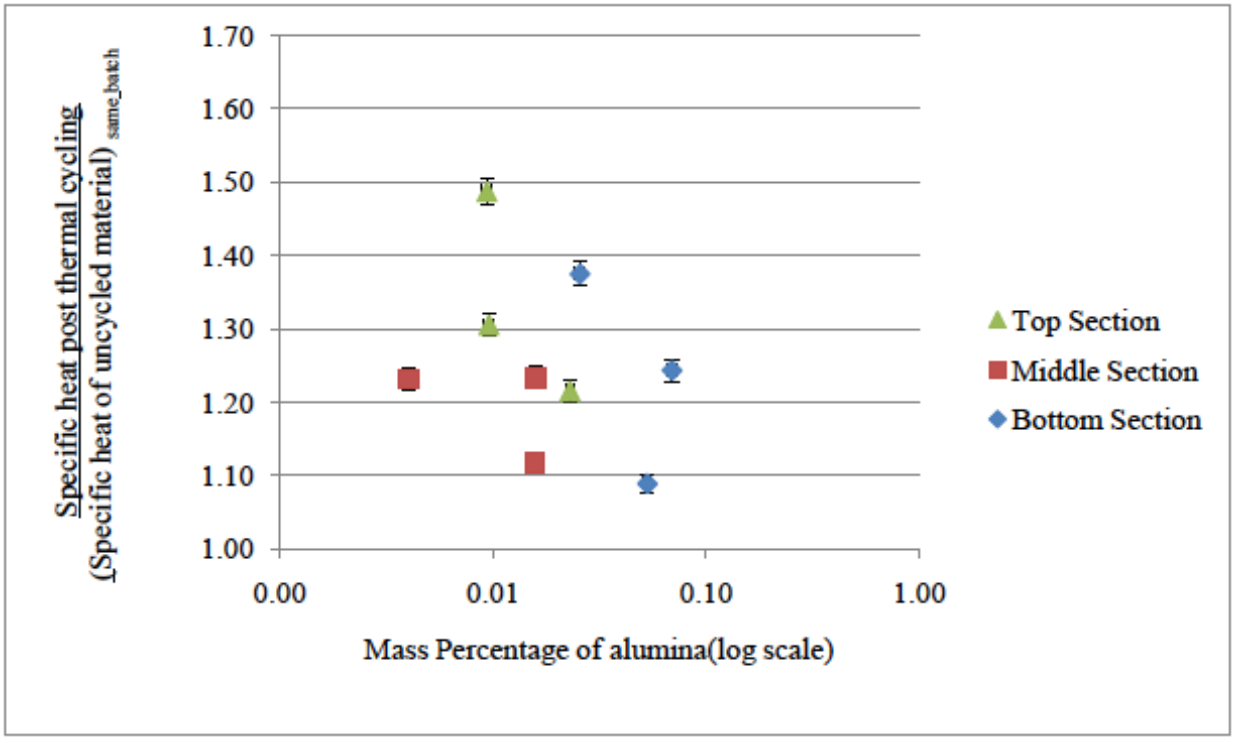

Figure 76: Correlation between the average mass percentage and relative average specific heat in Batch D (60 thermal cycles)

4.3 Corrosion

The mass loss data obtained from the experiments are normalized for surface area and exposure time to obtain the corrosion rate. These rates are then compared (between salts doped with and without silica) and plotted against time.

As discussed earlier, a total of 27 tests samples were tested with three per salt and timeframe. Referring back to the objective, the results and their discussions presented here will be presented with an objective to compare the rate of corrosion of steel with and without silica nanoparticles. The data will be pivoted in different ways to help analyze and verify any findings that supports the initial hypothesis.

The rate of corrosion is given as grams/ cm^2/day and the exposure time in weeks. Each bar is an average of the instantaneous corrosion rates for that particular salt and that exposure time. As explained earlier, there were 3 samples per corroding material and per exposure time. Thus each sample gives an instantaneous corrosion rate. These 3 instantaneous corrosion rates are averaged to determine the average instantaneous corrosion rate. This value is plotted in a bar graph (Figures 77, 78 and 79).

The results also include the total corrosion comparison, wherein the corrosion data is only area normalized. Total corrosion differs from mean instantaneous corrosion rate in the sense that they are only area normalized and not time normalized. Total corrosion refers to the value that is the mean of corrosion rates normalized with respect to only area of the three samples per corroding environment and per exposure time. This comparison was done to compare the observed behavior of the corrosion

with the predicted model for corrosion in ferrous materials.

4.3.1 Plain versus Doped Results

The results below compare the corrosion rate of steel by molten plain and doped carbonate salts at 2,4 and 6 weeks. Each of the corrosion rates are obtained by averaging 3 data points. The uncertainty bars indicate the standard deviation from the mean.

The uncertainty ranges from 7-10%. To establish further confidence in the shift of means due to doping a t test was performed. There is a 95% confidence in the results that the mean has shifted in the direction of reduced corrosion due to doping. This test has been detailed in section 4.3.1.5

4.3.1.1 Comparison of Corrosion Rates between Carbonate and Carbonate Doped with Silica Nanoparticles 1 % by Weight

Figures 77 - 79 show the average corrosion rate by carbonates and carbonates doped with silica. The figure was created by averaging the normalized mass loss rates for each salt type. Figure 77 shows the results for 2 weeks, Figure 78 for 4 weeks, and Figure 79 for 6 weeks.
Figure 77 indicates that due to doping, the corrosion rate has decreased by about 40% in comparison to the corrosion rate without doping. There is 95% confidence level in this result.

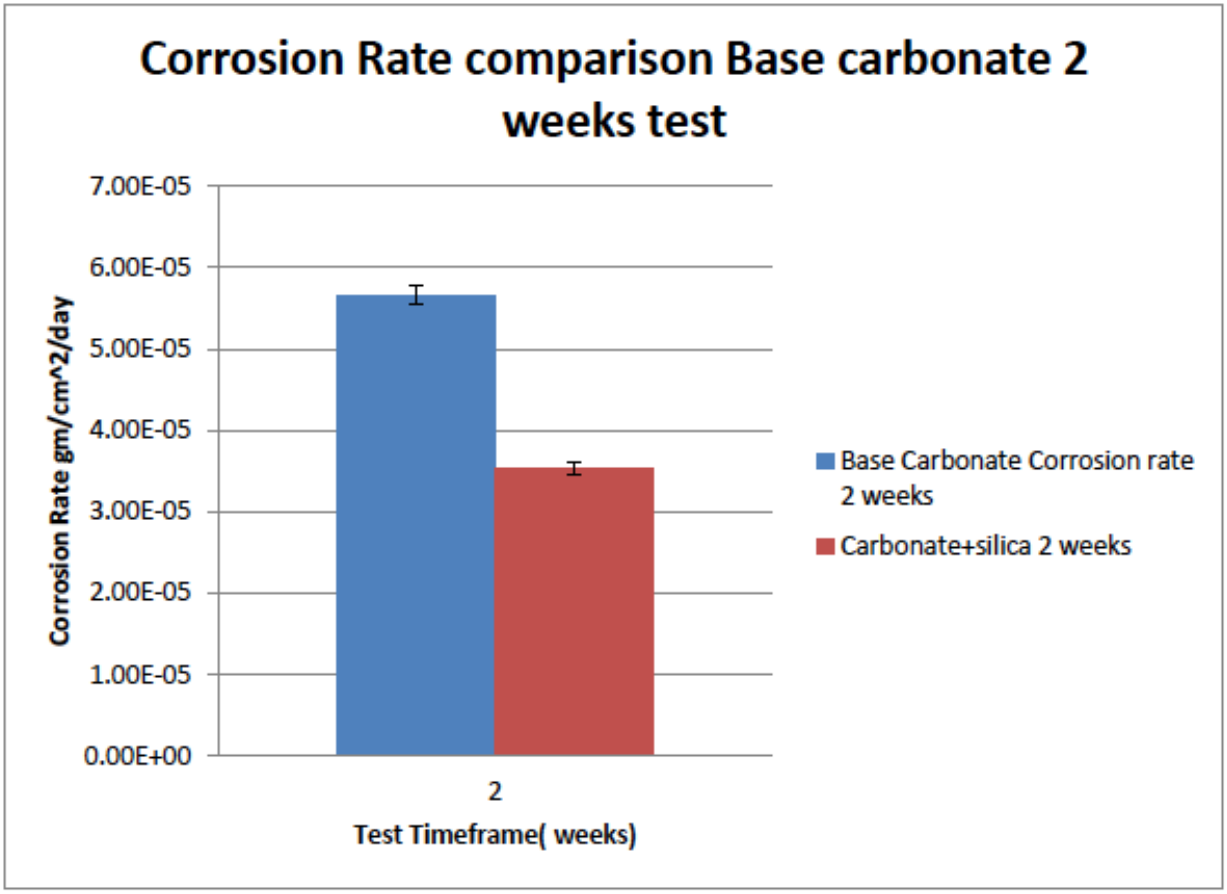

Figure 77: Instantaneous Corrosion Rate Comparison between Carbonate and Carbonate Doped with Silica at 2 Weeks.

Figure 78 indicates that due to doping, the corrosion rate has decreased by about 65% in comparison to the corrosion rate without doping. There is 95% confidence level in this result.

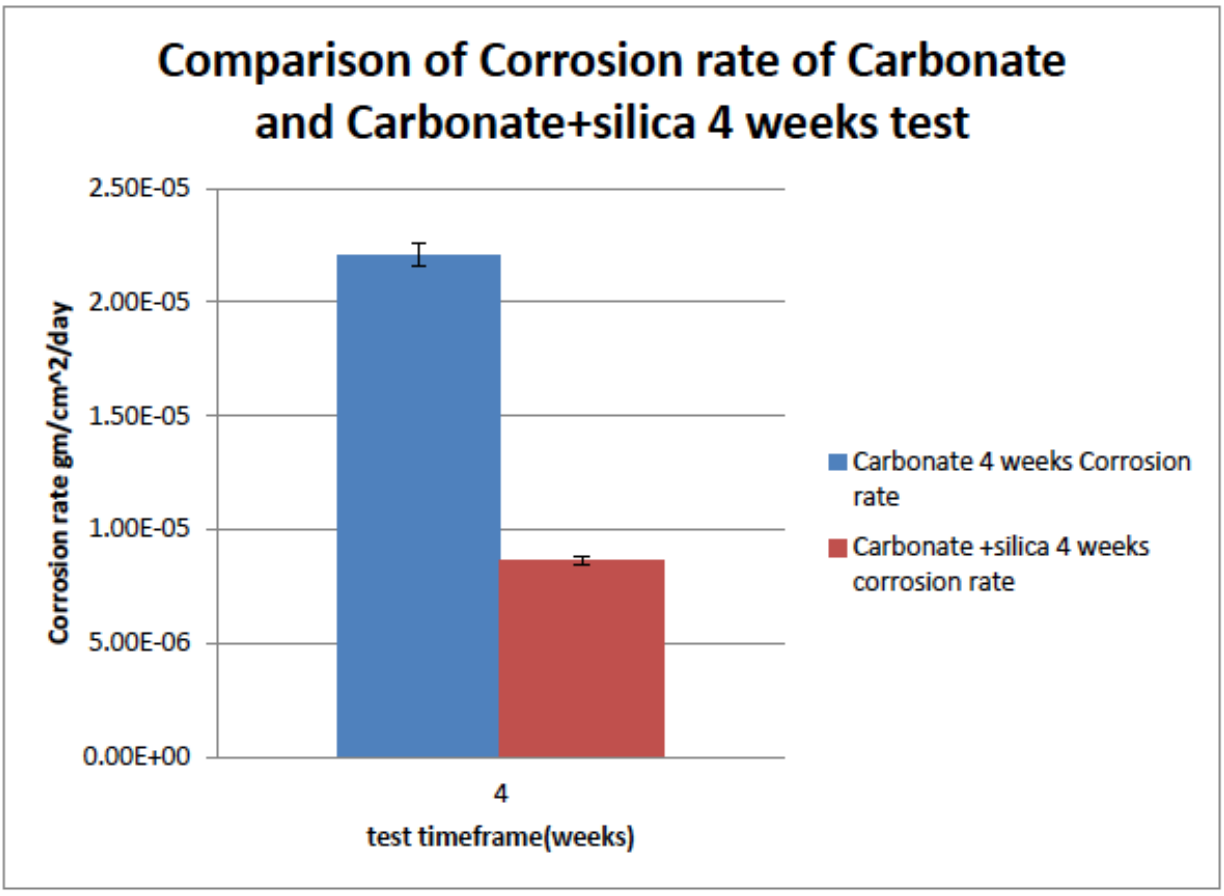

Figure 78: Instantaneous Corrosion Rate Comparison between Carbonate and Carbonate Doped with Silica (4 weeks).

Figure 79 indicates that due to doping the corrosion rate has decreased by about 50% in comparison to the corrosion rate without doping. There is 95% confidence level in this result.

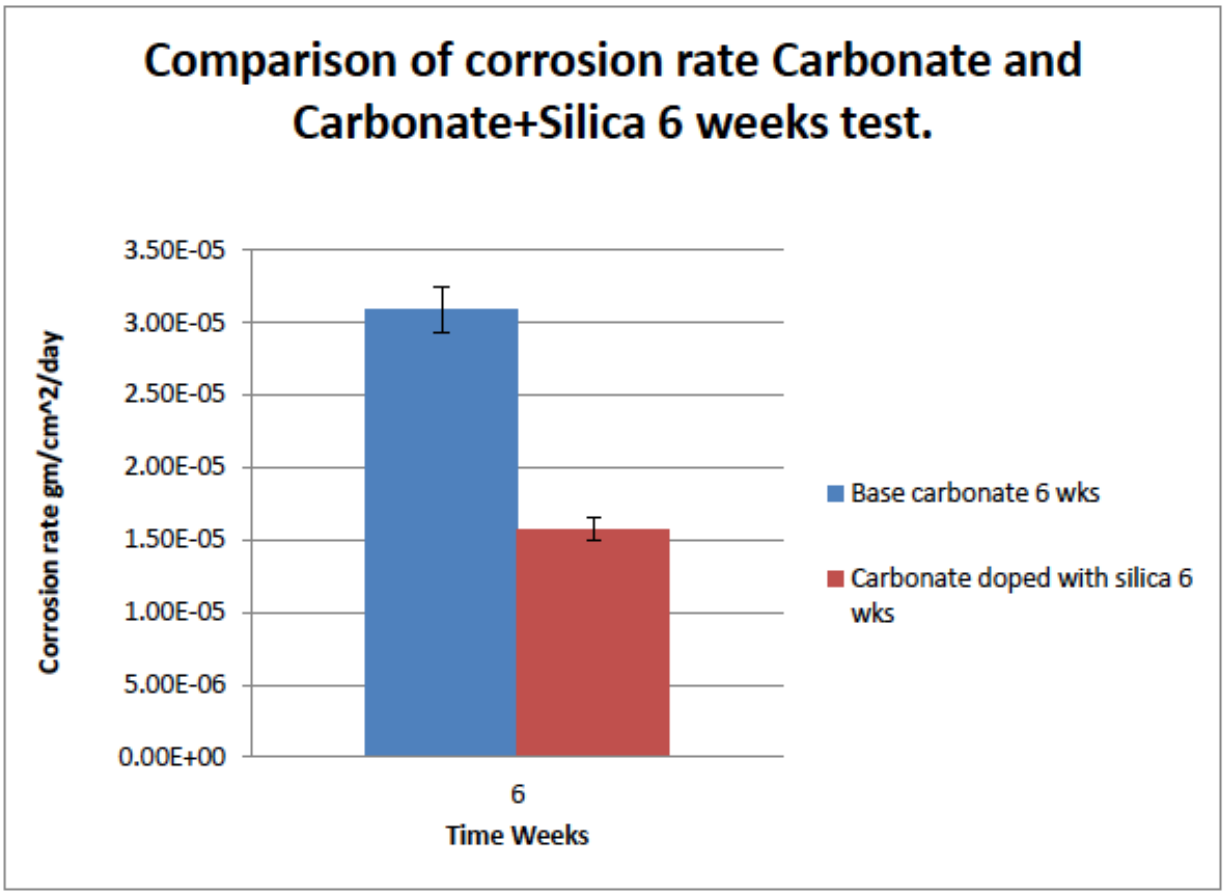

Figure 79: Instantaneous Corrosion rate Comparison between Carbonate and Carbonate Doped with Silica (6 weeks).

4.3.1.2 Comparison of Total Corrosion between Carbonate and Carbonate Doped with Silica

Figure 80 was constructed by plotting the average total mass loss per unit area against time. The bars indicate the mass loss per unit area at each time. Thus, the mass loss data of the steel coupons from the 2 week test normalized per unit area gives the total corrosion at 2 weeks. A similar statement holds for 4 and 6 weeks. This graph represents the corrosion characteristics of steel by molten plain and doped carbonate salts. This is compared with the theory where a parabolic behavior is expected. Both the carbonates and carbonates doped with silica deviated from the parabolic behavior but exhibited the same behavior.

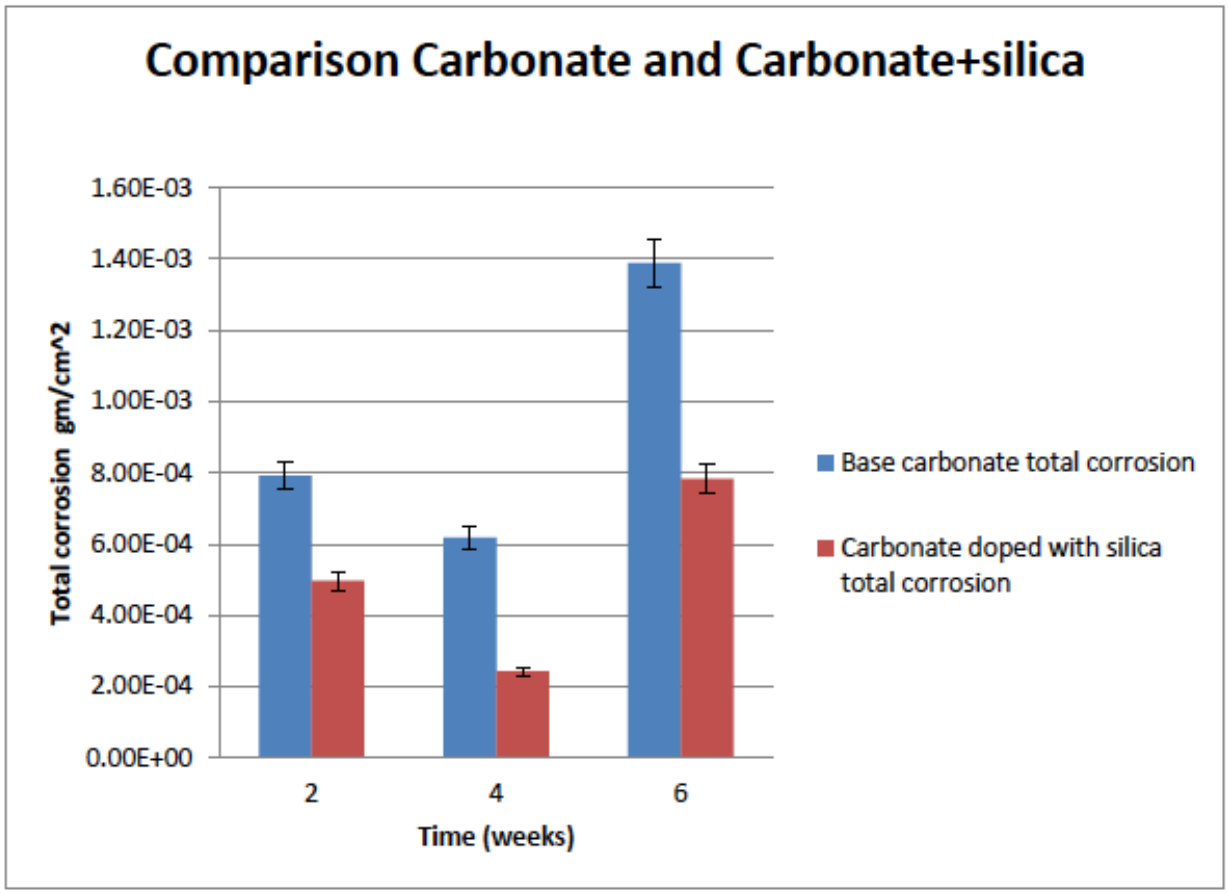

Figure 80: Total Mass Loss Comparison between Carbonate and Carbonate Doped with Silica.

4.3.1.3 Average Rate of Corrosion over all Exposure Times

The average rate of corrosion is determined to gauge the usability of the steel for CSP applications. Comparison of the average corrosion rate and the predefined metric from Table 4 permits qualitative recommendations on its applicability for CSP applications to be made. The term average indicates average of average of instantaneous corrosion rates over different exposure times. The Tables 43 and 44 below depicts the average corrosion rate by carbonate and carbonate doped with silica over all exposure times respectively.

Table 43: Average Corrosion Rate of Steel SS304 by Carbonate Eutectic at Different Timeframes.

Salt	Time (days)	Corrosion rate ($mg/cm^2/year$)
Carbonate	14	20.388
Carbonate	28	7.949
Carbonate	42	11.107

The average corrosion rate is 13.148

The corrosion rate due to carbonate doped with silica nanoparticles 1% by weight is depicted in Table 44.

Table 44: Average Corrosion Rate of Steel SS304 by Carbonate Doped with 1% Silica by Weight at Different Timeframes.

Salt	Time (days)	Corrosion rate (mg/cm2/year)
Carbonate + silica	14	12.751
Carbonate + silica	28	3.24
Carbonate + silica	42	5.646

The average corrosion rate is 7.212 mg/cm2/year.

4.3.1.4 The Relative Percentage Decrease in Corrosion Due to Doping of Silica with Respect to Base Carbonate

Figure 81 was created by dividing the difference in corrosion between the base carbonate and the corrosion due to doping and dividing it (difference) by the corrosion due to base carbonate expressed in percentage. This Figure serves as a visual aid to perceive the effect of silica nanoparticles on corrosion.

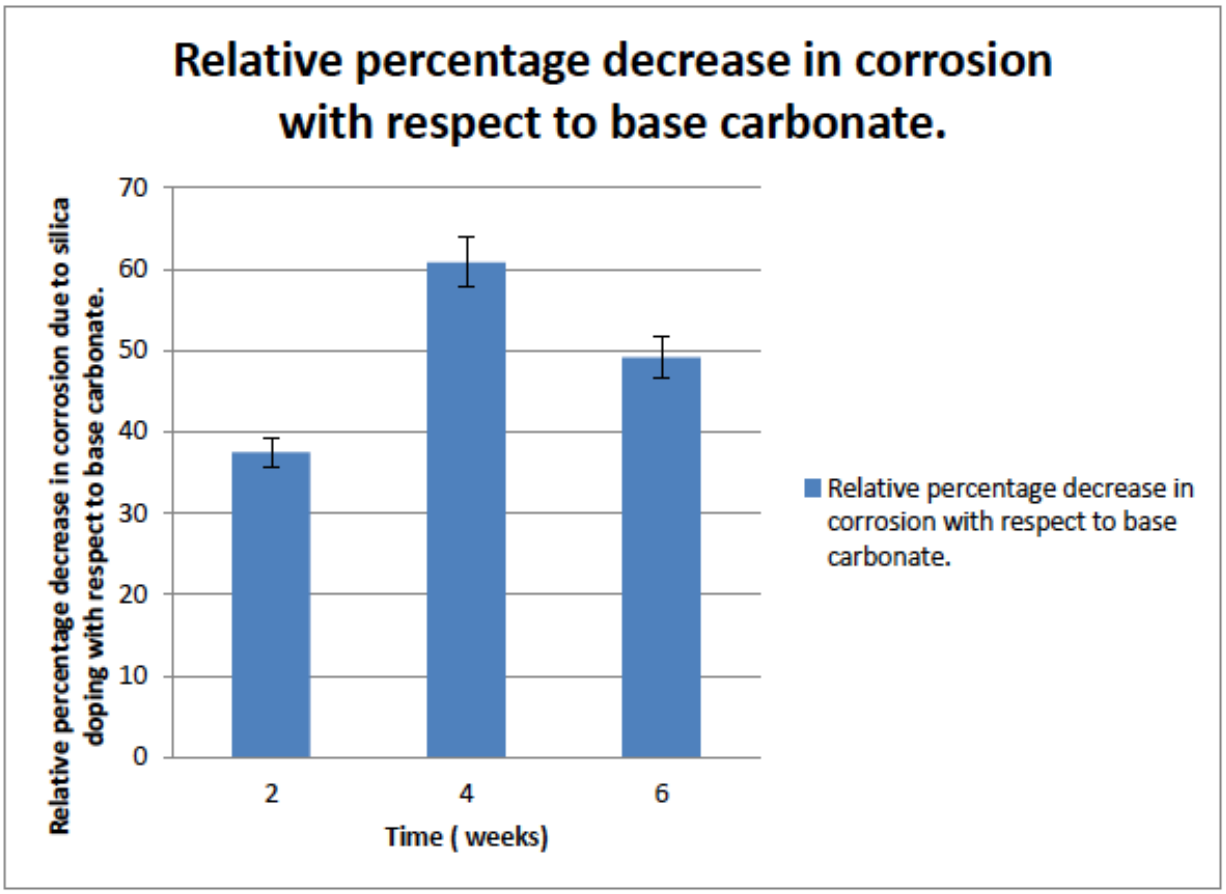

Figure 81: Relative Percentage Decrease in Corrosion Due to Doping of Silica.

4.3.1.5 Statistical Analysis

The results of this corrosion experiment showed an enhancement in the anticorrosive properties of molten carbonate by silica nanoparticles. These results must be statistically significant to make any claim valid in the discussions. This statistical analysis established the confidence level of the observations. A 2 tailed T test was performed to determine if the results are statistically significant. In this experiment the degrees of freedom were 4. This is arrived by determining the samples and subtracting 1 from each group. Since 2 groups are being compared, with each group having 3 data points, the degree of freedom evaluates to 4 (2X3-2). The confidence level was chosen to be 95 %. The critical t-value for this confidence level and degrees of freedom is 2.13. Table 44 shows the "t" test results.

Table 45: 'T' Test Results Table for the Rate of Corrosion of Carbonates and Carbonates Doped with Silica for the Three Times.

T Test 95% confidence level	**Difference in Mean**	**Variance**	**Sqrt(J)**	**t value (Mean/J)**	**Pass/ Fail**
carbonate +silica 2 weeks	0.000021	5.44E-10	7.37E-06	2.875	**Pass**
Carbonate + silica 4 weeks	0.000013	3.38E-11	5.82E-06	2.3071	**Pass**
Carbonate + silica 6 weeks	0.000015	2.73E-11	5.23E-06	2.8988	**Pass**

4.4 System Modeling

4.4.1 Sensitivity Modeling

The cost inputs used in the Excelergy model appeared to be outdated as the cost of the nitrate eutectic was assumed to be 0.5 $/kg whereas the price quoted by Coastal Chemical was 4.52 $/kg. The potential cost discrepancies were accounted for by normalizing the predicted TES system costs by dividing the cost of the investigated systems by the predicted cost of the Andasol I type TES system. The results of this parametric study are presented in Figure 82.

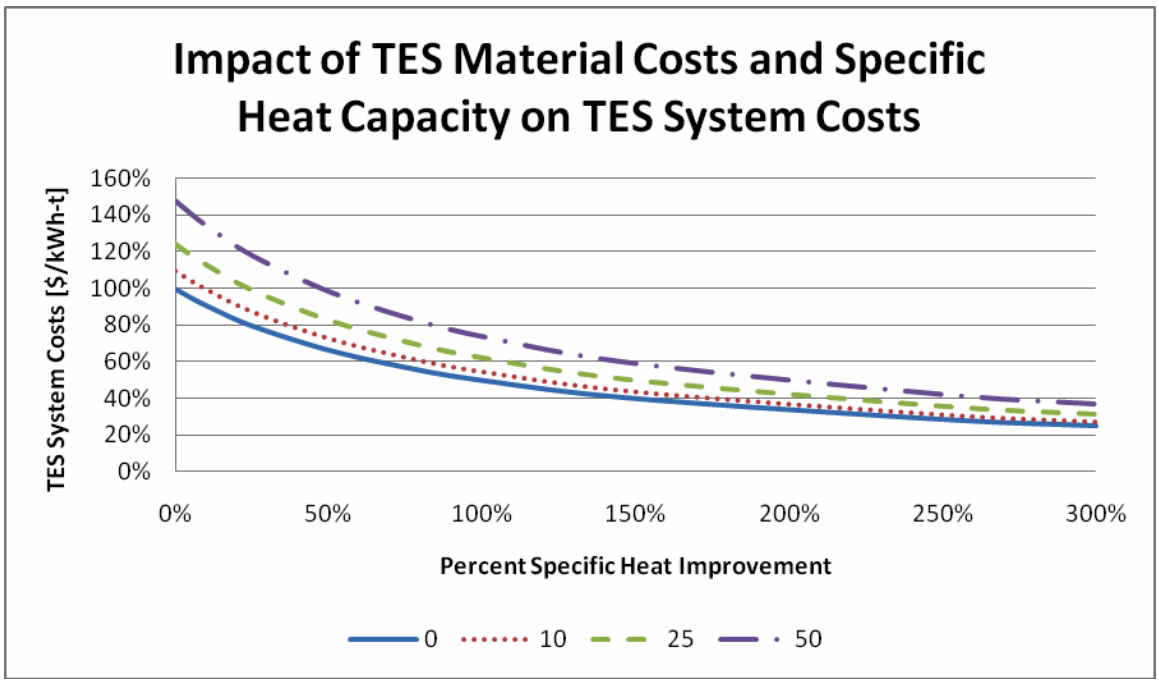

Figure 82: Normalized TES costs predicted by NREL Excelergy model.

The family of curves in Figure 82 represents TES system costs estimates for TES materials produced at 10, 25 and 50% cost increases. The 0% cost increase curve is provided for reference with the 0% specific heat improvement delineating the breakeven point for the other systems.

4.4.2 System Model

Due to the termination of the contract, no results were obtained from the system modeling beyond the validation detailed in section 3.5.

5 Findings

5.1 Nitrate Eutectic Salts

The addition of the alumina and silica nanoparticles to the nitrate using the given method caused an increase in the specific heat compared to the plain nitrate over the entire temperature range of interest.

The addition of the nanoparticles using the given method did not significantly alter the heat of fusion of the nitrate mixture.

The combination of the nitrate and silica using the given method in an aluminum container undergoes some change when raised to a temperature above 400C, causing the specific heat to drop over time.

The nitrate and alumina composite gave stable specific heat results up to 450C.

The ASTM and MDSC methods were determined to be functionally equivalent, based on the results generated by each method.

A large alumina nanoparticles mass fraction decrease in the nanofluid fabricated by using the hot plat method has been found.

The introduction of the alumina nanoparticles to the nitrate eutectic using the hot plate method resulted in a parabolic enhancement in the specific heat compared to the plain nitrate over the temperature range of interest.

The introduction of the alumina nanoparticles to the nitrate eutectic using the air dryer method significantly enhanced the specific heat compared to the plain nitrate over the temperature range of interest.

The addition of the alumina nanoparticles using each given methods had no influence on the heat of fusion and melting point.

The nanofluids fabricated by using the air dryer method showed higher specific heats, lower heat of fusion and similar melting point compared to the ones from the hot plate method.

The nanofluids from both given methods gave stable specific heat values up to 450^{o}C.

The addition of the alumina nanoparticles to the nitrate eutectic using the hot plate method decreased the thermal diffusivity and the thermal conductivity compared to the plain nitrate at temperature range of 65^{o}C to 145^{o}C.

During a long time span, the nano particles distribute evenly in the molten salt fluid even after many thermal cycles.

The composite of alumina nanoparticles and nitrate salt have good stability through thermal cycles.

The heat of fusion and melting point of the nitrate does not seem to be changed by the introduction of nanoparticles.

The addition of nanoparticles seems to decrease the thermal diffusivity and thermal conductivity of the nitrate eutectic.

5.2 Carbonate Eutectic Salts

The specific heat of the thermally cycled nanomaterial is stable with thermal cycling and does not show any trend with cycling time. The specific heat of the nanomaterial after thermal cycling is higher than the specific heat of the uncycled material.

The specific heat of the nanomaterial is independent of the concentration of the nanoparticles in

the material.

The specific heat of the nanomaterial is enhanced even at very low concentration of the nanoparticles in the nanomaterial.

Thermal cycling causes settling of nanoparticles due to gravity.

Thermal cycling causes the migration of the nanoparticles towards the walls of the sample container.

The rate of corrosion of steel by carbonate eutectics doped with silica nanoparticles was roughly half that of the rate of corrosion by the base carbonate for all time periods tested.

5.3 Modeling

The outputs of the model were very close to those produced by SAMS. The differences can be attributed to small changes in the ways in which certain output parameters were scored.

5.4 General

The evaporation and air dryer manufacturing methods produce identical materials.

The specific heat modification remained stable for both multiple phase changes and several hours in the liquid state.

The specific heat remained stable for a shelf life of at least two months.

Thermal cycling changes the distribution of the nanoparticles in the composite material, however, this change does not appear to affect the specific heat of the material for our test conditions.

6 Conclusions

The addition of ceramic nanoparticles enhances the specific heat of the nitrate and carbonate eutectics, even at low mass percentages. This enhancement is stable with time and thermal cycling.

The air dryer method is suitable for mass production of composite nanoparticles.

Nanoparticle augmentation of the thermophysical properties of both the nitrate and carbonate salts for use in a TES system works.

The composite can be implemented into existing system designs to improve the performance of such systems without additional equipment or sub-systems.

Using the nitrate or carbonate composites can benefit existing and future TES systems,

implemented in a CSP plant or other power generation facility.

References

[1] G. Ondrey, Solar's second coming, Chemical Engineering 116 (2009) 18-21.

[2] energy leveling [2] Andasol 1 goes into operation, RenewableEnergyWorld.com (2008) http://www.renewableenergyworld.com/rea/news/article/2008/11/andasol-1-goes-intooperation-54019.

[3] NREL 2000 study [6] National Renewable Energy Laboratory, Survey of Thermal Storage for Parabolic
Trough Power Plants, NREL/SR-550-27925, National Renewable Energy Laboratory (2000).

[4] thermocline material [7] D. Brosseau, J.W. Kelton, D. Ray, M. Edgar, K. Chisman, B. Emms, Testing of thermocline filler materials and molten-salt heat transfer fluids for thermal energy

[5] Divya- battery storage [8] K.C. Divya, J. Ostergaard, Battery energy storage technology for power systems – An overview, Electric Power Systems Research 79 (2009) 511-520.

[6] nano fluid [10] D. Wen, G. Lin, S. Vafaei, K. Zhang, Review of nanofluids for heat transfer applications, Particuology 7 (2009) 141-150.

[7] Zhou and Ni [11] S.Q. Zhou, R. Ni, Measurement of the specific heat of water-based AL2O3 nanofluid, Applied Physics Letters 92 (2008).

[8] Nelson [12] I.C. Nelson, D. Banerjee, Flow loop experiments using nanofluids, Poster Presentation, Texas A&M University.

[9] Andasol 1 performance [4] U. Hermann, D. Kearney, Survey of thermal energy storage for parabolic trough Power Plants, ASME J. of Solar Energy Engineering 124 (2002) 145-152.

[10] Choi S.U.S, Eastman J.A., 1995, "Enhancing Thermal Conductivity of Fluids with Nanoparticles." ASME International Mechanical Engineering Congress & Exposition, November 12-17, San Francisco, CA.

[11] J.A. Eastman, U.S. Choi, S.Li, L.J. Thompson, S. Lee, "Enhanced Thermal Conductivity through the Development of Nanofluids." Materials Research Society Symposium- Proceedings, 457, pp. 3-11.

[12] Lee S., Choi S.U.S., Li S., Eastman J.A., 1999, "Measuring Thermal Conductivity of Fluids Containing Oxide Nanoparticles." ASME J. Heat Transfer, 121(2), pp. 280-289.

[13] D.V. Kuznetsov, S.P. Bardakhanov, A.V. Nomoev, S.A. Novopashin, V.Z. Lygdenov, 2010, "Heat Conductivity of Nanofluids Based on Al2O3, SiO2 and TiO2." J Engineering Thermophysics, 19, pp. 138-143.

[14] Wang X, Xu X, Choi S.U.S, 1999, "Thermal Conductivity of Nanoparticle-Fluid mixture." J Thermal Physics Heat Transfer, 13, pp. 474-480.

[15] Wikipedia, available From: http://en.wikipedia.org/wiki/Settling

[16] Mohammed M. Farid, Amar M. Khudhair, A review on phase change energy storage: materials and applications, Energy Conversion and management 45 (2004) 1597-1615

[17] Suegama, P.H. 2008 "Corrosion behavior of carbon steel protected with single and bi-layer of silane films filled with silica nanoparticles," Surface & Coatings Technology **202,** pp.2850-2858.

[18] S.D Cramer and B.S Covino,Jr(Eds.), "Corrosion:Fundamentals, Testing and Protection ASM International"**.** Vol. 13 A**.**

[19] Goods, S.H. and Bradshaw, R.W, 2004, "Corrosion of stainless steels and carbon steel by molten mixtures of commercial nitrate salts, "Journal of Materials Engineering and Performance, **13**(1), pp. 78-87.

[20] Sadahiro T, Shinya N, Tadao W, 2006, "Correlation of grain boundary connectivity with grain boundary character distribution in austenitic stainless steel," Acta Materialia **54** 3617–3626, pp. 54.

[21] "Molten Salt Solar Energy Thermal Storage and Concentrated Solar Power (CSP) Market Shares, Strategies, and Forecasts, Worldwide, 2010 to 2016, " Market Research News, May 9 2011.

[22] Tomashov, N D**.** 1967, *Theory of Corrosion and Protection of Metals: The Science of Corrosion*. The Macmillan Company, New York. 57

[23] Scott, L.R., Pile L. D. , Butt, P. D, 1998." Materials Corrosion and Mitigation Strategies for APT". Materials Corrosion & Environmental Effects Lab: Los Alamos National Laboratory, Los Alamos, NM..

[24] Cabeza, L.F., Badia, F., Illa J., Roca, J.**,** Illa, J., Mehling, H., Heibler, S., Zeigler, F., 2001, "Immersion corrosion tests on metal-salt hydrate pairs used for latent heat storage in the 32 to 36° C temperature range," Material and Corrosion, **52**(2)**,** pp.140-146**.**

[25] Coastal Chemical data 1.) Coastal Chemical L.L.C. Hitec solar salt coastal chemical specification sheet. Coastal Chemical L.L.C., Houston TX. 2010.

[26] Janz GJ, Allen CB, Bansal NP, Murphy RM, Tomkins RPT. Physical properties data

compilations relevant to energy storage: molten salts: data on single and multicomponent salt systems. Rensselaer Polytechnic Institute, Troy, New York, April 1979;
396-411.

[27] Janz GJ, Allen CB, Murphy RM, Tomkins RPT. Physical properties data compilations relevant to energy storage I: molten salts eutectic data. *NSRDS-NBS-61;* US Government Printing Office, Washington DC, 1978.

[28] Peng Q, Wei X, Ding J, Yang J, Yang X. High-temperature thermal stability of molten salt materials. *International Journal of Energy Research*, 2008; **32**: 1164-1174.

[29] Petri, R.J., 1979, "Evaluation of Molten Carbonates as Latent Heat Thermal Energy Storage materials," Proceedings of the 14th Intersociety Energy Conversion Engineering Conference, Boston, MA, Aug. 5-10, 1979.

[30] Janz, G.J., Allen, C.B., Bansal, N.P., Murphy, R.M., Tomkins, R.P.T., 1979 "Physical Properties Data Compilation Relevant to Energy Storage, Molten Salt: Data on Single and Multi Component Salt Systems," National Standard Reference Data System, National Bureau of Standards, 61, Part I.

[31] Eastman JA, Choi SUS, Li S, Thompson LJ Lee S. Enhanced thermal conductivity through the development of nanofluids. *Presented at the Materials Research Society 1996 Fall Meeting*, Boston MA, Dec. 2-6 1996.
[23] Eastman JA, Choi SUS, Li S, Thompson LJ, Yu W. Anomalously increased effective thermal conductivities of ethylene glycol-based nanofluids containing copper nanoparticles. *Applied Physics Letters*, 2001; **78**(6): 718-720.

[33] Wang X, Mujumdar A. Heat transfer characteristics of nanofluids: a review. *International Journal of Thermal Sciences,* 2007; **46:** 1-19.

[34] Wang B, Zhou L, Peng X. Surface and size effects on the specific heat capacity of nanoparticles. *International Journal of Thermophysics* 2006; **27**(1): 139-151.

[35] Zhou L, Wang B, Peng X, Du X, Yang Y. On the specific heat capacity of CuO nanofluid. *Advancements in Mechanical Engineering* 2009; Hindawi Publishing Corporation.

[36] Sundar L, Sharma KV, Ramanathan S. Experimental investigation of heat transfer enhancements with Al2O3 nanofluid and twisted tape insert in a circular tube. *International Journal of Nanotechnology and Applications*, 2007; **1** (2): 21-28.

[37] Likhachev VN, Astakhova T, Vinogradov GA, Alymov MI. Anomalous heat capacity of nanoparticles. *Russian Journal of Physical Chemistry B,* 2007; **1**(1): 89-93.

[38] W.J. Parker, R.J. Jenkins, C.P. Butler, 1961, "Flash Method of Determining Thermal Diffusivity, Heat Capacity and Thermal Conductivity." J Appl. Phys, 32(9), pp. 1679-1684.

[39] Tzvetkoff, T.Z., Girginov, A, Bojinov, M**.** 1995 "Review Corrosion of nickel, iron, cobalt and their alloys in molten salt electrolytes". , Journal of Material Science, **30**, pp. 5561-5575.

[40] Heat Loss Testing of Schott's 2008 PTR70 Parabolic Trough Receiver, www.nrel.gov/csp/troughnet/pdfs/45633.pdf

[41] http://apps1.eere.energy.gov/buildings/energyplus/cfm/weather_data3.cfm/region=6_europe_wmo_region_6/country=ESP/cname=Spain

[42] http://www.netzsch-thermal-analysis.com/download/LFA_447_Nanoflash_E_1108_en_180.pdf